Democratic and Popular Republic of Algeria
Ministry of Higher Education and Scientific
Research University Mohamed Khider of
Biskra

Faculty of Exact Sciences and Science of Nature
and LifeDepartment of
Sciences of Matter

Ref : ……..

Thesis Presented to obtain the degree of

Doctorate in Chemistry

Option: Inorganic Chemistry

Entitled:

Synthesis and characterization of mixed oxides applicable as catalysts and photocatalysts using solar energy

Presented by:
Djamel Eddine Mazouzi

Publicly defended on: 30/ 04/ 2025

In front of the Jury committee composed of:

Ms. Fatima Zohra Sriti	MCA	University of Biskra	President
Mr. Faiçal Djani	Professor	University of Biskra	Supervisor
Mr. Rachid Makhloufi	MCA	University of Biskra	Examiner
Mr. Abdelhakim Chadli	MCA	University of Biskra	Examiner
Mr. Abdelhakim Khainach	MCA	University of Msila	Examiner
Mr. Ahmed Bahloul	Professor	University of .Msila	Examiner

Acknowledgment

All praise is due to Allah, the Lord or the worlds, for his countless blessings and guidance throughout this research.

Words cannot express my gratitude to my supervisor Pr. Dr. Faiçal Djani for his invaluable patience, guidance, motivation and precious advices along the way of my Ph.D. research.

I would like to express my deepest appreciation to the defense committee.

I am extremely grateful to pedagogic laboratory staff of the matter sciences department for their hosting and tolerance.

Words cannot express my gratitude to Pr. Dr. Fatih Şen head of the nanotechnology laboratory at Kütahya Dumlupinar University for his hosting in his laboratory in order to perform a part of this thesis. I am also thankful to Pr. Dr. Arturo Martinez Arias for his meaningful help. Without forgetting my sincere thanks to Pr. Dr. Abdelouhed Chala for granting the perform of available analysis in his lab LPCMA.

Special thanks should also go to Mehdi Kaci Abdelraouf Soukeur for their help and efforts for performing characterizations.

Lastly, I would like to mention Dr. Salah Eddine Hachani and Dr. Soufiane Makhloufi for their encouragements and precious advices.

Dedication

I dedicate this work to:

My parents

My grandma (may Allah be merciful to her)

My brother

My sisters and my wife

Djamel Eddine

Table of content

List of figures

List of tables

List of abreviations

GENERAL INTRODUCTION

CHAPTER I : BIBLIOGRAPHIC STUDY

CHAPTER II : SYNTHESIS, CHARACTERIZATION TECHNIQUES AND PHOTOCATALYTIC & CATALYTIC PROCESSES DESCRIPTION

CHAPITRE III : AUTOCOMBUSTION SYNTHESIS OF $BiFeO_3/Bi_2O_3$, AND ITS PROPERTIES

CHAPTER IV : PHOTOCATALYTIC AND CATALYTIC PERFORMANCE OF $BiFeO_3/Bi_2O_3$ SYSTEM

List of figures

List of tables

List of abbreviations

XRD: X-ray diffraction.

SEM: Scanning electron microscopy.

EDS: Energy dispersive spectroscopy.

NB: Nitrobenzene.

FTIR: Fourier transform infra-red spectroscopy.

XPS: X-ray photoelectron spectroscopy.

BB5: $BiFeO_3/Bi_2O_3$ composite material synthesized through 5% excess of Bi nitrates.

NB: Nitrobenzene.

GENERAL INTRODUCTION

GENERAL INTRODUCTION

The interaction of light with molecules and the resulting processes are currently of major interest in the development of various chemical technologies. Various types of semiconductor catalysts are known to be photosensitive, allowing activation by light photons. Photoactivated molecules may initiate or influence the rate of chemical reaction by energy or charge carrier transfer. Materials or molecules active for the process are known as photocatalysts and main aspects of research in this field are dedicated to discover most active configurations of them for useful processes.

Energy shortage and environmental pollution have become two urgent problems that restrict social development and endanger human survival. In order to resolve the two issues and to realize the sustainable development of society, the most effective route is the active development and utilization of clean and renewable energy sources, among which solar energy is the most promising candidate due to its availability and wide distribution. However, the large scale utilization of solar energy is still restricted at present due to its low energy density, high geographical dispersion, high time instability, and inconvenience for storage. H_2 is a kind of superior energy carrier and ideal clean and renewable energy due to its high energy density, absence of pollution from combustion products, convenience for storage and transportation. Consequently, exploring and performing the conversion and storage of solar energy as hydrogen energy is a powerful route to develop and utilize renewable energy.

Photocatalytic products were first marketed in Japan in the mid-1990s, and later in America and Europe. By 2009, the global volume of solar photocatalysis-based products was $848 million and is expected to double in 2014, reaching nearly $1.7 billion (Fig. 1). In 2009, photocatalytic products for construction accounted for the largest share of the market (over 87%), with estimated gains of $740.3 million. At a predicted compound annual growth rate (CAGR) of 14.5%, these will reach $1.5 billion in 2014. The consumer products market segment was worth $85 million for the same year, and is expected to grow at a CAGR of 13.2% to $158 million in 2014.

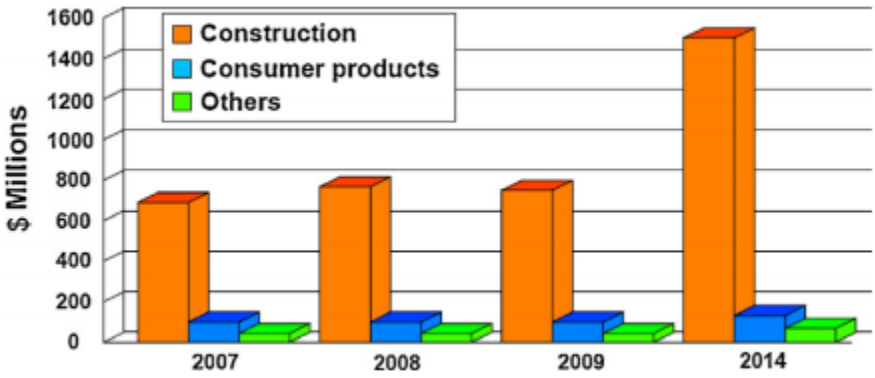

Figure 1: Global market for photocatalysts production[1].

The developed photocatalytic materials for H_2 and O_2 evolution mainly contain inorganic semiconductors, metal organic complexes, organic semiconductors, and recently reported conductors, in which inorganic semiconductor photocatalysts showed great promising for future applications. Considering the fundamental principle, the photocatalyst should exhibit bandgap larger than the standard Gibbs free energy change (1.23 eV) for water splitting into H_2 and O_2, and should have conduction band with potential more negative than that for water reduction and valence band with potential more positive than that for water oxidation. Furthermore, based on the processes, firstly, photocatalyst should have bandgap smaller than

the energies of incident photons to ensure the excitation of photogenerated charge carriers. Visible light accounts for around 43% of the incoming solar energy, and therefore should be fully used by photocatalysts with excellent visible-light response [2]. Secondly, photocatalyst should have good ability to promote the separation and transfer of photogenerated charge carriers and thus to restrain their recombination. Thirdly, photocatalyst should provide enough reactive sites to accelerate redox reaction and to restrain the back-reaction. In a word, in order to improve the photocatalytic reaction, photocatalyst should enhance the generation, transfer, and reaction of photogenerated charge carriers during the whole photocatalytic process. Furthermore, based on the processes involved, a photocatalyst should:

- Have a bandgap smaller than the energies of incident photons to ensure the excitation of photogenerated charge carriers. Since visible light accounts for around 43% of incoming solar energy, photocatalysts with excellent visible-light response are crucial for efficient solar energy utilization [2], [3].
- Possess a good ability to promote the separation and transfer of photogenerated charge carriers and thus to restrain their recombination [4], [5].
- Provide enough reactive sites to accelerate the redox reaction and to restrain back-reaction [6], [7].

In summary, to improve photocatalytic reaction efficiency, a photocatalyst should enhance the generation, transfer, and reaction of photogenerated charge carriers throughout the entire photocatalytic process.

Recent research has significantly advanced the discovery of novel photocatalytic materials with enhanced efficiency and visible-light activity. Among these, perovskite materials have garnered considerable attention due to their unique crystal structures, tunable electronic properties, and excellent light-harvesting capabilities. Perovskites, generally represented by the formula ABX_3, offer a flexible framework that allows for compositional engineering to optimize band alignment, charge separation, and catalytic activity [8], [9]. Their remarkable performance in solar cell applications has naturally extended interest to their use in photocatalysis, particularly for water splitting and CO_2 reduction [10], [11].

A promising example within the complex oxide family is bismuth ferrite ($BiFeO_3$), a multiferroic material known for its coexistence of ferroelectric and antiferromagnetic orders at room temperature. More recently, $BiFeO_3$ has been explored for its impressive photocatalytic power, especially under visible light irradiation [12]. Its narrow bandgap (around 2.2 eV) makes it a suitable candidate for absorbing a significant portion of the solar spectrum. The unique internal electric fields originating from its ferroelectric nature can effectively promote the separation of photogenerated electron-hole pairs, thereby reducing recombination and enhancing photocatalytic efficiency [13]. Furthermore, the strategic incorporation of bismuth oxide (Bi_2O_3) to form a $BiFeO_3/Bi_2O_3$ mixed oxide system offers an exciting avenue to further boost photocatalytic performance. This heterojunction approach can create beneficial interfaces that facilitate charge transfer and improve light absorption, making the $BiFeO_3/Bi_2O_3$ system a compelling subject for advanced photocatalytic research [14], [15].

This thesis aims to contribute to the advancement of photocatalytic/catalytic materials for sustainable environmental and energy solutions, leveraging the abundant solar energy available in our region of Biskra. The research focuses on the development and characterization of novel mixed oxide systems. The work is organized into four chapters:

- **Chapter I: Bibliographic Study** provides a comprehensive review of the current state-of-the-art in photocatalysis and catalysis covering fundamental principles, various photocatalytic materials, and their applications.
- **Chapter II: Synthesis, Characterization Techniques, and Photocatalytic & Catalytic Processes Description** details the experimental methodologies employed in this research, including synthesis routes, material characterization techniques, and the procedures for evaluating photocatalytic and catalytic performance.
- **Chapter III: Autocombustion Synthesis of $BiFeO_3/Bi_2O_3$ and Its Properties** focuses on the synthesis of the $BiFeO_3/Bi_2O_3$ mixed oxide system using the autocombustion method and investigates its structural, morphological, optical, and electronic properties.
- **Chapter IV: and the last one: Photocatalytic and Catalytic Performance of $BiFeO_3/Bi_2O_3$ System** presents the experimental results on the photocatalytic and catalytic activities of the synthesized $BiFeO_3/Bi_2O_3$ system, discussing its efficiency in relevant chemical reactions and proposing mechanisms for its enhanced performance.

References:

[1] D. Spasiano, R. Marotta, S. Malato, P. Fernandez-Ibañez, and I. Di Somma, "Solar photocatalysis: Materials, reactors, some commercial, and pre-industrialized applications. A comprehensive approach," Jul. 01, 2015, *Elsevier*. doi: 10.1016/j.apcatb.2014.12.050.

[2] X. Sun, S. Jiang, H. Huang, H. Li, B. Jia, and T. Ma, "Solar Energy Catalysis," Jul. 18, 2022, *John Wiley and Sons Inc*. doi: 10.1002/anie.202204880.

[3] D. P. Bui, M. T. Pham, H. H. Tran, T. D. Nguyen, T. M. Cao, and V. Van Pham, "Revisiting the Key Optical and Electrical Characteristics in Reporting the Photocatalysis of Semiconductors," *ACS Omega*, vol. 6, no. 41, pp. 27379–27386, Oct. 2021, doi: 10.1021/acsomega.1c04215.

[4] R. Yanagi, T. Zhao, D. Solanki, Z. Pan, and S. Hu, "Charge Separation in Photocatalysts: Mechanisms, Physical Parameters, and Design Principles," *ACS Energy Lett*, vol. 7, no. 1, pp. 432–452, Jan. 2022, doi: 10.1021/acsenergylett.1c02516.

[5] J. Xue, M. Fujitsuka, T. Tachikawa, J. Bao, and T. Majima, "Charge Trapping in Semiconductor Photocatalysts: A Time- and Space-Domain Perspective," *J Am Chem Soc*, vol. 146, no. 13, pp. 8787–8799, Apr. 2024, doi: 10.1021/jacs.3c14757.

[6] J. Wang, M. Zhu, A. Sun, R. Yuan, H. Chen, and B. Zhou, "The Influence Mechanism of Dissolved Organic Matter on the Photocatalytic Oxidation of Pharmaceuticals and Personal Care Products," *Molecules*, vol. 30, no. 11, p. 2266, May 2025, doi: 10.3390/molecules30112266.

[7] S. He, Y. Chen, J. Fang, Y. Liu, and Z. Lin, "Optimizing photocatalysis via electron spin control," 2025, *Royal Society of Chemistry*. doi: 10.1039/d4cs00317a.

[8] E. Grabowska, "Selected perovskite oxides: Characterization, preparation and photocatalytic properties-A review," Jun. 05, 2016, *Elsevier B.V.* doi: 10.1016/j.apcatb.2015.12.035.

[9] A. Baray-Calderón *et al.*, "Recent Advances in Perovskite-Based Heterojunction Photocatalysts: Synthesis, Properties, and Applications," Apr. 01, 2025, *Springer*. doi: 10.1007/s11814-025-00416-1.

[10] K. Bienkowski *et al.*, "Halide Perovskites for Photoelectrochemical Water Splitting and CO_2 Reduction: Challenges and Opportunities," May 03, 2024, *American Chemical Society*. doi: 10.1021/acscatal.3c06040.

[11] M. A. Raza, F. Li, M. Que, L. Zhu, and X. Chen, "Photocatalytic reduction of $CO_2$by halide perovskites: Recent advances and future perspectives," Nov. 21, 2021, *Royal Society of Chemistry*. doi: 10.1039/d1ma00703c.

[12] H. Li *et al.*, "Recent advances in the application of bismuth-based catalysts for degrading environmental emerging organic contaminants through photocatalysis: A review," Oct. 01, 2023, *Elsevier Ltd*. doi: 10.1016/j.jece.2023.110371.

[13] S. Mittal, S. Garg, H. Bhandari, and V. Sharma, “A review on recent progressions of Bismuth ferrite modified morphologies as an effective photocatalyst to curb water and air pollution,” Oct. 01, 2022, *Elsevier B.V.* doi: 10.1016/j.inoche.2022.109834.

[14] Y. Nassereddine, M. Benyoussef, B. Asbani, M. El Marssi, and M. Jouiad, “Recent Advances toward Enhanced Photocatalytic Proprieties of $BiFeO_3$-Based Materials,” Jan. 01, 2024, *Multidisciplinary Digital Publishing Institute (MDPI)*. doi: 10.3390/nano14010051.

[15] C. Zhu, Z. Chen, C. Zhong, and Z. Lu, “Facile synthesis of $BiFeO_3$ nanosheets with enhanced visible-light photocatalytic activity,” *Journal of Materials Science: Materials in Electronics*, vol. 29, no. 6, pp. 4817–4829, Mar. 2018, doi: 10.1007/s10854-017-8437-6.

.

CHAPTER I :

BIBLIOGRAPHIC STUDY

Chapter I :

Bibliographic study

I.1.Materials:

I.1.1.Mixed Oxides:

The mixed oxide (MM'O) constitutes of two or more different metal cations combined with oxygen. MM'Os find extensive applications as additives or colorants in the pulp and paper, coating, or polymer sectors, while their usage in ceramic and electronic fields is pervasive. MM'Os represent the most thermally stable, chemically unreactive, luminous, and enduring pigments to date. Typically formed at elevated temperatures, they comprise solely of metal cations and oxygen anions. While the metallic constituents of MOs may pertain to any group on the periodic table, they can be classified into five primary groupings based on their molecular composition: aluminates, titanates, silicates, ferrites, and chromites. Furthermore, they can be categorized according to their crystal structures; in this analysis, the focus has been on aluminates and titanates and their respective crystal formations, spinel and perovskite.[1] MM'O nanoparticles, also known as heterometal oxide nanoparticles, have the potential significantly impact various domains within the fields of chemistry and physics. The distinct electronic and magnetic characteristics achieved through the fusion of two metals within an oxide framework have been extensively researched.[2], [3] However, the predominant application of Mixed Oxides (MM'Os) lies within the realm of catalysis, where they are utilized both as the primary catalyst and as supports for catalysts.[4], [5] MM'O incorporating aluminum has been identified as presenting numerous prospects in the field of catalysis.[6], [7].

I.1.1.1.$BiFeO_3$:

$BiFeO_3$, known as the exemplar of monophasic multiferroic substances, exhibits promising potential in the realms of data storage, sensors, and actuators. This particular perovskite showcases a crystallographic structure of rhombohedral R3c and manifests a cycloidal magnetic arrangement with spin modulation, featuring a modulation period of approximately 62 nm. Notably, it presents magnetoelectric interplay at standard room temperature. Nevertheless, its subpar remanent magnetization and relatively significant leakage current stand out as primary obstacles hindering its prospective utilizations. $BiFeO_3$ is the focus of considerable attention owing to its potential applications in spintronics, data storage microelectronics, and other fields, as well as the intriguing physics underlying its properties. The ferroelectric ordering of $BiFeO_3$, with a Curie temperature of approximately 830°C, is a result of the sterochemical effects stemming from the lone electron pair of Bi^{3+}.[8] Below (Néel

temperature) TN = 370◦C, the magnetic configuration exhibited by $BiFeO_3$ is characterized by G-type antiferromagnetism. It features a modulated cycloidal spin structure with a substantial periodicity of 62 nm. Ferroelectricity, characterized by a significant remanent polarization of approximately 136 μC cm^{-2}, has been detected in thin films of $BiFeO_3$ that were fabricated using pulsed laser deposition.[9] and as large as 2Pr ∼ 197.1 μC cm^{-2} in films grown by off-axis radio-frequency magnetron sputtering.[10] In the case of $BiFeO_3$ bulk ceramics, the attainment of a single-phase perovskite structure presents a considerable challenge in synthesis. The process of phase formation often results in the presence of impurity phases, including $Bi_2Fe_4O_9$, Bi_2O_3, and $Bi_{25}FeO_{39}$.[11], [12] Nitric acid extraction is utilized for the purpose of removing impurity components subsequent to the process of calcination involving a combination of bismuth and iron oxides. Within large-scale samples, challenges related to seepage hinder the ability to accurately observe the inherent saturated ferroelectric hysteresis loops. The seepage found in ceramics composed of $BiFeO_3$ is believed to be triggered by the presence of Fe^{2+} and vacancies in oxygen, both of which also have adverse effects on the intrinsic magnetic characteristics.[13]

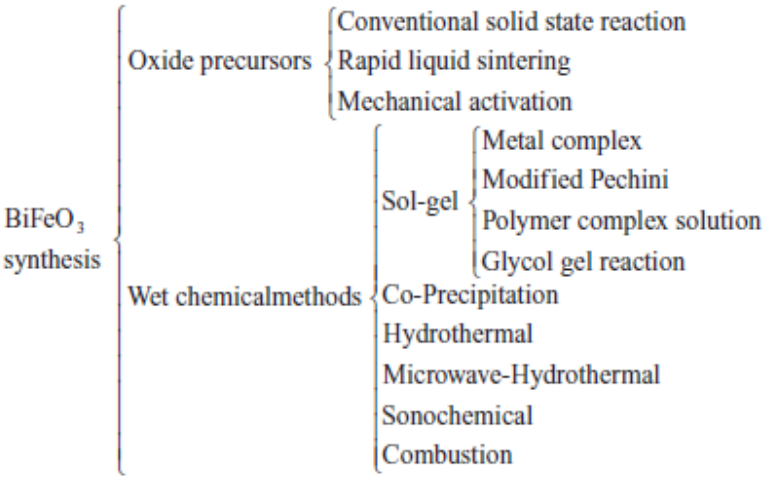

Figure I.1: A schematic illustrating the methodologies employed in the synthesis of $BiFeO_3$.[14]

I.1.2. Simple oxides:

I.1.2.1. Bi_2O_3:

Research on bismuth commenced during the 19th century; however, it gained significant momentum in 2004, primarily attributed to its advantageous characteristics and minimal toxicity. Moreover, the initial study on bismuth oxide, which was published in a journal, dates back to the year 1989.[15] Bismuth oxide (Bi_2O_3) is distinguished by its effective photocatalytic and antibacterial characteristics. Possessing a moderate band gap, Bi_2O_3 can efficiently capture visible light to initiate photocatalytic reactions, resulting in the formation of electron-hole pairs. The crystal structure of Bi_2O_3 contains oxygen vacancies, which lead to the

generation of reactive oxygen species (ROS) that enhance its antibacterial properties. Through photocatalytic processes, Bi_2O_3 can degrade pollutants and bolster its antibacterial effects. Various synthesis techniques offer the ability to manipulate the properties of Bi_2O_3 nanoparticles. Due to its perceived lower toxicity, Bi_2O_3 demonstrates promise for environmental applications. In conclusion, the distinctive attributes of Bi_2O_3 render it a versatile material suitable for diverse uses in environmental and biomedical fields. The interest in bismuth oxide has surged among researchers due to its valuable properties. Wise publications on bismuth oxide in various research groups can be observed in Figure I.2, with the data being gathered from the Web of Science.[16]

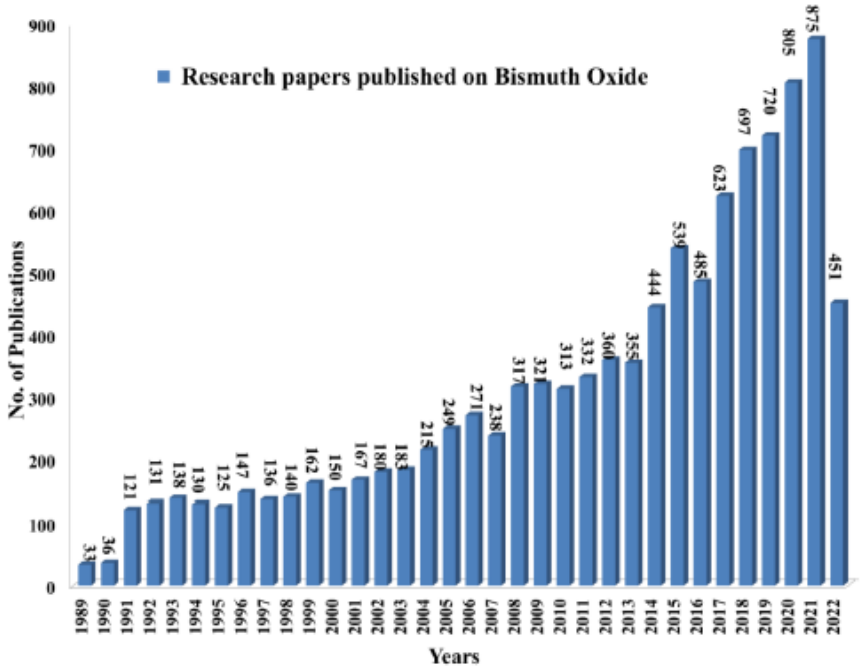

Figure I.2: Yearly publications focused on the compound bismuth oxide [16].

I.1.3.Composites:

The composite of $Bi_2O_3/BiFeO_3$ system has been investigated and synthesized using various approach by researchers. Shi et al [17] synthesized this system using conventional sol-gel method. A conventional melt method also has been used to fabricate this composite by Margha et al, they used it for photocatalytic degradation of bisphenol A [18]. It also has been prepared by hydrothermal approach to study the effect of both Bi_2O_3 and Fe_2O_3 phases as impurities on the electrical properties [19]. $Bi_2O_3/BiFeO_3$ films has been produced for photoelectrochemical applications by Yan et al [20].

I.2. Synthesis methods:

I.2.1. Sol-gel:

Originating from the sequential chemical and physical transitions of hydrolysis, polymerization, gelation, condensation, desiccation, and densification, the term "sol-gel" encapsulates the fundamental mechanism of its formation. This process is characterized by the initial dispersion of nanoscale entities, whether individual molecules or minute particles, within a liquid phase (the sol). Subsequently, under meticulously controlled environmental conditions, these dispersed units undergo a process of aggregation and interlinking, ultimately self-assembling into a continuous, interconnected macroscopic architecture – the gel state[21]. This technique represents a straightforward approach for fabricating nano and microstructures of superior quality. It offers various benefits compared to alternative synthesis pathways, including the ability to regulate the texture, dimensions, and surface characteristics of the substances. Moreover, it is characterized by its simplicity of execution, cost-effectiveness, excellent quality, and capability to generate materials with extensive surface areas[22]. The high level of flexibility and simplicity exhibited by this method contributes significantly to its widespread popularity in the manufacturing of nanoscale powders[23], [24]. and its extensive utilization as a method for applying a protective layer[25], [26] .

I.2.2. Co-precipitation synthesis:

Co-precipitation method is employed for the fabrication of nanoscale metal oxide entities and hybrid metal-ceramic architectures frequently. The ultimate dimensions and morphology of the resultant nanoparticles are critically modulated by an array of operational parameters, notably the initial reactant concentrations, the imposed pH environment, and the thermal energy input. Mechanistically, this methodology commences with the dissolution of precursor materials, typically in chloride or nitrate form, within a solvent system to yield a uniformly dispersed molecular mixture. Subsequently, the controlled introduction of a basic agent, such as sodium hydroxide or ammonium hydroxide, into this homogeneous solution induces the formation of insoluble hydroxide compounds, leading to precipitation. Following a purification stage involving the removal of extraneous ionic species via washing, a thermal processing step is applied to facilitate the transformation of the precipitated salts into the desired metal oxide nanoparticles [27].

I.2.3. Solid state synthesis:

Solid-state synthesis fundamentally relies on the thermally activated interaction of precursor solids maintained at elevated temperatures for a predetermined duration. The precise thermal regime and temporal parameters governing the synthesis are contingent upon a complex interplay of variables. Consequently, a comprehensive understanding of these influential factors is indispensable for the rational design of a successful solid-state synthetic route capable of yielding the targeted material with the intended characteristic[28].

I.2.4. Green synthesis:

In the field of materials science, the concept of "green" synthesis has garnered considerable attention due to its reputation as a dependable, sustainable, and environmentally friendly protocol for the production of a diverse array of materials/nanomaterials, which includes metal/metal oxides nanomaterials, hybrid materials, and bioinspired materials. Consequently, green synthesis is recognized as a crucial tool in mitigating the detrimental consequences linked to conventional synthesis methods employed for nanoparticles in both laboratory and industrial settings. Within this analysis, the foundational procedures and mechanisms of "green" synthesis methods, particularly focusing on metal and metal oxide nanoparticles like gold (Au), silver (Ag), copper oxide (CuO), and zinc oxide (ZnO), utilizing natural extracts were outlined. Notably, an investigation was conducted into the involvement of biological elements, essential phytochemicals such as flavonoids, alkaloids, terpenoids, amides, and aldehydes, serving as reducing agents and solvent systems. Furthermore, the examination extended to the evaluation of nanoparticle stability/toxicity and the relevant surface engineering strategies employed to ensure biocompatibility. Lastly, the discourse encompassed the applications of these synthesized products in environmental remediation, specifically addressing antimicrobial properties, catalytic performance, elimination of pollutant dyes, and detection of heavy metal ions[29].

I.2.5. Microwave assisted synthesis:

Microwave (MW) chemistry, a burgeoning field of investigation with expanding practical applications, constitutes an emergent methodology within green chemistry synthesis. This innovative technique operates through the selective perturbation of matter at the atomic and molecular levels, facilitating processes of self-organization and assembly[30], [31] [32]. Microwave-assisted synthesis is considered to be environmentally friendly and, as such, aligns with the fundamental principles of green chemistry. This method of energy utilization has been extensively and effectively utilized in the realm of organic synthesis, particularly in the context of metal-catalyzed synthetic processes. Nevertheless, its application in the synthesis of metal complexes has not been as widely embraced. The efficacy of microwave irradiation as a time-efficient technique and an alternative approach for challenging transformations has been increasingly demonstrated, offering potential benefits for inorganic chemists as well[33].

I.2.6. Sunlight-driven ingnition synthesis:

The synthesis of metal oxide nanostructures via combustion routes is a highly promising approach due to its simplicity, speed, scalability, and cost-effectiveness [34]. The solar irradiance incident upon Earth encompasses a broad spectral range, extending from the far ultraviolet to the infrared region. Although far-UV photons would have been attenuated by atmospheric constituents, a significantly greater proportion of the photochemically relevant near-UV spectrum permeated the early terrestrial environment. Despite its inherent benefits relative to thermal and electrical discharge energy inputs, solar radiation has not been as thoroughly investigated within origin-of-life research paradigms. Given that photochemical

processes are predicated on molecular photon absorption, their efficacy is critically contingent upon the energy, wavelength, and photon flux characteristics of the incident radiation. In laboratory investigations, monochromatic or narrow-bandwidth light sources are frequently employed, delivering a limited selection of wavelengths. This spectral constraint may not optimally align with the absorption profile of the target molecule, potentially skewing chemical reaction pathways and product yields. Consequently, the utilization of broadband radiation sources, such as xenon arc lamps, to emulate the solar spectral output in experimental simulations would likely yield more geochemically plausible photochemical outcomes relevant to prebiotic chemistry[35]. Utilizing sunlight as a sustainable energy source serves not only to trigger the combustion process but also to induce the formation of oxygen vacancies on the surface of metal oxides [34].

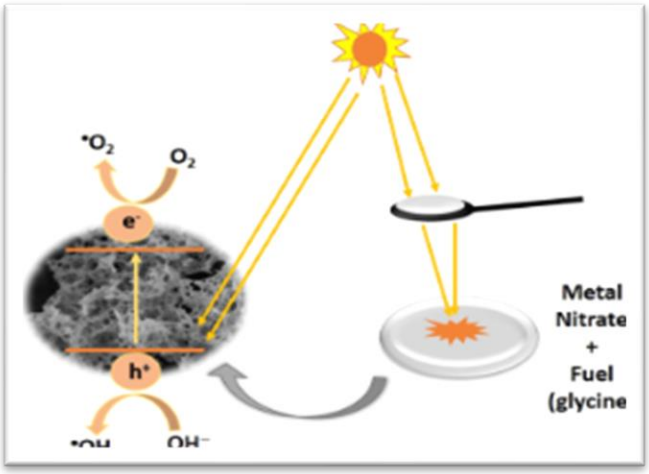

Figure I.3: Schema of sunlight-driven ingnition synthesis[34].

I.2.7. Hydrothermal:

Hydrothermal synthesis represents one of the most frequently employed techniques for the production of nanomaterials. Essentially, it involves a solution-based reaction methodology. Within the realm of hydrothermal synthesis, nanomaterial formation can occur over a broad spectrum of temperatures ranging from ambient conditions to elevated levels. In order to govern the morphology of the envisaged materials, researchers can opt for either low-pressure or high-pressure environments, contingent upon the vapor pressure of the primary constituent in the reaction. Numerous categories of nanomaterials have been effectively fabricated using this particular approach. The hydrothermal synthesis method boasts notable advantages when compared to alternative methodologies[36].

I.2.8. Autocombustion:

Combustion synthesis presents a facile and cost-effective methodology for the generation of nanomaterials, enabling the fabrication of nanostructured ceramics, composites, alloys, and intermetallic compounds [37]. The underlying principle involves the thermal initiation of an exothermic reaction that subsequently proceeds in a self-sustaining manner. Depending on the physical state of the initial reactants [38].

Solution combustion synthesis (SCS) systems are categorized based on the chemical identities of the fuel, oxidizer, and solvent (Table I.1) [39].

Table I.1: Common constituents for autocombustion solution preparation[40], [41], [42].

Oxidizer	Fuel	Solvent
Metal nitrates or nitrate hydrates: $Me^{\upsilon}(NO_3).nH_2O$ υ-metal valence	Urea (CH_4N_2O)	Water (H_2O)
	Glycine ($C_2H_5NO_2$)	Hydrocarbons:
	Sucrose ($C_{12}H_{22}O_{11}$)	Kerosene
	Glucose ($C_6H_{12}O_6$)	Benzene (C_6H_6)
	Citric Acid ($C_6H_8O_7$)	Alcohols:
Ammonium based nitrate (NH_4NO_3)	Hydrazine based fuels:	Ethanol (C_2H_6O)
	Carbohydrazide (CH_6N_4O)	Methanol (CH_4O)
	Oxalyldihydrazide ($C_2H_6N_4O_2$)	Furfuryl alcohol ($C_5H_6O_2$)
Nitric acid (HNO_3)	Hexamethylenetetramine ($C_6H_{12}N_4$)	2-methoxyethanol ($C_3H_8O_2$)
	Acetylacetone ($C_5H_8O_2$)	Formaldehyde (CH_2O)

Typically, diverse organic fuels or their combinations are dissolved in a solvent alongside metal nitrate hydrates. The widespread use of nitrate salts as oxidizers is likely attributable to their favorable aqueous solubility and comparatively low thermal decomposition temperatures, which facilitate the generation of reactive oxygen species. For instance, aluminum nitrate nonahydrate, $Al(NO_3)_3{\cdot}9H_2O$, decomposes at approximately 130 °C, whereas the decomposition onset for aluminum sulfate, $Al_2(SO_4)_3$, occurs around 600 °C. Furthermore, the solubility of nitrates in water at ambient temperature (~64 wt %) surpasses that of corresponding sulfates (~27 wt %). In instances where nitrates are unavailable, alternative metallic precursors (such as hydroxides) can be dissolved in nitric acid, or ammonium nitrate may serve as the oxidizer [43], [44]. Table I.1 enumerates the most frequently employed fuels in SCS reactions. These compounds act as sources of carbon and hydrogen and often exhibit the capacity to form complexes with metal cations, thereby promoting homogeneous cation distribution within solutions or gels. An ideal fuel should possess high solvent solubility, a low decomposition temperature (below 400 °C), leave no residual mass, exhibit compatibility with metal nitrates (avoiding explosive reactions), and be readily obtainable or easily synthesized. Water is the predominant solvent in SCS research; however, kerosene [45], [46], alcohols [40], [47], [48], [49], [50], or formaldehyde [51] are occasionally utilized.It is established that SCS, along with other combustion synthesis methodologies, can be executed in two distinct regimes [52], [53], [54]. The first, termed volume combustion or thermal explosion, involves the uniform preheating of the entire reactive mixture to the solvent's boiling point. This is followed by a sustained isothermal phase during which free and a portion of bound water evaporate. A subsequent preheating stage exhibits an accelerated rate, culminating at an ignition temperature (Tig) where the temperature abruptly escalates to a maximum value (Tm), followed by a cooling phase. Conversely, the self-propagating combustion mode entails the localized heating of a small volume (~1 mm^3) within the reactive solutions or gels to initiate the exothermic reaction [55], which then propagates autonomously throughout the remaining volume as a combustion wave [56]. The corresponding time-temperature profile reveals a comparatively abbreviated preheating stage in contrast to the volume combustion scenario[39].

I.3. Application:

I.3.1. Photocatalysis:

Photocatalysis process uses photocatalyst materials to benefit from light, these are microscopic semiconductors that absorb light, allowing them to act as catalysts in beneficial processes like pollution control and generating clean energy[57], [58]. Photocatalysts work much better than larger materials because they have a special structure with a lot more surface area. This extra surface lets them do their job better[59], [60]. Precise control over the shape and size of photocatalytic materials at the nanoscale enables the design and fabrication of novel materials with tailored properties for innovative applications. Furthermore, green photoactive nanoparticles can be synthesized from diverse biological sources such as plant materials and microorganisms. This approach offers an environmentally friendly, biocompatible, and cost-effective synthesis strategy[61], [62]. Green synthesis of nanophotocatalysts offers a double benefit: it boosts their catalytic activity while eliminating the need for expensive and hazardous chemicals, making the process more sustainable and safer[63], [64]. Eco-friendly nanoparticle production is gaining momentum with two main approaches: using diverse bacteria to create valuable metals and semiconducting oxides, and leveraging safe and easy-to-handle plant extracts. These methods eliminate the need for harsh chemicals. Photocatalysis, a pollution-fighting process powered by abundant and clean sunlight, holds promise for the future. Not only is light a sustainable resource, but it can also trigger highly selective reactions for efficient environmental cleanup[65], [66]. Photocatalysis offers a promising technique for eliminating persistent organic contaminants with ease[67]. Light-powered pollution breakdown demands next-generation photoactive nanomaterials to generate potent ROS (reactive oxygen species) for efficient organic contaminant oxidation[68], [69], [70]. Sunlight is a vital source of energy for humans, delivered by a continuous stream of electromagnetic waves reaching Earth's surface.

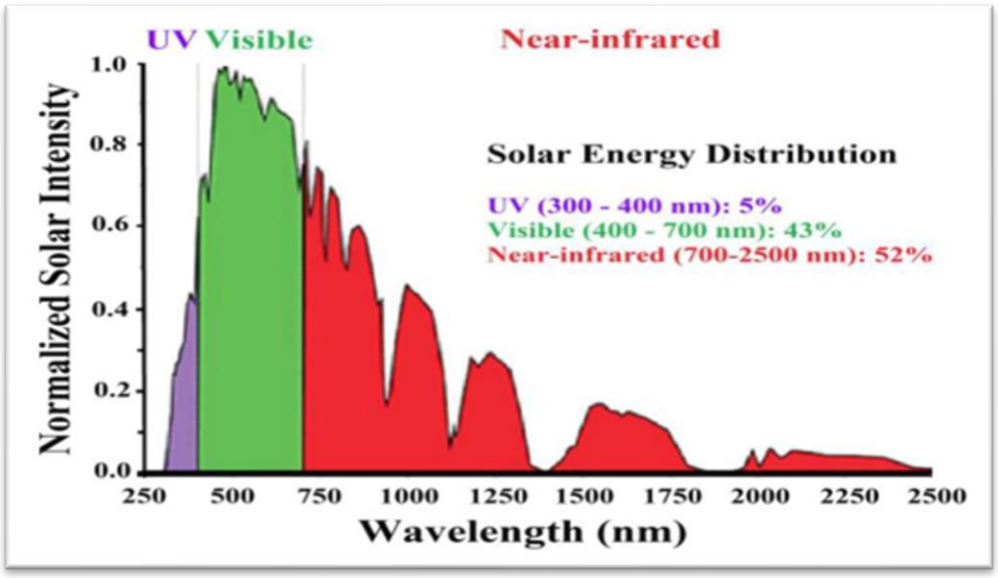

Figure I.4: The spectrum of solar energy [71].

While only a small fraction of the Sun's immense energy output (384.6 yottawatts) reaches Earth, our planet still receives a significant amount (1368 W/m²) at its current distance [72], [73]. Despite Earth receiving a substantial 1000 W/m² due to atmospheric filtering, the real hurdle lies in efficiently capturing and harnessing this abundant solar energy. The main challenge is efficiently capturing and utilizing this abundant resource[74].

I.3.1.1. Photocatalytic degradation of toxic organic compounds:

The economic boom of industrialization has left a dark stain on our environment. Air and water pollution, dwindling resources, and climate change are grim reminders of the price paid for progress. Uncontrolled release of pollutants like dyes, chemicals, and heavy metals only worsens the situation. However, there's a ray of hope: Advanced Oxidation Processes (AOPs) are gaining traction as a powerful tool for environmental remediation[75]. One promising method for cleaning up persistent pollutants involves heterogeneous photocatalysis. This technique uses semiconductor materials and light sources to break down pollutants into harmless byproducts. Here's how it works: when light with the right amount of energy shines on the semiconductor, it excites an electron, pushing it from the valence band to the conduction band. This creates a "hole" where the electron used to be. These excited electrons and holes (called charge carriers) kickstart the pollutant degradation process. The hole reacts with water molecules on the surface, generating powerful hydroxyl radicals. Meanwhile, the excited electron interacts with oxygen to form superoxide radicals or hydroperoxyl radicals. These highly reactive oxygen species (ROS), along with the free electrons and holes, then attack the pollutant molecules adsorbed on the surface, transforming them into safe products[76].

$$\text{Semiconductor} + h\nu \rightarrow h^+ + e^-$$

$$e^- + h^+ \rightarrow \text{energy}$$

$$h^+ + H_2O \rightarrow {\bullet}OH + H^+$$

$$e^- + O_2 \rightarrow {\bullet}O_2^-$$

A photocatalytic reaction's success hinges on two main factors: the photocatalyst's ability to create long-lasting electrons and holes, and the type of material used. Additionally, various operational parameters like solution acidity/alkalinity (pH), light exposure time, and the presence of "sacrificial donors" (molecules that readily give up electrons) influence efficiency. Even the physical form of the photocatalyst (powder or immobilized) plays a role. Degrading complex organic pollutants (containing elements like C, N, O, S, Cl) is particularly challenging. Each carbon atom in these pollutants needs a specific number of electrons and holes to completely break down into harmless CO_2. This high demand for electrons and holes limits the effectiveness of photocatalysis for these large molecules. Here's the breakdown: photo-generated charges act like tiny scissors, progressively chopping the pollutant into smaller pieces through complex electron transfer reactions. This makes photocatalysis more efficient for simpler pollutants with only one carbon atom, like formic acid or methanol. For larger, tough[77], [78], [79], [80]er molecules, scientists are exploring combining photocatalysis with other methods like strong oxidants (ozone, persulfate, hydrogen peroxide) to achieve complete

mineralization[77], [78], [79], [80]. A major hurdle in pollution cleanup technologies is ensuring complete breakdown of pollutants. Unfortunately, many studies only track the conversion of the target pollutant into smaller molecules (intermediates), which can still be harmful. This approach neglects to measure how much is actually transformed into harmless carbon dioxide (CO_2)[81].

I.3.1.2. Photocatalysis with nitrobenzene:

Nitrobenzene's molecular architecture comprises a benzene ring bearing one nitro substituent (Figure I.5). This compound presents as a viscous yellow liquid characterized by an odor reminiscent of bitter almonds. Alternative designations for nitrobenzene include oil of mirbane, essence of mirbane, nitrobenzol, and solvent black 6 [82].

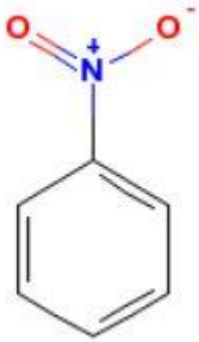

Figure I.5: Nitrobenzene structure [82].

Key physical and chemical characteristics of nitrobenzene are detailed below (National Library of Medicine's [NLM] Hazardous Substances Data Bank, 2003; World Health Organization [IPCS], 2003; Agency for Toxic Substances and Disease Registry [ATSDR], 1990) [82]:

Chemical formula: $C_6H_5NO_2$

Molecular weight: 123.11 g/mol

Melting point: 5.7°C

Boiling point: 210.8°C

Density: 1.2 g/mL (at 20°C)

Water solubility: 1,900 mg/L (at 20°C)

Vapor pressure 0.15 mm Hg at 25°C (20 Pa at 20°C).

Nitroaromatic compounds are a rising star among the cast of environmental villains, contributing significantly to the global challenge of organic contaminant pollution[83], [84]. Nitroaromatic compounds raise serious environmental concerns due to their toxic and mutagenic properties. These compounds are particularly troublesome because they are highly stable, difficult to dissolve in water (low solubility), and widely used as industrial raw materials, making them prevalent in our environment[85]. To achieve complete breakdown of these contaminants into harmless products like carbon dioxide, nitrogen oxides, and water, scientists have explored various oxidation processes[86]. Traditional oxidation methods struggle to completely break down these persistent nitroaromatic compounds. Therefore, researchers are exploring alternative, greener solutions. One promising approach is the conversion of these pollutants into valuable products. Aromatic amines, for instance, serve as crucial building blocks for dyes, polymers, and various life-science products like antioxidants, pharmaceuticals, and even agrochemicals[87], [88], [89], [90]. Nitroaromatic compounds can be converted into aromatic amines through reduction reactions.

I.3.2. Catalysis:

The term "catalysis" was introduced in 1835 thanks to Swedish chemist Berzelius. However, a more precise definition came much later, in 1894, from Ostwald. He described a catalyst as a substance that speeds up a slow chemical reaction without being consumed itself. Today, this principle is well understood by students: a catalyst lowers the activation energy needed for a reaction to occur, often by interacting with the reactant molecules. While it participates in the reaction, it remains intact and can transform many reactant molecules. Therefore, only a small amount of catalyst is needed to convert a large quantity of reactants. However, basic textbooks rarely delve deeper into the mechanisms of catalysis, despite its key role in chemistry. In fact, most chemical compounds involve one or more catalytic steps during their production[91]. While many surface science techniques were valuable, they had a major limitation: they only functioned effectively in extremely low-pressure environments (high vacuum). This meant the observed conditions were far removed from real-world applications, where reactions occur at normal pressures and temperatures. As a result, researchers focused on developing techniques that could bridge this "pressure gap" and operate under conditions relevant to practical uses[92].

I.3.2.1. Mixed oxides catalysts:

Y. Sim et al [93] systematically evaluated the performance of different ABO_3 perovskite catalysts in the oxidative coupling of methane (OCM) reaction, identified distinct trends in their activity based on the substituted metal, and delved into the underlying mechanism by highlighting the crucial role of surface and bulk oxygen species, oxygen vacancies, and ultimately, oxygen ion conductivity as key determinants of methane conversion. Their research yielded several key findings:

Initially, a blank test confirmed minimal methane conversion and negligible C_2 yield under the reaction conditions, establishing the necessity of the catalysts.

The study then revealed a distinct catalytic behavior among the different ABO_3 catalyst groups (I, II, and III) concerning methane conversion and C_2 selectivity as the atomic number of the substituted metal element increased.

- Methane Conversion: Showed a decreasing trend for Group I, an increasing trend for Group III, and a parabolic (upward convex) trend for Group II.
- C_2 Selectivity: Displayed a decreasing trend for Groups I and III, and a parabolic (downward convex) trend for Group II.

Despite these varying trends, the researcher noted that all investigated ABO_3 catalysts exhibited significant C_2 yields in the OCM reaction. Specifically, $LaAlO_3$ demonstrated the highest C_2 yield in Groups I and II due to its superior methane conversion and C_2 selectivity. In Group III, $CaZrO_3$, with good C_2 selectivity, outperformed $SrZrO_3$ and $BaZrO_3$ in terms of C_2 yield.

To understand these catalytic activities, the researcher focused on the relationship between surface oxygen species and methane conversion. Drawing on existing literature, they highlighted the role of selective oxygen species in abstracting hydrogen from methane to form methyl radicals, which subsequently dimerize to C_2 hydrocarbons in the gas phase. The reaction of methane with surface oxygen was identified as the rate-determining step.

The study further explored the role of oxygen vacancies created during this reaction and their subsequent refilling by gas-phase oxygen adsorption and bulk lattice oxygen. The researcher presumed that both adsorbed surface oxygen and bulk lattice oxygen contribute to replenishing these vacancies, emphasizing that a fast oxygen cycle is crucial for high methane conversion. This conclusion was supported by their previous work, which demonstrated a significantly faster OCM reaction and higher methane conversion in the presence of gaseous oxygen.

Consequently, the researcher inferred that facile release of surface oxygen and rapid refilling of oxygen vacancies are essential for achieving high methane conversion. This implies that oxygen ion conductivity within the catalyst is a critical factor directly related to methane conversion, suggesting its potential as an indicator for estimating conversion rates.

Finally, recognizing that the oxygen ion conductivity of perovskites is strongly influenced by their structural properties, the researcher proposed that investigating these structural properties could predict oxygen ion conductivity and further confirm its dependency on methane conversion.

I.3.3. Hydrogen production:

Hydrogen possesses the capacity to offer environmentally friendly, effective, dependable, and cost-effective solutions in various application domains, yielding notable societal advantages.[94] It has been documented in academic literature that the utilization of hydrogen has the potential to facilitate extensive adoption and complete integration of renewable energy resources.[95] On the end-user (service) side, hydrogen serves as a crucial counterpart to electricity for the purpose of storing intermittent renewable energy sources,

thereby representing a significant advancement in the transition towards environmental sustainability within energy systems.[96] The literature documents that hydrogen has the potential to satisfy 18% of the ultimate energy requirements, leading to a reduction of 6 gigatons of annual CO_2 emissions, and facilitating the generation of 30 million fresh employment opportunities by the year 2050.[97] The literature additionally demonstrates that hydrogen has the potential to fuel more than 400 million cars, 15 to 20 million trucks, and approximately 5 million buses by the year 2050, constituting approximately 20 to 25% of the transportation sector.[98] In addition to its notable economic and environmental advantages, it is anticipated that hydrogen energy systems will achieve greater efficiencies in the forthcoming period.[99] The literature demonstrates that hydrogen is perceived as the linchpin for sustainable development and a resolution to the challenges of global warming [100]. Despite its cosmic abundance, elemental hydrogen is not readily available on Earth and necessitates extraction from hydrogen-containing compounds like water and natural gas. Diverse resources, including water, fossil fuels, and biomass, can serve as feedstocks for hydrogen production via various processes such as water electrolysis or high-temperature thermochemical water splitting. This multiplicity of production pathways contributes to hydrogen's significance as an energy vector. However, the overall energy efficiency and environmental footprint of a hydrogen economy are intrinsically linked to the chosen production method, making its selection a complex consideration. Several prevalent hydrogen production methods might be mentioned such as: production from fossil fuels, natural gas reforming, coal gasification, water splitting, water electrolysis, high-temperature electrolysis, photoelectrolysis (photolysis), Solar thermochemical hydrogen, photobiological production (biophotolysis) and biomass conversion.

I.3.3.1. Catalytic hydrogen production:

Numerous research studies have been conducted on the topic of hydrogen research and development alongside fuel cell technology (Figure I.6). In order to promote the integration of H_2 in forthcoming energy systems, investigations into catalyst development (encompassing electro-, photo-, bio-, and chemical catalysis) play a crucial role in the hydrogen economy. This involves assessing the efficiency of various methods for hydrogen production and the utilization of H_2 in fuel cells for generating clean electricity and heat. Today, steam methane reforming is employed for the large-scale production of H_2 owing to its cost-effectiveness and technological advancement. In the upcoming time, novel approaches and their integration will likely revolutionize the current practices.

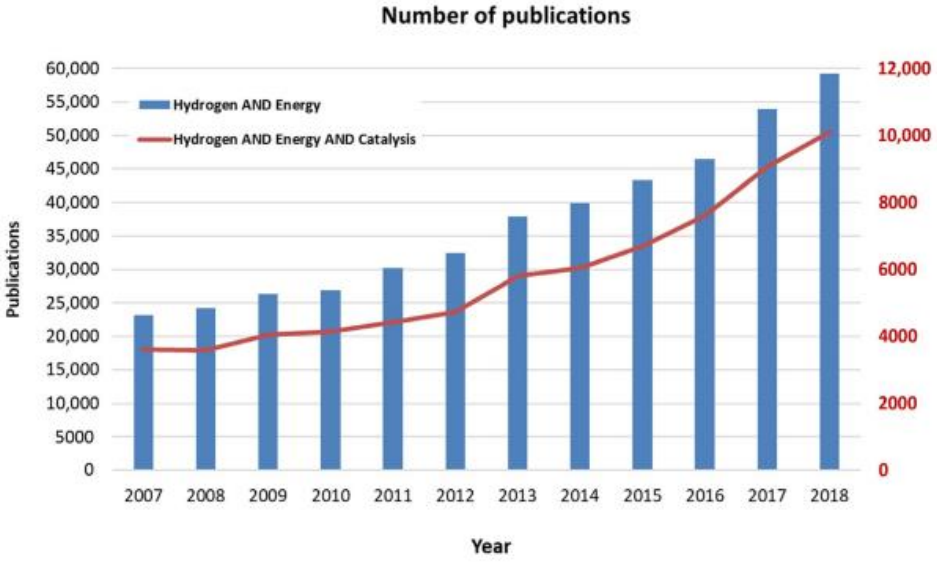

Figure I.6: The quantity of scientific publications within the ScienceDirect repository that have been released between the years 2007 and 2018, utilizing the search terms "Hydrogen and Energy" as well as "Hydrogen and Energy and Catalysis," was examined (accessed on January 21, 2019).

The integration of renewable sources into the pool of resources will enhance the sustainability of this hydrogen production technology.[101] Cleaner production is increasingly recognized as global regulations restrict the utilization of fossil fuels in the forthcoming period. This encompasses, to some extent, bio-based fuels like bioethanol. The generation of hydrogen can stem from sustainable raw materials like water, compounds derived from biomass, and various types of waste or byproducts from industries (e.g., organic compounds). Nonetheless, advancements in process and reactor technologies are crucial to enhance the overall efficiency of the process. Advanced techniques, such as membrane-supported reformers and electrochemical reactors, are employed to enhance the efficiency of energy, separation, and purification of streams rich in H_2.[101], [102]

I.3.3.2. Sodium Borohydride Hydrolysis:

Hydrogen has been regarded as one of the most viable alternatives to fossil fuels in recent years due to its cleanliness and energy-carrying capacity, stemming from the increased demand for energy and exacerbated environmental harm.[103] Furthermore, the chemical energy per unit mass of hydrogen, amounting to 142 MJ/kg, surpasses that of any other fuel by nearly threefold. For instance, the chemical energy per unit mass of hydrocarbons stands at 47 MJ/kg.[104]**.** In the initial years of the 21st century, sodium borohydride ($NaBH_4$) gained recognition as a prospective material for hydrogen storage in proton exchange membrane fuel cells and direct borohydride fuel cell systems. Possessing a theoretical hydrogen storage capacity by weight of 10.8%, $NaBH_4$ demonstrates notable controllability in its hydrolysis and yields hydrogen of high purity. The stoichiometric representation of the ideal hydrolysis of $NaBH_4$ is as follows [105]:

$$NaBH_4+2H_2O \longrightarrow NaBO_2+4H_2 \ \Delta H=217kJmol^{-1} \qquad (1)$$

In recent times, there has been a notable shift in attention among a number of researchers towards the examination of the hydrolysis process of MgH_2 as an example. This particular compound has traditionally been regarded as one of the most efficient metal hydrides for such reactions. Despite its slightly lower hydrogen storage capacity at 7.6 wt.%, when compared to $NaBH_4$ and NH_3BH_3, MgH_2 stands out for its relatively economical nature [106]. When considering stoichiometric water, it has been documented that the hydrogen production from the hydrolysis process of MgH_2 amounts to 6.4 weight percent [107]. Moreover, owing to the robust reducibility of MgH_2, the hydrogen production can achieve up to 15.2% wt.% when it undergoes a chemical reaction with water at ambient temperature, as illustrated in Equation (2), making it notably suitable for hydrogen supply in fuel cells, especially when the water mass is not taken into consideration [108].

$$MgH_2 + 2H_2O \rightarrow Mg(OH)_2 + 2H_2 \uparrow \Delta H = -277 \text{ kJ/mol} \qquad (2)$$

I.3.3.3. Sodium Borohydride methanolysis:

In variety forms of hydrogen storage.[109] a chemical hydride possessing a high capacity for storing hydrogen by weight and ensuring operational safety represents an optimal choice for the controlled release of H_2 as needed.[110] In the 1950s, Schlesinger initially suggested the utilization of sodium borohydride ($NaBH_4$) for the generation of H_2 under normal environmental conditions.[111] $NaBH_4$ methanolysis begin to be considered as viable technologies for the production of hydrogen since 2010, which is extensively acknowledged as the fundamental basis of the studies conducted on $NaBH_4$ as materials for storing H_2.[112] The H_2 molecule effectively liberates energy through the process of electron oxidation reaction within proton-exchange membrane fuel cells [113]**.**

$$NaBH_4+4CH_3OH \longrightarrow NaB(OCH_3)_4+4H_2 \qquad (3)$$

The methanolysis process as denoted by Equation (3) is being discussed.[114] Four moles of hydrogen molecules are produced from one mole of sodium borohydride (NaBH4), resulting in the formation of sodium metaborate $NaB(OCH_3)_4$ as a byproduct with the presence of methanol as a sacrificial agent[115], [116].

I.3.3.4. Hydrogen production by photocatalysis:

In contemporary times, a primary technological obstacle researchers confront pertains to ensuring a sustainable provision of clean energy. The consumption of energy worldwide has experienced a substantial increase over the past few decades. Consequently, the necessity arises for the advancement of energy production technologies that rely on renewable sources due to the gradual exhaustion of fossil fuel deposits and the adverse ecological repercussions associated with their utilization. Out of the various available alternatives, solar energy stands out as the most extensive renewable energy reservoir. The daily solar energy output (1022 J) significantly surpasses the current global annual energy requirements[117]. The necessity of capturing and transforming solar energy into a suitable energy form, be it electricity, chemicals,

or fuels, has instigated extensive research efforts in this domain. Various approaches have been devised over recent decades. The technology of photovoltaic cells facilitates the conversion of solar energy into electrical power, a process that has been commercialized and seen a significant enhancement in efficiency, surpassing the notable threshold of 20%. Despite advancements in smart grids and new battery technologies, the lack of efficient large-scale energy storage remains a significant constraint. Conversely, the conversion of solar energy into chemical energy to produce renewable fuels, known as "solar fuels," offers clear advantages for practical applications. In this context, the direct conversion of solar energy into chemical energy can be achieved through two distinct pathways: a) converting CO_2 into hydrocarbons (e.g., methane, methanol, ethanol, etc.) and b) generating H_2. Hydrogen (H_2), a clean fuel source, holds potential as an optimal energy carrier. When combined with oxygen in a Fuel Cell, the chemical energy stored in the H-H bond is released, yielding only water. Nonetheless, several challenges must be addressed before the global transition to a new energy landscape can occur. Among these challenges, establishing an efficient H_2 production process that aligns with industrial requirements stands out as a critical endeavor. Ideally, such a method should ensure a sustainable supply of H_2, while considering environmental factors such as minimizing or eliminating waste products, with a specific focus on reducing CO_2 emissions or other greenhouse gases (GHG). Various process technologies have been proposed thus far, encompassing thermal chemical, chemical, biological, electrolytic, photoelectrolytic, and photocatalytic processes. These processes rely on carbon-containing feedstocks (fossil fuels, biomass, wastes) or water as the source of hydrogen[118]. At present, the predominant method for generating H_2 involves the utilization of natural gas in conjunction with the steam reforming of methane (SRM). This is subsequently accompanied by the water-gas shift reaction (WGS) which capitalizes on the CO generated in the initial phase to enhance the production of H_2 [119]. However, this methodology is not deemed sustainable due to the limited availability of fossil fuels and the generation of CO_2, a prominent greenhouse gas responsible for global warming. The majority of the aforementioned techniques necessitate elevated pressures and temperatures, the imposition of an external bias, or the utilization of non-renewable H_2 resources. Among these methods, photocatalytic processes utilizing solar radiation and H_2O or potentially sustainable raw materials offer clear benefits and have garnered considerable attention in recent years. Recent research indicates that H_2 production through solar-driven approaches shows promising competitiveness when compared to traditional methods relying on non-renewable sources[120].

References:

[1] P. Cousin and R. A. Ross, “Preparation of Mixed Oxides: a Review,” 1990.

[2] R. Amigó, J. Asenjo, E. Krotenko, F. Torres, J. Tejada, and E. Brillas, “Electrochemical synthesis of new magnetic mixed oxides of Sr and Fe: Composition, magnetic properties, and microstructure,” *Chemistry of Materials*, vol. 12, no. 2, pp. 573–579, Feb. 2000, doi: 10.1021/cm991159h.

[3] J. A. Rodriguez, J. C. Hanson, S. Chaturvedi, A. Maiti, and J. L. Brito, “Phase transformations and electronic properties in mixed-metal oxides: Experimental and theoretical studies on the behavior of NiMoO4 and MgMoO4,” *Journal of Chemical Physics*, vol. 112, no. 2, pp. 935–945, Jan. 2000, doi: 10.1063/1.480619.

[4] D. Heinz, W. F. Hoelderich, S. Krill, W. Boeck, and K. Huthmacher, “V2O5/TiO2 Catalysts for the Vapor-Phase Oxidation of β-Picoline: Influence of the TiO2-Carrier,” *J Catal*, vol. 192, no. 1, pp. 1–10, May 2000, doi: 10.1006/jcat.1999.2658.

[5] H. Watanabe and Y. Koyasu, “New synthesis route for Mo-V-Nb-Te mixed oxides catalyst for propane ammoxidation,” 2000.

[6] A. Coma, “Inorganic Solid Acids and Their Use in Acid-Catalyzed Hydrocarbon Reactions,” 1995.

[7] D. Kiessling, G. Wendt, K. Hagenau, and R. Schoellner, “Dimerization of n-butenes on amorphous NiO-A12Off SiO2 catalysts,” 1991.

[8] B. F. Kubel and H. Schmid, “Nonstoichiometry and Crystal Structures of Barium-Bismuth Oxides,” 1985.

[9] K. Y. Yun, M. Noda, M. Okuyama, H. Saeki, H. Tabata, and K. Saito, “Structural and multiferroic properties of BiFeO3 thin films at room temperature,” *J Appl Phys*, vol. 96, no. 6, pp. 3399–3403, Sep. 2004, doi: 10.1063/1.1775045.

[10] J. Wu and J. Wang, “BiFeO3 thin films of (1 1 1)-orientation deposited on SrRuO3 buffered Pt/TiO2/SiO2/Si(1 0 0) substrates,” *Acta Mater*, vol. 58, no. 5, pp. 1688–1697, Mar. 2010, doi: 10.1016/j.actamat.2009.11.011.

[11] M. I. Morozov, N. A. Lomanova, and V. V Gusarov, “Specific Features of BiFeO 3 Formation in a Mixture of Bismuth(III) and Iron(III) Oxides,” 2003.

[12] M. Valant, A.-K. Axelsson, and N. Alford, “Peculiarities of a Solid-State Synthesis of Multiferroic Polycrystalline BiFeO 3,” 2007, doi: 10.1021/cm071730.

[13] J. Silva, A. Reyes, H. Esparza, H. Camacho, and L. Fuentes, “BiFeO3: A review on synthesis, doping and crystal structure,” in *Integrated Ferroelectrics*, 2011, pp. 47–59. doi: 10.1080/10584587.2011.574986.

[14] J. Silva, A. Reyes, H. Esparza, H. Camacho, and L. Fuentes, "BiFeO3: A review on synthesis, doping and crystal structure," in *Integrated Ferroelectrics*, 2011, pp. 47–59. doi: 10.1080/10584587.2011.574986.

[15] R. P. Gupta, W. S. Khokle, J. P. Pachauri, C. C. Tripathi, B. C. Pathak, and G. S. Virdi, "Fluorine-implanted bismuth oxide superconductors," *Appl Phys Lett*, vol. 54, no. 6, pp. 570–571, 1989, doi: 10.1063/1.101459.

[16] V. Mane, D. Dake, N. Raskar, R. Sonpir, E. Stathatos, and B. Dole, "A review on Bi2O3 nanomaterial for photocatalytic and antibacterial applications," Jun. 01, 2024, *Elsevier B.V.* doi: 10.1016/j.chphi.2024.100517.

[17] Y. Shi *et al.*, "Bi2O3/BiFeO3 heterostructure: preparation, characterization, and photocatalytic activity," *Chemical Papers*, vol. 72, no. 6, pp. 1327–1337, Jun. 2018, doi: 10.1007/s11696-018-0384-z.

[18] F. H. Margha, E. K. Radwan, M. I. Badawy, and T. A. Gad-Allah, "Bi2O3-BiFeO3Glass-Ceramic: Controllable β-/γ-Bi2O3Transformation and Application as Magnetic Solar-Driven Photocatalyst for Water Decontamination," *ACS Omega*, vol. 5, no. 24, pp. 14625–14634, Jun. 2020, doi: 10.1021/acsomega.0c01307.

[19] C. Casut, I. Malaescu, C. N. Marin, and M. Miclau, "The Effect of Bi2O3 and Fe2O3 Impurity Phases in BiFeO3 Perovskite Materials on Some Electrical Properties in the Low-Frequency Field," *Materials*, vol. 15, no. 14, Jul. 2022, doi: 10.3390/ma15144764.

[20] X. Yan *et al.*, "Design and fabrication of Bi2O3/BiFeO3 heterojunction film with improved photoelectrochemical performance," *Appl Surf Sci*, vol. 552, Jun. 2021, doi: 10.1016/j.apsusc.2021.149442.

[21] A. Shah, S. N. F. Ismail, M. A. Hasan, and R. Daud, "Surface Modification on Titanium Alloy for Biomedical Applications," in *Encyclopedia of Smart Materials*, A.-G. Olabi, Ed., Oxford: Elsevier, 2018, pp. 436–444. doi: https://doi.org/10.1016/B978-0-12-803581-8.10484-9.

[22] A. E. Danks, S. R. Hall, and Z. Schnepp, "The evolution of 'sol-gel' chemistry as a technique for materials synthesis," *Mater Horiz*, vol. 3, no. 2, pp. 91–112, Mar. 2016, doi: 10.1039/c5mh00260e.

[23] M. Fu, Y. Li, S. Wu, P. Lu, J. Liu, and F. Dong, "Sol-gel preparation and enhanced photocatalytic performance of Cu-doped ZnO nanoparticles," *Appl Surf Sci*, vol. 258, no. 4, pp. 1587–1591, Dec. 2011, doi: 10.1016/j.apsusc.2011.10.003.

[24] C.-Q. Ye, "Sol-Gel Processes of Functional Powders and Films," in *Chemical Reactions in Inorganic Chemistry*, InTech, 2018. doi: 10.5772/intechopen.69588.

[25] V. Purcar *et al.*, "Investigation of Hybrid Films Based on Fluorinated Silica Materials Prepared by Sol–Gel Processing," *Coatings*, vol. 12, no. 10, Oct. 2022, doi: 10.3390/coatings12101595.

[26] K. Harun, N. Mansor, Z. A. Ahmad, and A. A. Mohamad, "Electronic Properties of ZnO Nanoparticles Synthesized by Sol-gel Method: A LDA+U Calculation and Experimental Study," *Procedia Chem*, vol. 19, pp. 125–132, 2016, doi: 10.1016/j.proche.2016.03.125.

[27] A. Ahmad, I. Ahmad, S. Ramzan, M. Z. Kiyani, D. Dubal, and N. M. Mubarak, "5 - Nanomaterial synthesis protocols," in *Nanomedicine Manufacturing and Applications*, F. Verpoort, I. Ahmad, A. Ahmad, A. Khan, and C. Y. Chee, Eds., Elsevier, 2021, pp. 73–85. doi: https://doi.org/10.1016/B978-0-12-820773-4.00010-X.

[28] V. Grover, B. P. Mandal, and A. K. Tyagi, "Solid State Synthesis of Materials," in *Handbook on Synthesis Strategies for Advanced Materials : Volume-I: Techniques and Fundamentals*, A. K. Tyagi and R. S. Ningthoujam, Eds., Singapore: Springer Singapore, 2021, pp. 1–49. doi: 10.1007/978-981-16-1807-9_1.

[29] S. Ying *et al.*, "Green synthesis of nanoparticles: Current developments and limitations," May 01, 2022, *Elsevier B.V.* doi: 10.1016/j.eti.2022.102336.

[30] W. Ao *et al.*, "Microwave assisted preparation of activated carbon from biomass: A review," Sep. 01, 2018, *Elsevier Ltd*. doi: 10.1016/j.rser.2018.04.051.

[31] G. Kiani, A. Nourizad, and R. Nosrati, "Application of microwave-assisted synthesized leaf-like ZnO nanosheets as the ethanol sensor," *Scientia Iranica*, vol. 26, no. 6F, pp. 3889–3895, 2019, doi: 10.24200/sci.2019.51664.2300.

[32] A. Kumar, Y. Kuang, Z. Liang, and X. Sun, "Microwave chemistry, recent advancements, and eco-friendly microwave-assisted synthesis of nanoarchitectures and their applications: a review," *Mater Today Nano*, vol. 11, p. 100076, 2020, doi: https://doi.org/10.1016/j.mtnano.2020.100076.

[33] E. Gabano and M. Ravera, "Microwave-Assisted Synthesis: Can Transition Metal Complexes Take Advantage of This 'Green' Method?," Jul. 01, 2022, *MDPI*. doi: 10.3390/molecules27134249.

[34] A. Hezam *et al.*, "Sunlight-Driven Combustion Synthesis of Defective Metal Oxide Nanostructures with Enhanced Photocatalytic Activity," *ACS Omega*, vol. 4, no. 24, pp. 20595–20605, Dec. 2019, doi: 10.1021/acsomega.9b02564.

[35] R. J. Rapf and V. Vaida, "Sunlight as an energetic driver in the synthesis of molecules necessary for life," *Physical Chemistry Chemical Physics*, vol. 18, no. 30, pp. 20067–20084, 2016, doi: 10.1039/C6CP00980H.

[36] Y. X. Gan, A. H. Jayatissa, Z. Yu, X. Chen, and M. Li, "Hydrothermal Synthesis of Nanomaterials," 2020, *Hindawi Limited*. doi: 10.1155/2020/8917013.

[37] K. C. Patil, S. T. Aruna, and S. Ekambaram, "Combustion synthesis," *Curr Opin Solid State Mater Sci*, vol. 2, no. 2, pp. 158–165, 1997, doi: https://doi.org/10.1016/S1359-0286(97)80060-5.

[38] K. Ravichandran, P. K. Praseetha, T. Arun, and S. Gobalakrishnan, "Synthesis of Nanocomposites," in *Synthesis of Inorganic Nanomaterials: Advances and Key Technologies*, Elsevier, 2018, pp. 141–168. doi: 10.1016/B978-0-08-101975-7.00006-3.

[39] A. Varma, A. S. Mukasyan, A. S. Rogachev, and K. V. Manukyan, "Solution Combustion Synthesis of Nanoscale Materials," Dec. 14, 2016, *American Chemical Society*. doi: 10.1021/acs.chemrev.6b00279.

[40] X. Yu *et al.*, "Spray-combustion synthesis: Efficient solution route to high-performance oxide transistors," *Proc Natl Acad Sci U S A*, vol. 112, no. 11, pp. 3217–3222, Mar. 2015, doi: 10.1073/pnas.1501548112.

[41] M. G. Kim, M. G. Kanatzidis, A. Facchetti, and T. J. Marks, "Low-temperature fabrication of high-performance metal oxide thin-film electronics via combustion processing," *Nat Mater*, vol. 10, no. 5, pp. 382–388, 2011, doi: 10.1038/nmat3011.

[42] K. C. Patil, S. T. Aruna, and T. Mimani, "Combustion synthesis: An update," *Curr Opin Solid State Mater Sci*, vol. 6, no. 6, pp. 507–512, 2002, doi: 10.1016/S1359-0286(02)00123-7.

[43] C.-C. Hwang, J.-S. Tsai, T.-H. Huang, C.-H. Peng, and S.-Y. Chen, "Combustion synthesis of Ni–Zn ferrite powder—influence of oxygen balance value," *J Solid State Chem*, vol. 178, no. 1, pp. 382–389, 2005, doi: https://doi.org/10.1016/j.jssc.2004.10.045.

[44] A. Cross *et al.*, "In Situ Preparation of Highly Stable Ni-Based Supported Catalysts by Solution Combustion Synthesis," *The Journal of Physical Chemistry C*, vol. 118, no. 45, pp. 26191–26198, Nov. 2014, doi: 10.1021/jp508546n.

[45] T. Tani, N. Watanabe, K. Takatori, and S. E. Pratsinis, "Morphology of oxide particles made by the emulsion combustion method," *Journal of the American Ceramic Society*, vol. 86, no. 6, pp. 898–904, 2003, doi: 10.1111/j.1151-2916.2003.tb03394.x.

[46] K. Takatori, T. Tani, N. Watanabe, and N. Kamiya, "Preparation and characterization of nano-structured ceramic powders synthesized by emulsion combustion method," 1999.

[47] C. Gomez-Solís *et al.*, "Rapid synthesis of ZnO nano-corncobs from Nital solution and its application in the photodegradation of methyl orange," *J Photochem Photobiol A Chem*, vol. 298, pp. 49–54, Feb. 2015, doi: 10.1016/j.jphotochem.2014.10.012.

[48] A. A. Voskanyan and K. Y. Chan, "Solution combustion synthesis using furfuryl alcohol as fuel and a combustible solvent," *J Exp Nanosci*, vol. 10, no. 6, pp. 466–475, Apr. 2015, doi: 10.1080/17458080.2013.843028.

[49] S. Ilić *et al.*, “Sol-gel synthesis and characterization of iron doped mullite,” Nov. 05, 2014, *Elsevier Ltd*. doi: 10.1016/j.jallcom.2014.05.204.

[50] R. Branquinho *et al.*, “Towards environmental friendly solution-based ZTO/AlOx TFTs,” *Semicond Sci Technol*, vol. 30, no. 2, p. 024007, 2015, doi: 10.1088/0268-1242/30/2/024007.

[51] K. Prabhakaran, J. Joseph, N. M. Gokhale, S. C. Sharma, and R. Lal, “Synthesis of nanocrystalline lanthanum strontium manganite powder by the urea-formaldehyde polymer gel combustion route,” *Journal of the American Ceramic Society*, vol. 89, no. 7, pp. 2335–2337, Jul. 2006, doi: 10.1111/j.1551-2916.2006.01013.x.

[52] A. S. Mukasyan and P. Dinka, “Novel approaches to solution-combustion synthesis of nanomaterials,” *International Journal of Self-Propagating High-Temperature Synthesis*, vol. 16, no. 1, pp. 23–35, Mar. 2007, doi: 10.3103/s1061386207010049.

[53] R. Ianoş, I. Lazău, C. Păcurariu, and P. Barvinschi, “Fuel mixture approach for solution combustion synthesis of Ca3Al2O6 powders,” *Cem Concr Res*, vol. 39, no. 7, pp. 566–572, Jul. 2009, doi: 10.1016/j.cemconres.2009.03.014.

[54] K. Deshpande, A. Mukasyan, and A. Varma, “Direct Synthesis of Iron Oxide Nanopowders by the Combustion Approach: Reaction Mechanism and Properties,” *Chemistry of Materials*, vol. 16, no. 24, pp. 4896–4904, Nov. 2004, doi: 10.1021/cm040061m.

[55] K. V Manukyan *et al.*, “Solution Combustion Synthesis of Nano-Crystalline Metallic Materials: Mechanistic Studies,” *The Journal of Physical Chemistry C*, vol. 117, no. 46, pp. 24417–24427, Nov. 2013, doi: 10.1021/jp408260m.

[56] A. S. Mukasyan, C. Costello, K. P. Sherlock, D. Lafarga, and A. Varma, “Perovskite membranes by aqueous combustion synthesis: synthesis and properties,” 2001. [Online]. Available: www.elsevier.com

[57] M. A. Hassaan *et al.*, “Techno-economic analysis of ZnO nanoparticles pretreatments for biogas production from barley straw,” *Energies (Basel)*, vol. 13, no. 18, Oct. 2020, doi: 10.3390/en13195001.

[58] A. Saravanan, P. S. Kumar, S. Jeevanantham, M. Anubha, and S. Jayashree, “Degradation of toxic agrochemicals and pharmaceutical pollutants: Effective and alternative approaches toward photocatalysis,” *Environmental Pollution*, vol. 298, p. 118844, 2022, doi: https://doi.org/10.1016/j.envpol.2022.118844.

[59] M. A. Hassaan, M. A. El-Nemr, M. R. Elkatory, S. Ragab, V. C. Niculescu, and A. El Nemr, “Principles of Photocatalysts and Their Different Applications: A Review,” Dec. 01, 2023, *Springer Science and Business Media Deutschland GmbH*. doi: 10.1007/s41061-023-00444-7.

[60] Y. Yin, H. Chen, and Q. Yuan, “Strain-induced bandgap engineering in C3N nanotubes,” *Chem Phys Lett*, vol. 768, p. 138390, 2021, doi: https://doi.org/10.1016/j.cplett.2021.138390.

[61] N. G. Sarath, A. M. Shackira, H. A. El-Serehy, D. I. Hefft, and J. T. Puthur, "Phytostabilization of arsenic and associated physio-anatomical changes in Acanthus ilicifolius L," *Environmental Pollution*, vol. 298, p. 118828, 2022, doi: https://doi.org/10.1016/j.envpol.2022.118828.

[62] H. Abdul Salam, R. Sivaraj, and R. Venckatesh, "Green synthesis and characterization of zinc oxide nanoparticles from Ocimum basilicum L. var. purpurascens Benth.-Lamiaceae leaf extract," *Mater Lett*, vol. 131, pp. 16–18, 2014, doi: https://doi.org/10.1016/j.matlet.2014.05.033.

[63] T. Miyata, H. Tokunaga, K. Watanabe, N. Ikenaga, and T. Minami, "Photovoltaic properties of low-damage magnetron-sputtered n-type ZnO thin film/p-type Cu2O sheet heterojunction solar cells," *Thin Solid Films*, vol. 697, p. 137825, 2020, doi: https://doi.org/10.1016/j.tsf.2020.137825.

[64] H. Agarwal, S. Venkat Kumar, and S. Rajeshkumar, "A review on green synthesis of zinc oxide nanoparticles – An eco-friendly approach," *Resource-Efficient Technologies*, vol. 3, no. 4, pp. 406–413, 2017, doi: https://doi.org/10.1016/j.reffit.2017.03.002.

[65] L. L. Chng, N. Erathodiyil, and J. Y. Ying, "Nanostructured Catalysts for Organic Transformations," *Acc Chem Res*, vol. 46, no. 8, pp. 1825–1837, Aug. 2013, doi: 10.1021/ar300197s.

[66] C. S. Turchi and D. F. Ollis, "Photocatalytic degradation of organic water contaminants: Mechanisms involving hydroxyl radical attack," *J Catal*, vol. 122, no. 1, pp. 178–192, 1990, doi: https://doi.org/10.1016/0021-9517(90)90269-P.

[67] X. Zhang, Y. L. Chen, R.-S. Liu, and D. P. Tsai, "Plasmonic photocatalysis," *Reports on Progress in Physics*, vol. 76, no. 4, p. 046401, 2013, doi: 10.1088/0034-4885/76/4/046401.

[68] "S135964620800715X".

[69] Z. Mirzaeifard, Z. Shariatinia, M. Jourshabani, and S. M. Rezaei Darvishi, "ZnO Photocatalyst Revisited: Effective Photocatalytic Degradation of Emerging Contaminants Using S-Doped ZnO Nanoparticles under Visible Light Radiation," *Ind Eng Chem Res*, vol. 59, no. 36, pp. 15894–15911, Sep. 2020, doi: 10.1021/acs.iecr.0c03192.

[70] M. R. Hoffmann, S. T. Martin, W. Choi, and D. W. Bahnemann, "Environmental Applications of Semiconductor Photocatalysis," *Chem Rev*, vol. 95, no. 1, pp. 69–96, Jan. 1995, doi: 10.1021/cr00033a004.

[71] M. A. Hassaan *et al.*, "Techno-economic analysis of ZnO nanoparticles pretreatments for biogas production from barley straw," *Energies (Basel)*, vol. 13, no. 18, Oct. 2020, doi: 10.3390/en13195001.

[72] M. A. Hassaan *et al.*, "Techno-economic analysis of ZnO nanoparticles pretreatments for biogas production from barley straw," *Energies (Basel)*, vol. 13, no. 18, Oct. 2020, doi: 10.3390/en13195001.

[73] B. Janani *et al.*, "CuO loaded ZnS nanoflower entrapped on PVA-chitosan matrix for boosted visible light photocatalysis for tetracycline degradation and anti-bacterial application," *J Environ Manage*, vol. 306, Mar. 2022, doi: 10.1016/j.jenvman.2021.114396.

[74] M. A. Hassaan, M. A. El-Nemr, M. R. Elkatory, S. Ragab, V. C. Niculescu, and A. El Nemr, "Principles of Photocatalysts and Their Different Applications: A Review," Dec. 01, 2023, *Springer Science and Business Media Deutschland GmbH*. doi: 10.1007/s41061-023-00444-7.

[75] G. Ramalingam, N. Perumal, A. K. Priya, and S. Rajendran, "A review of graphene-based semiconductors for photocatalytic degradation of pollutants in wastewater," *Chemosphere*, vol. 300, p. 134391, 2022, doi: https://doi.org/10.1016/j.chemosphere.2022.134391.

[76] M. Pavel, C. Anastasescu, R. N. State, A. Vasile, F. Papa, and I. Balint, "Photocatalytic Degradation of Organic and Inorganic Pollutants to Harmless End Products: Assessment of Practical Application Potential for Water and Air Cleaning," Feb. 01, 2023, *MDPI*. doi: 10.3390/catal13020380.

[77] E. Gabano and M. Ravera, "Microwave-Assisted Synthesis: Can Transition Metal Complexes Take Advantage of This 'Green' Method?," Jul. 01, 2022, *MDPI*. doi: 10.3390/molecules27134249.

[78] S. Mirsadeghi, H. Zandavar, H. R. Rajabi, F. Sajadiasl, M. R. Ganjali, and S. M. Pourmortazavi, "Superior degradation of organic pollutants and H2O2 generation ability on environmentally-sound constructed Fe3O4-Cu nanocomposite," *Journal of Materials Research and Technology*, vol. 14, pp. 808–821, 2021, doi: https://doi.org/10.1016/j.jmrt.2021.07.007.

[79] W. Kang *et al.*, "Photocatalytic ozonation of organic pollutants in wastewater using a flowing through reactor," *J Hazard Mater*, vol. 405, p. 124277, 2021, doi: https://doi.org/10.1016/j.jhazmat.2020.124277.

[80] S. Preda *et al.*, "Iron-Modified Titanate Nanorods for Oxidation of Aqueous Ammonia Using Combined Treatment with Ozone and Solar Light Irradiation," *Catalysts*, vol. 12, no. 6, Jun. 2022, doi: 10.3390/catal12060666.

[81] M. Pavel, C. Anastasescu, R. N. State, A. Vasile, F. Papa, and I. Balint, "Photocatalytic Degradation of Organic and Inorganic Pollutants to Harmless End Products: Assessment of Practical Application Potential for Water and Air Cleaning," Feb. 01, 2023, *MDPI*. doi: 10.3390/catal13020380.

[82] U. EPA ORD NCEA Integrated Risk Information System, "TOXICOLOGICAL REVIEW OF NITROBENZENE In Support of Summary Information on the Integrated Risk Information System (IRIS)," 2009. [Online]. Available: www.epa.gov/iris

[83] W. Navarra, O. Sacco, V. Venditto, and V. Vaiano, "Selective Photocatalytic Reduction of Nitrobenzene to Aniline Using TiO2 Embedded in sPS Aerogel," *Polymers (Basel)*, vol. 15, no. 2, Jan. 2023, doi: 10.3390/polym15020359.

[84] K.-S. Ju and R. E. Parales, "Nitroaromatic Compounds, from Synthesis to Biodegradation," *Microbiology and Molecular Biology Reviews*, vol. 74, no. 2, pp. 250–272, Jun. 2010, doi: 10.1128/mmbr.00006-10.

[85] W. Navarra, O. Sacco, V. Venditto, and V. Vaiano, "Selective Photocatalytic Reduction of Nitrobenzene to Aniline Using TiO2 Embedded in sPS Aerogel," *Polymers (Basel)*, vol. 15, no. 2, Jan. 2023, doi: 10.3390/polym15020359.

[86] P. Bose, W. H. Glaze, and D. S. Maddox, "DEGRADATION OF RDX BY VARIOUS ADVANCED OXIDATION PROCESSES: II. ORGANIC BY-PRODUCTS," *Water Res*, vol. 32, no. 4, pp. 1005–1018, 1998, doi: https://doi.org/10.1016/S0043-1354(97)00308-4.

[87] S. Paganelli, A. Angi, N. Pajer, and O. Piccolo, "A smart heterogeneous catalyst for efficient, chemo-and stereoselective hydrogenation of 3-hexyn-1-ol," *Catalysts*, vol. 11, no. 1, pp. 1–9, Jan. 2021, doi: 10.3390/catal11010014.

[88] W. Navarra, O. Sacco, V. Venditto, and V. Vaiano, "Selective Photocatalytic Reduction of Nitrobenzene to Aniline Using TiO2 Embedded in sPS Aerogel," *Polymers (Basel)*, vol. 15, no. 2, Jan. 2023, doi: 10.3390/polym15020359.

[89] H. Ding, J. Liu, X. Shen, and H. Li, "Advances in the Preparation of Tough Conductive Hydrogels for Flexible Sensors," Oct. 01, 2023, *Multidisciplinary Digital Publishing Institute (MDPI)*. doi: 10.3390/polym15194001.

[90] C. Fleischmann, M. Lievenbrück, and H. Ritter, "Polymers and dyes: Developments and applications," 2015, *MDPI AG*. doi: 10.3390/polym7040717.

[91] "19536798".

[92] J. Schnadt *et al.*, "Interplay of adsorbate-adsorbate and adsorbate-substrate interactions in self-assembled molecular surface nanostructures," *Nano Res*, vol. 3, no. 7, pp. 459–471, 2010, doi: 10.1007/s12274-010-0005-9.

[93] Y. Sim, D. Kwon, S. An, J. M. Ha, T. S. Oh, and J. C. Jung, "Catalytic behavior of ABO3 perovskites in the oxidative coupling of methane," *Molecular Catalysis*, vol. 489, Jun. 2020, doi: 10.1016/j.mcat.2020.110925.

[94] Y. Kalinci, A. Hepbasli, and I. Dincer, "Techno-economic analysis of a stand-alone hybrid renewable energy system with hydrogen production and storage options," *Int J Hydrogen Energy*, vol. 40, no. 24, pp. 7652–7664, Jun. 2015, doi: 10.1016/j.ijhydene.2014.10.147.

[95] A. K. Singh, S. Singh, and A. Kumar, "Hydrogen energy future with formic acid: a renewable chemical hydrogen storage system," *Catal Sci Technol*, vol. 6, no. 1, pp. 12–40, 2016, doi: 10.1039/C5CY01276G.

[96] G. Cipriani *et al.*, "Perspective on hydrogen energy carrier and its automotive applications," *Int J Hydrogen Energy*, vol. 39, no. 16, pp. 8482–8494, 2014, doi: https://doi.org/10.1016/j.ijhydene.2014.03.174.

[97] T. S. Uyar and D. Beşikci, "Integration of hydrogen energy systems into renewable energy systems for better design of 100% renewable energy communities," *Int J Hydrogen Energy*, vol. 42, no. 4, pp. 2453–2456, 2017, doi: https://doi.org/10.1016/j.ijhydene.2016.09.086.

[98] A. Mostafaeipour *et al.*, "Evaluating the wind energy potential for hydrogen production: A case study," *Int J Hydrogen Energy*, vol. 41, no. 15, pp. 6200–6210, 2016, doi: https://doi.org/10.1016/j.ijhydene.2016.03.038.

[99] A. Nakamura *et al.*, "A 24.4% solar to hydrogen energy conversion efficiency by combining concentrator photovoltaic modules and electrochemical cells," *Applied Physics Express*, vol. 8, no. 10, Oct. 2015, doi: 10.7567/APEX.8.107101.

[100] E. López González, F. Isorna Llerena, M. Silva Pérez, F. Rosa Iglesias, and J. Guerra Macho, "Energy evaluation of a solar hydrogen storage facility: Comparison with other electrical energy storage technologies," *Int J Hydrogen Energy*, vol. 40, no. 15, pp. 5518–5525, 2015, doi: https://doi.org/10.1016/j.ijhydene.2015.01.181.

[101] I. Dincer and C. Acar, "Innovation in hydrogen production," *Int J Hydrogen Energy*, vol. 42, no. 22, pp. 14843–14864, 2017, doi: https://doi.org/10.1016/j.ijhydene.2017.04.107.

[102] Y. Ben Smida, R. Marzouki, S. Kaya, S. Erkan, M. Faouzi Zid, and A. Hichem Hamzaoui, "Synthesis Methods in Solid-State Chemistry," in *Synthesis Methods and Crystallization*, IntechOpen, 2020. doi: 10.5772/intechopen.93337.

[103] A. Balbay and C. Saka, "The effect of the concentration of hydrochloric acid and acetic acid aqueous solution for fast hydrogen production from methanol solution of NaBH4," *Int J Hydrogen Energy*, vol. 43, no. 31, pp. 14265–14272, Aug. 2018, doi: 10.1016/j.ijhydene.2018.05.131.

[104] L. Schlapbach and A. Züttel, "Hydrogen-storage materials for mobile applications," 2001. [Online]. Available: www.nature.com

[105] W. Chen *et al.*, "Hydrolysis and regeneration of sodium borohydride (NaBH4) – A combination of hydrogen production and storage," *J Power Sources*, vol. 359, pp. 400–407, 2017, doi: 10.1016/j.jpowsour.2017.05.075.

[106] Q. Luo, J. Li, B. Li, B. Liu, H. Shao, and Q. Li, "Kinetics in Mg-based hydrogen storage materials: Enhancement and mechanism," *Journal of Magnesium and Alloys*, vol. 7, no. 1, pp. 58–71, 2019, doi: https://doi.org/10.1016/j.jma.2018.12.001.

[107] J. P. Tessier, P. Palau, J. Huot, R. Schulz, and D. Guay, "Hydrogen production and crystal structure of ball-milled MgH2-Ca and MgH2-CaH2 mixtures," *J Alloys Compd*, vol. 376, no. 1–2, pp. 180–185, Aug. 2004, doi: 10.1016/j.jallcom.2003.12.013.

[108] X. Xie *et al.*, "Recent advances in hydrogen generation process via hydrolysis of Mg-based materials: A short review," *J Alloys Compd*, vol. 816, p. 152634, 2020, doi: https://doi.org/10.1016/j.jallcom.2019.152634.

[109] J. M. Ogden, T. G. Kreutz, and M. M. Steinbugler, "Fuels for fuel cell vehicles," *Fuel Cells Bulletin*, vol. 3, no. 16, pp. 5–13, 2000, doi: https://doi.org/10.1016/S1464-2859(00)86613-4.

[110] J. O. Abe, A. P. I. Popoola, E. Ajenifuja, and O. M. Popoola, "Hydrogen energy, economy and storage: Review and recommendation," *Int J Hydrogen Energy*, vol. 44, no. 29, pp. 15072–15086, 2019, doi: https://doi.org/10.1016/j.ijhydene.2019.04.068.

[111] W. Schlesinger and H. M. Leeper, "Gutta. I. Single crystals of alpha-gutta," *Journal of Polymer Science*, vol. 11, no. 3, pp. 203–213, Sep. 1953, doi: 10.1002/pol.1953.120110302.

[112] M. S. İzgi, Ö. Şahin, and C. Saka, "Hydrogen production from NaBH4 using Co–Cu–B catalysts prepared in methanol: Effect of plasma treatment," *Int J Hydrogen Energy*, vol. 41, no. 3, pp. 1600–1608, 2016, doi: https://doi.org/10.1016/j.ijhydene.2015.11.004.

[113] B. H. Liu and Z. P. Li, "A review: Hydrogen generation from borohydride hydrolysis reaction," *J Power Sources*, vol. 187, no. 2, pp. 527–534, 2009, doi: https://doi.org/10.1016/j.jpowsour.2008.11.032.

[114] E. Y. Marrero-Alfonso, J. R. Gray, T. A. Davis, and M. A. Matthews, "Minimizing water utilization in hydrolysis of sodium borohydride: The role of sodium metaborate hydrates," *Int J Hydrogen Energy*, vol. 32, no. 18, pp. 4723–4730, 2007, doi: https://doi.org/10.1016/j.ijhydene.2007.08.014.

[115] B. H. Liu and Z. P. Li, "A review: Hydrogen generation from borohydride hydrolysis reaction," *J Power Sources*, vol. 187, no. 2, pp. 527–534, 2009, doi: https://doi.org/10.1016/j.jpowsour.2008.11.032.

[116] Y. Kojima *et al.*, "Hydrogen generation using sodium borohydride solution and metal catalyst coated on metal oxide," *Int J Hydrogen Energy*, vol. 27, no. 10, pp. 1029–1034, 2002, doi: https://doi.org/10.1016/S0360-3199(02)00014-9.

[117] N. S. Lewis and D. G. Nocera, "Powering the planet: Chemical challenges in solar energy utilization," 2006. [Online]. Available: www.pnas.orgcgidoi10.1073pnas.0603395103

[118] M. Ni, D. Y. C. Leung, M. K. H. Leung, and K. Sumathy, “An overview of hydrogen production from biomass,” *Fuel Processing Technology*, vol. 87, no. 5, pp. 461–472, 2006, doi: https://doi.org/10.1016/j.fuproc.2005.11.003.

[119] M. H. Halabi, M. H. J. M. de Croon, J. van der Schaaf, P. D. Cobden, and J. C. Schouten, “Low temperature catalytic methane steam reforming over ceria–zirconia supported rhodium,” *Appl Catal A Gen*, vol. 389, no. 1, pp. 68–79, 2010, doi: https://doi.org/10.1016/j.apcata.2010.09.004.

[120] C. A. Rodriguez, M. A. Modestino, D. Psaltis, and C. Moser, “Design and cost considerations for practical solar-hydrogen generators,” *Energy Environ Sci*, vol. 7, no. 12, pp. 3828–3835, Dec. 2014, doi: 10.1039/c4ee01453g.

CHAPTER II :

SYNTHESIS, CHARACTERIZATION TECHNIQUES AND PHOTOCATALYTIC & CATALYTIC PROCESSES DESCRIPTION

CHAPITER II : SYNTHESIS, CHARACTERIZATION TECHNIQUES AND PHOTOCATALYTIC & CATALYTIC PROCESSES DESCRIPTION

This chapter is devoted primarily to the description of the methods of preparation, second to characterization techniques and thirdly the catalytic tests.

II.1. Synthesis of oxides

Oxide-based materials invariably entail the synthesis of metal oxides, thereby laying the foundational cornerstone upon which subsequent investigations are built **[1]**. Despite its inherent significance, synthesis often assumes a subsidiary role within the broader scope of materials science inquiry, which typically pivots towards the elucidation and delineation of the manifold properties and characterizations inherent to these materials **[2]**. As a corollary, the elucidation and dissemination of synthesis methodologies frequently encounter marginalization within the academic discourse, resulting in scanty and inadequately articulated documentation within the scholarly literature **[3]**. Consequently, for neophyte scientists embarking upon their nascent foray into this domain, the conundrum of selecting the appropriate synthesis pathway and optimal experimental conditions becomes a labyrinthine endeavor, fraught with perplexity **[4]**. Indeed, the meticulous preparation of a pristine, monophasic, and intricate oxide powder, which serves as the bedrock of their scholarly pursuits, necessitates a judicious and discerning approach.

II.1.1.Auto-combustion Synthesis:

Auto-combustion synthesis techniques, as highlighted in various research papers **[5]**, offer a versatile approach in materials science for developing catalysts and photocatalysts that harness solar energy efficiently. Researchers have explored the synthesis of materials like bismuth ferrite ($BiFeO_3$) through auto-combustion methods, demonstrating their potential in photocatalytic applications **[6]**. By combining simple oxides such as Bi_2O_3, mixed oxides like $BiFeO_3$, and composite structures such as $BiFeO_3$-Bi_2O_3, scientists aim to design sustainable and effective materials for catalytic and photocatalytic purposes. The use of auto-combustion techniques enables the precise control over the synthesis process, leading to the creation of nanostructured materials with tailored properties suitable for various applications in renewable energy and environmental remediation.

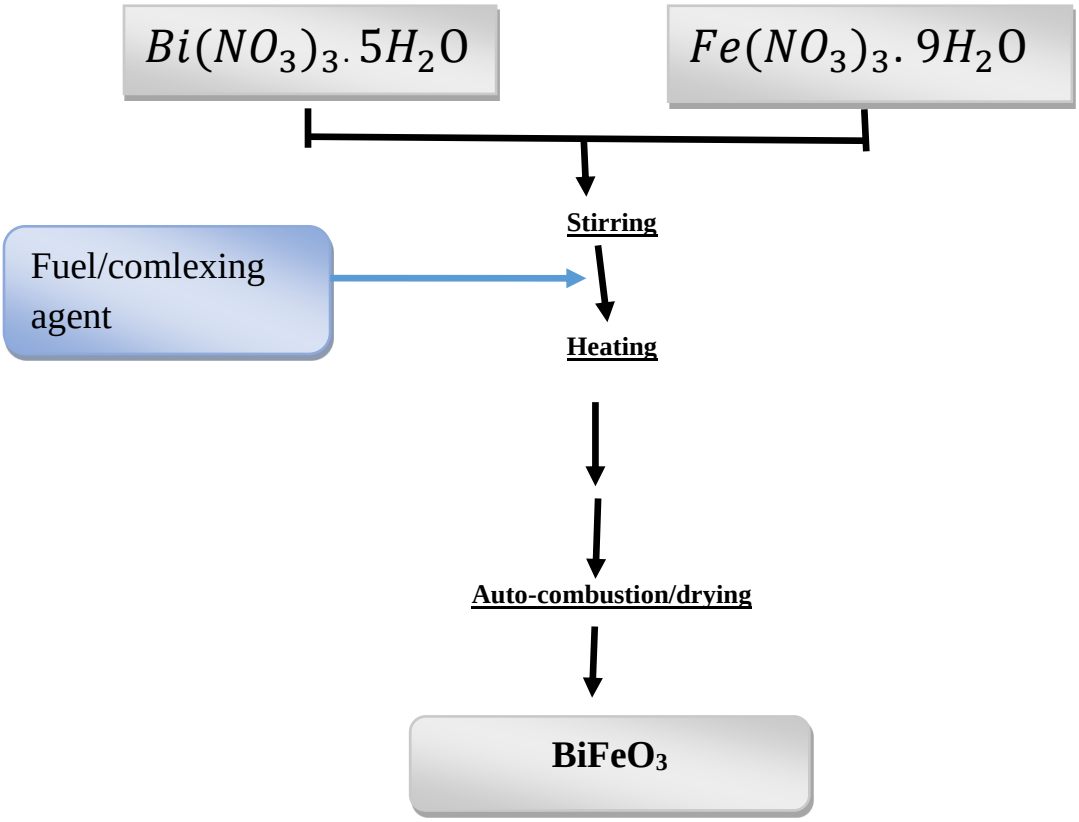

Figure II.1: Scheme of auto-combustion and soft route synthesis of bismuth ferrite **[7]**.

II.2.Characterization Methods

II.2.1 X-ray diffraction

II.2.1.1 Introduction

X-ray diffraction (XRD) stands as an indispensable non-invasive modality in the elucidation of material structures, operating with exquisite efficacy at the atomic or molecular scale. Predominantly tailored for the interrogation of materials evincing crystalline or semi-crystalline attributes, denoting a propensity towards periodic architectural regularity, XRD nonetheless extends its purview to encompass the probing of non-crystalline substrates, thereby amplifying its utility across a diverse spectrum of material compositions and structural motifs.

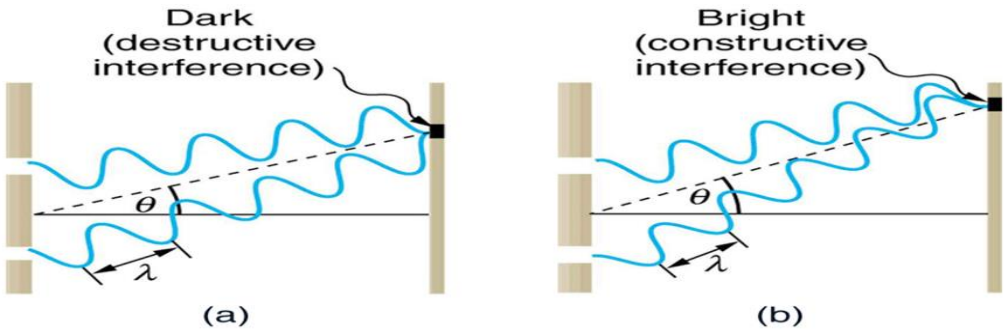

Figure II.2: According to the θ deviation, the phase shift cause constructive **(b)** or destructive **(a)** interferences **[8]**.

This basic technique for the crystallochemical characterization of matter is based on the fact that interatomic distances are of the order of magnitude of X-ray waves (0.2 Å <λ<2 Å) . The spatial periodicity of the crystal structures is the origin of constructive interference of the radiation scattered by the different atoms. X-rays, which are electromagnetic waves, interact with the electrons of atoms. Thus, the results of X-ray diffraction will provide access to electron density maps in the crystal lattice. Indeed, each atom of number Z contains Z electrons, which are distributed around the nucleus. Each electron has its own electron density $\rho(r)_j$ and a form factorF_e . The atomic form factor or atomic diffusion factor is $F_\mathbf{a}$ the sum of the form factors of the electrons of the atom:

$$F_\mathbf{a} = \sum F_e\,(\mathrm{Q}) = \sum \rho(r)_j \,.\, e^{iQr} dV_r$$

The atomic diffusion factor represents the Fourier transform of the electron density of an atom. At a diffraction angle of $2\theta = 0$, the atomic diffusion factor corresponds to the count of Z electrons present. As the diffraction angle rises, $F_\mathbf{a}$ diminishes because of the emergence of destructive interference caused by the spatial distribution of the electron cloud **[9]**.

Over the entire mesh, the amplitude diffracted in a given direction corresponds to the sum of the complex amplitudes $F_\mathbf{a}$ scattered by the atoms. This amplitude diffracted by all the atoms is called structure factor and can be written:

$$F_{hkl} = \sum N_j F_j \exp\,(-B_j(\frac{\sin\theta}{\lambda})^2).\exp\,(i2\pi(hx_j + ky_j + lz_j))$$

With :

- N_j: Number of atoms.
- F_j : Facteur de diffusion de l'atome j.
- $\exp(-B_j\left(\frac{\sin\theta}{\lambda}\right)^2)$: Fourier transform of the Gaussian probability cloud replacing the point position of the atom. and where B_j is the atomic isotropic displacement factor of atom j.
- $\exp\,(i2\pi(hx_j + ky_j + lz_j))$: Phase of the waves scattered with: x_j , y_j ,z_j - reduced coordinates of atom j.

By definition, the diffracted intensity corresponds to the square of the structure factor modulus:

$$I_{hkl} = |F_{hkl}|^2$$

II.2.1.2 Principle

X-ray diffraction (XRD) is a potent analytical method employed for elucidating the crystallographic arrangement of materials through the examination of diffraction patterns generated by the interaction of X-rays with the crystal lattice **[10]**. The foundational concept of XRD relies on Bragg's law, which asserts that X-rays exhibit constructive interference when they strike a crystal lattice at an exact angle, leading to the scattering of X-rays at specific angles corresponding to the separation between crystal planes **[11]**.

II.2.1.3 Apparatus used

XRD Patterns were collected on a Bruker AXS D8- advance diffractometer (LPCMA laboratory, University of Biskra) employing Cu Kα radiation. In all diffractograms, a step size of 0.05° (2θ) was used with a data collection time of 90 minutes.

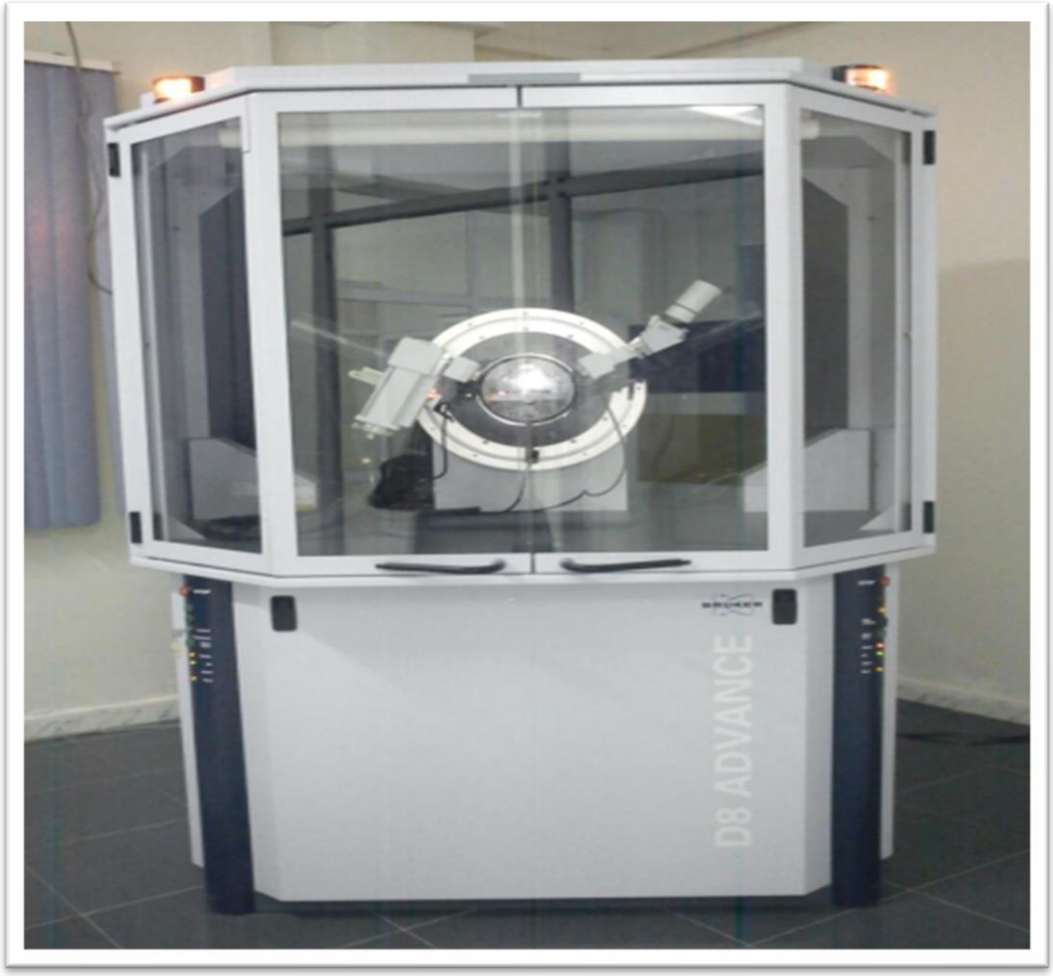

FigureII.3: X-ray Diffractometer equipment **[12]**.

II.2.2 Scanning electron microscopy (SEM) coupled with energy dispersive spectroscopy (EDS)

II.2.2.1 Introduction

The coupling of scanning electron microscopy (SEM) with energy dispersive spectroscopy (EDS) represents a formidable analytical combination, providing deep insights into the microstructural, morphological, and compositional characteristics of various materials. This preliminary discussion seeks to outline the fundamental principles, operational approaches, and wide-ranging applications that highlight the synergy between SEM and EDS, shedding light on their crucial role in the realm of materials analysis and scientific investigation. Fundamentally, SEM utilizes a focused electron beam to examine the surface morphology and topography of samples with exceptional precision and depth **[13]**.

Through scanning the surface of the specimen and identifying the resulting secondary and backscattered electrons, SEM reveals a plethora of structural information ranging from nanoscale attributes to large-scale surface features. This imaging capability makes SEM essential for observing microstructural flaws, surface irregularities, and complex surface structures across a broad spectrum of materials **[14]**.

II.2.2.2 Principle

In the realm of scanning electron microscopy (SEM), a beam of electrons that is highly energetic and focused is employed to scan the specimen, resulting in a significantly magnified image of its morphology, along with insights into its chemical composition facilitated by an energy dispersive spectrometer (EDS) detector **[15]**. The utilization of SEM-EDS is predominantly centered around the characterization of various materials; however, its scope has recently expanded to encompass investigations involving organic-based samples like biological specimens and polymers **[16]**. Microplastics represent hazardous substances that arise not only directly from human activities, but also as a byproduct of the degradation of macroplastics. The contamination stemming from the introduction of micro/nanoplastics into the environment and the subsequent ecological impacts have become prominent topics of contemporary scientific inquiry. As a result, there is a pressing need for specialized methodologies to effectively analyze the morphology and chemical composition of such polymer-derived materials **[17]**.

II.2.2.3 Apparatus used

A scanning electron microscope is a form of microscope that generates images of a specimen's surface through the scanning process using a concentrated beam of accelerated electrons, known as primary electrons (PE). The Zeiss DSM 962 SEM in place is equipped with three detectors as part of its standard setup, enabling the capturing of secondary electrons (SE), backscattering electrons (BSE), and X-ray photons (Xr) that are released by atoms stimulated by the electron beam (Research Center of Semi-conductor Technology for Energy(CRTSE),Algiers).

Figure II.4: SEM with Light Element EDX and Backscatter Detector **[18]**.

II.2.3 Fourier transform infrared (FTIR) spectroscopy

II.2.3.1 Introduction

Infrared spectroscopy has been extensively developed in various forms, primarily utilizing the near or mid infrared regions of the electromagnetic spectrum. Conventional IR spectroscopy employs dispersive apparatus, such as gratings and prisms, with applications typically restricted to gas samples and materials soluble in IR transparent solvents. A notable advancement in contemporary IR spectroscopy is the utilization of Fourier transform infrared (FTIR) methods, significantly broadening the scope of IR technology. These methods have been accessible to researchers since the early 1970s **[19]**. The use of the entire source spectrum provided by an interferometer, as opposed to the individual wavelengths produced by gratings and/or prisms in traditional IR spectroscopy, renders FTIR spectrometers a substantial improvement over dispersive instruments **[19]**. Furthermore, modern FTIR spectrometers are distinguished by their enhanced reliability, speed, cost-effectiveness, and superior performance characteristics, rendering them more favorable than dispersive instruments.

II.2.3.2 Principle

Fourier transform infrared (FTIR) spectroscopy is a methodology utilized for the analysis of the infrared characteristics exhibited by a given specimen. This technique entails the employment of an interferometer to gauge the interferogram signal at the sensor, subsequently subjecting it to Fourier analysis for the derivation of the spectral intensity originating from the source. The widespread application of FTIR spectroscopy across diverse domains like science, engineering, and medicine can be attributed to its non-invasive nature and remarkable sensitivity. Not only does it furnish comprehensive insights into the chemical composition of biological specimens, but it has also proven valuable for the typing and characterization of bacteria. Furthermore, FTIR spectroscopy has demonstrated efficacy in the prompt identification of illicit substances, boasting a high rate of success in distinguishing samples obtained from illicit street sources. Extensive discourse on the principles and equipment utilized in FTIR spectroscopy has been documented, alongside the availability of commercial spectrometers from various suppliers **[20]**. In essence, FTIR spectroscopy stands out as a potent analytical instrument that facilitates a profound comprehension of the infrared attributes intrinsic to diverse specimens.

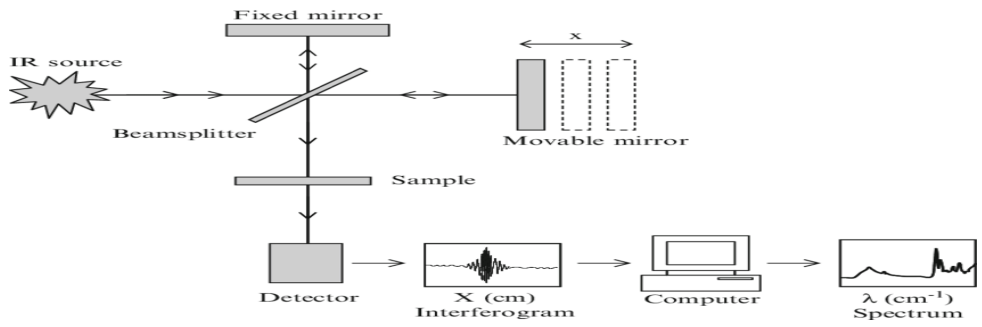

Figure II.5: Schematic sketch of the essential features of a Fourier transform infrared (FTIR) spectrometer **[21]**.

II.2.3.3 Apparatus used

Infrared transmission spectra were performed on a Fourier transform spectrometer (FTIR) Shimadzu 8400S (chemistry laboratory, Department of Material Sciences, University of Biskra). A granular technique employing KBr (1mg of sample added to 200 mg of KBr) was used and the spectra were recorded in the 400-4000 cm-1 range.

Figure II.6: Fourier transform spectrometer (FTIR) Shimadzu 8400S **[22]**.

II.2.1 X-ray photoelectron spectroscopy (XPS)

II.2.4.1 Introduction

X-ray photoelectron spectroscopy (XPS) is a technique that exhibits surface sensitivity in its analytical approach, whereby x-rays are utilized to impact the surface of a substance, subsequently quantifying the kinetic energy of the electrons released. An essential aspect of this method lies in its capability to divulge information regarding the chemical state of the elements within the sample, alongside its proficiency in surface analysis. The scope of detectable elements encompasses all except for hydrogen and helium, thus rendering XPS instrumental in exploring a wide array of materials ranging from plastics and textiles to semiconductors and soil. The significance of surfaces in material interactions can not be understated, as they influence various factors including surface wettability, adhesion, corrosion, charge transfer, and catalysis. Consequently, delving into the study and comprehension of surfaces emerges as a crucial endeavor in scientific inquiry.

The foundation of XPS rests upon the photoelectric effect, initially observed by Heinrich Hertz in 1887, wherein the emission of electrons from surfaces upon light irradiation was noted. Albert Einstein further expounded on this phenomenon in 1905, ultimately receiving the Nobel Prize in physics in 1921 for his contributions. Robinson first documented the utilization of x-ray irradiation for photoemission and Rawlinson in 1914, with the pioneering application of photoemission as an analytical technique credited to Steinhardt and Serfass in 1951 **[23]**. Nonetheless, Kai Siegbahn at the University of Uppsala in Sweden predominantly

accomplished the substantial advancements shaping XPS into its current form during the 1950s and 1960s **[24-25]**. Siegbahn's dedication to refining XPS culminated in his receipt of the Nobel Prize in 1981, specifically for his notable work on high-resolution electron spectroscopy, initially termed electron spectroscopy for chemical analysis (ESCA).

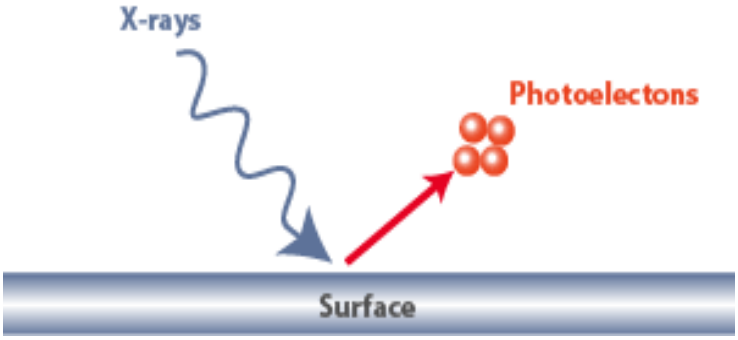

Figure II.7: Ejection of photoelectrons **[26]**.

II.2.4.2 Principle

The X-ray Photoelectron Spectroscopy (XPS) technique is grounded on the principle of photoionization. An examined sample's surface is stimulated by monoenergetic X-ray photons within the 150-1500 eV range, leading to the emission of photoelectrons that are subsequently segregated based on their energy levels. The substantial energy of the primary photons enables the extraction of electrons from the inner atomic electron shells, thereby ionizing the surface atoms **[27]**. While the photons have a penetration depth of 1-10 µm, the electrons, due to their significant inelastic scattering cross section resulting in a complex multiple scattering phenomenon, can only escape from the surface's topmost few atomic layers. X-ray photons possess the capability to excite electrons from the valence band (0-25 eV) and atomic core levels with binding energy ranging from 25-1500 eV. Consequently, XPS proves to be a valuable tool for analyzing the electron configuration of surfaces **[28]**. The excitation of X-ray photons instigates the emission of photoelectrons in accordance with a specific equation:

$$h\nu = E_i^F + E_k + \psi_{sp}$$

the energy of the exciting radiation, denoted as $h\nu$, along with the ionization energy of electrons referenced to the Fermi level, E_i^F , the kinetic energy of photoelectrons, E_k , and the work function of the spectrometer, ψ_{sp} , need to be considered. This is necessary because the sample and the detector of the spectrometer are in metallic contact with each other, leading to the equalization of Fermi levels and the generation of contact potential.

II.2.4.3 Apparatus used

X-ray photoelectron spectroscopy was performed with a VG Escalab 200 R spectrometer employing Al Kα (1486 eV) as X-ray source. (Research Center of Semi-conducteur Technology for Energy (CRTSE), Algiers).

Figure II.8 : XPS – Surface Analysis **[18].**

II.2.5 UV-Vis Spectroscopy

II.2.5.1 Introduction

UV-visible spectroscopy is a rapidly employed analytical method utilized for quantifying the light's absorbance or transmittance **[29]**,**[30]**. The UV spectrum encompasses wavelengths ranging between 100 and 380 nm, with the visible range extending up to 800 nm **[31]**; however, the majority of spectrophotometers operate within the wavelength span of 200 to 1100 nm. In the realm of UV-vis spectroscopy, the practical range typically spans from 200 to 800 nm, with wavelengths beyond 800 nm falling into the infrared category, while those below 200 nm are classified as vacuum UV. The capacity of substances to absorb and emit light plays a pivotal role in determining their visual appearance, with the human eye being capable of distinguishing among an extensive palette of up to 10 million distinct hues **[32]**. Light interacts with various mediums through processes such as transmission, reflection on both opaque and transparent surfaces, and refraction when encountering crystals. Compounds characterized by covalent unsaturation and possessing electronic transition energy variances that align with the energy levels of UV-visible light demonstrate absorption at particular wavelengths. Chromophores, which are compounds recognized for their distinctive coloration, are accountable for this characteristic. Auxochromes **[33]**, on the other hand, are covalently saturated groups that do not directly interact with UV-visible electromagnetic radiation but do impact the absorption properties of chromophores. Upon exposure to UV-visible radiation, chromophores undergo an electron excitation process where electrons transition from a ground state to an excited state. In contrast, auxochromes function as electron donors and possess the ability to influence the coloration of chromophores without undergoing any color changes themselves. Substances such as water and alcohols are typically transparent and do not exhibit absorption within the UV-visible spectrum, making them ideal mediums for UV-visible spectroscopic analysis **[34]**. However, acetone and dimethylformamide (DMF) serve as effective solvents for compounds that are insoluble in water and alcohol. It is worth noting that acetone absorbs light below 320

nm, while DMF absorbs light below 275 nm, thus limiting their suitability to wavelengths above these specific cut-off points.

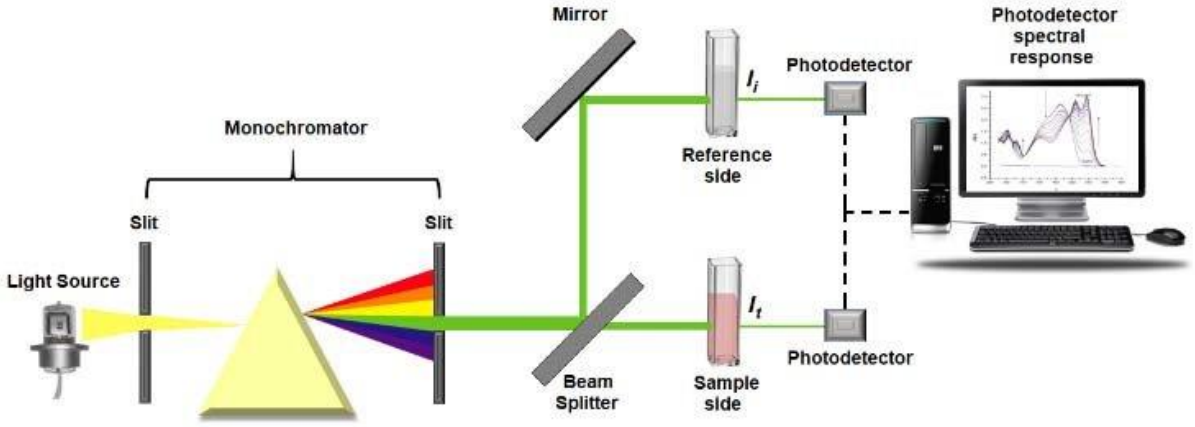

Figure II. 9: Schematic representation of the dual-beam UV-VIS spectrometer **[35]**.

II.2.5.2 Principle

UV-visible spectroscopy relies on the electronic transitions of organic molecules that absorb light, leading to the excitation of electrons from a lower energy orbital (highest occupied molecular orbital—HOMO) to a higher energy unoccupied orbital (lowest unoccupied molecular orbital—LUMO). The absorption of light of a specific energy must match the energy gap between the HOMO and LUMO orbitals (**Figure II.10**) **[36]**.

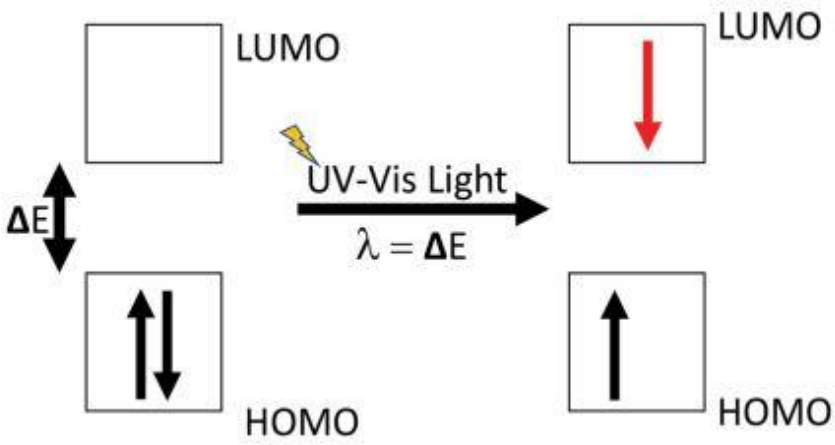

Figure II.10: The concept of molecular orbitals (closely linked to the energy difference required for the excitation of electron energy levels).

In conjugated systems, the energy gap between the lower and higher energy molecular orbitals is smaller compared to isolated double bonds, resulting in the absorption of longer wavelengths. Furthermore, in larger conjugated systems, the corresponding wavelength of light absorbed also increases **[37]**.

The path length through the sample (b), concentration (C), and molar absorptivity (ε) influences the absorbance of light, denoted as A, which is unique to each compound according to the Beer-Lambert law **[36]**.

$$A = \log_{10} \frac{I_0}{I} = \varepsilon . b . c$$

II.2.5.3 Apparatus used

The Cary 7000 is a double harder spectrophotometer to measure the absorbance of a liquid or solid sample as a function of the wavelength in the field of ultraviolet, visible and the close infrared (NIR), either from 175 to 3300 nm (Nanotechnology laboratory, Kütahya Dumlupiner Univerity).

In addition to a range of varied sampling holders, the instrument has two external accessories: the UMA (Universal Measurement Accessory) makes it possible to automatically measure the absolute reflectivity, transmission and distribution to a wide range of angles and different polarizations. This accessory is ideal for research in the fields of thin films and coverings, optics, glass and solar energy. The second accessory, the DRA (diffuse Reflectance Accessory), is an integration sphere which allows to concentrate the light diffused by a sample to the detector.

Figure II. 11: UV-visible spectroscopy-NIR.

II.1 PHOTOCATALYTIC EXPERIMENTS

$BiFeO_3/Bi_2O_3$ composite was subjected to evaluation for its photocatalytic efficacy in the degradation of Nitrobenzene (NB) utilizing various visible light sources. The assessments were conducted within a double-walled glass cylinder containing 250 mL of water, with continuous

cooling to sustain ambient conditions and prevent overheating upon light exposure. The experimental setup included 1 g/L of the composite powder, a pH close to neutral, and an initial Cobalt concentration of 0.4 mmol/L. Preceding the light exposure, the suspension (250 mL of catalyst/NB) underwent a 30-minute period of darkness to establish an adsorption equilibrium, followed by irradiation under both solar light (optimal absorption around 500 nm in the solar spectrum) and artificial light (15 W LED lamp with a color temperature of 6500K, maximum absorption at approximately 450 nm). At specified intervals, samples were centrifuged at 6500 rpm for 15 minutes to separate the powder from the NB solution, and the residual NB levels were quantified using a UV-visible spectrophotometer (Uviline 9400 SECOMAM) at a wavelength of 290 nm. The experimental investigations were carried out during October, spanning from 10:00 to 15:00.

II.2 CATALYTIC TESTS

In this section, we give an account of the different preparation methods used for preparation of catalysts, which have been prepared and investigated in this thesis.

II.4.1 Catalytic hydrogen generation :

In order to assess and enhance the catalytic efficacy of the synthesized $BiFeO_3$-Bi_2O_3, a $NaBH_4$ methanolysis process was conducted. This involved systematically altering the amount of catalyst, the temperature, and the substrate concentration for each trial, with the aim of identifying the optimal conditions that yield the greatest catalytic activity.

II.4.1.1 Catalyst amount effect

In this procedure, the amount of catalyst was established at 10, 20, 30, and 40 mg, maintaining consistency in all other variables, and assessing the velocity at which hydrogen is emitted (25 ◦C, 300 mM $NaBH_4$).

II.4.1.2 Subtrate effect

To test the performance of different $NaBH_4$ substrate concentrations on the hydrogen generation rate, measurements was performed by keeping the temperature and catalyst ratios constant. $NaBH_4$ concentrations were used as 125, 300, 350 and 400 mM, respectively. The hydrogen release rate of different concentrations of $NaBH_4$ under constant parameters (40 mg catalyst and 25 °C temperature).

II.4.1.3 Temperature effect

To observe the effect of different temperatures on the substrate, the assessment of hydrogen production rate at 25 °C, 30 °C, 35 °C, and 40 °C was conducted while maintaining all other variables constant (40 mg $BiFeO_3$-Bi_2O_3 and 300mM of $NaBH_4$), illustrates a notable enhancement in hydrogen production and release rate corresponding to the rise in temperature.

II.4.1.4 Reusability

Reusability efficiency testing was conducted employing a 40 mg catalyst. Following the execution of hydrogen generation with a 40 mg catalyst under consistent conditions (40 °C temperature and 400 mM substrate), the identical specimen underwent nine times, and a total of five measurements of hydrogen production.

References:

[1] Sopiha, Kostiantyn V., et al. "Chalcogenide perovskites: tantalizing prospects, challenging materials." Advanced Optical Materials 10.3 (2022): 2101704.

[2] İSKENDER, Halil. "The Interplay of Polysemy and Prototypes: A Prototype Theory Approach to the Turkish Polysemic–lIk Morpheme." Karamanoğlu Mehmetbey Üniversitesi Edebiyat Fakültesi Dergisi 6.Cumhuriyet'in 100. Yılı Özel Sayısı (100th Year of the Republic Special Issue) (2023): 56-76.

[3] Lerner, Adam B. From the ashes of history: collective trauma and the making of international politics. Oxford University Press, 2022.

[4] Ficarra, Bernard Joseph. International Diplomacy and United States National Policies. University Press of America, 2006.

[5] Deganello, Francesca, G. Marcì, and G. Deganello. "Citrate–nitrate auto-combustion synthesis of perovskite-type nanopowders: A systematic approach." Journal of the European Ceramic Society 29.3 (2009): 439-450.

[6] Gulati, Shikha, et al. "Bismuth ferrite (BiFeO 3) perovskite-based advanced nanomaterials with state-of-the-art photocatalytic performance in water clean-up." Environmental Science: Water Research & Technology 8.8 (2022): 1590-1618.

[7] Ilić, Nikola I., et al. "Structure and properties of chemically synthesized BiFeO3. Influence of fuel and complexing agent." Ceramics International 41.1 (2015): 69-77.

[8] Learning, Lumen. "Young's Double Slit Experiment." Fundamentals of Heat, Light & Sound (2021).

[9] Anana, Hayet, and Chaouki Boudaren. Composés à base de lanthanides. Diss. Université Frères Mentouri-Constantine 1, 2020.

[10] Gawas, Umesh B., Vinod K. Mandrekar, and Mahesh S. Majik. "Structural analysis of proteins using X-ray diffraction technique." Advances in biological science research. Academic Press, 2019. 69-84.

[11] Kohal, Ralf-Joachim, et al. "Long-term stability of hydrothermally aged and/or dynamically loaded one-piece diameter reduced zirconia oral implants." Journal of Functional Biomaterials 14.3 (2023): 123.

[12] Ghada Hassanine and Amina Hassani, "Synthèse, caractérisation et propriétés Photo-catalytique d'un composite à base de Fer et Bismuth $BiFeO_3$-Bi_2O_3," Faculté des Sciences Exactes et des Sciences de la Nature et de la Vie, Université Mohamed Khider, 2019.

[13] Plank, Harald, et al. "Focused electron beam-based 3D nanoprinting for scanning probe microscopy: a review." Micromachines 11.1 (2019): 48.

[14] Chirayil, Cintil Jose, et al. "Instrumental techniques for the characterization of nanoparticles." Thermal and rheological measurement techniques for nanomaterials characterization. Elsevier, 2017. 1-36.

[15] Sieradzka, Marta, et al. "Insight into the effect of graphite grain sizes on the morphology, structure and electrical properties of reduced graphene oxide." Journal of Materials Research and Technology 9.4 (2020): 7059-7067.

[16] Maćczak, Piotr, Halina Kaczmarek, and Marta Ziegler-Borowska. "Recent achievements in polymer bio-based flocculants for water treatment." Materials 13.18 (2020): 3951.

[17] Chaudhary, Raghvendra Pratap, et al. "Additive manufacturing of polymer-derived ceramics: Materials, technologies, properties and potential applications." Progress in Materials Science 128 (2022): 100969.

[18] https://crtse.dz/caracterisations-disponibles/ Accessed: May11,2025.[Online].Available:

[19] Dong, Jun. "Development of Fourier transform infrared (FTIR) spectroscopy for determining oil quality." (1996).

[20] Stuart, Barbara. "Infrared spectroscopy." Analytical techniques in forensic science (2021): 145-160.

[21] Ojeda, Jesús J., and Maria Dittrich. "Fourier transform infrared spectroscopy for molecular analysis of microbial cells." Microbial Systems Biology: Methods and Protocols (2012): 187-211.

[22] Djani, Faiçal. Etude physicochimique du système LaMM'O3 à base de métaux divalents et trivalents. Diss. Université Mohamed Khider-Biskra, 2016.

[23] Steinhardt, Ralph, and Earl Serfass. "X-ray photoelectron spectrometer for chemical analysis." Analytical Chemistry 23.11 (1951): 1585-1590.

[24] Nordling, Carl, Evelyn Sokolowski, and Kai Siegbahn. "Precision method for obtaining absolute values of atomic binding energies." Physical Review 105.5 (1957): 1676**.**

[25] Siegbahn, Kai. "ten co-workers.(1967)." Nova Acta Regiae Societatis Scientiarum Upsaliensis, ser. IV, 20, 1-282.(Presentation to Royal Society of Sciences of (1965).

[26] Krishna, D. Nanda Gopala, and John Philip. "Review on surface-characterization applications of X-ray photoelectron spectroscopy (XPS): Recent developments and challenges." Applied Surface Science Advances 12 (2022): 100332.

[27] Berry, R. Stephen, and Boris M. Smirnov. "Configurational transitions in processes involving metal clusters." Physics Reports 527.4 (2013): 205-250.

[28] Fewster, Paul F. X-Ray scattering from semiconductors and other materials. World Scientific, 2015.

[29] Watts, John F., and John Wolstenholme. An introduction to surface analysis by XPS and AES. John Wiley & Sons, 2019.

[30] Barbosa-García, O., et al. "UV–vis absorption spectroscopy and multivariate analysis as a method to discriminate tequila." Spectrochimica Acta Part A: Molecular and Biomolecular Spectroscopy 66.1 (2007): 129-134.

[31] Asahi, R. Y. O. J. I., et al. "Visible-light photocatalysis in nitrogen-doped titanium oxides." science 293.5528 (2001): 269-271.

[32] Owen, A. E. "Fundamentals of UV-visible spectroscopy." (1996).

[33] Patience, Gregory S. Experimental methods and instrumentation for chemical engineers. Elsevier, 2017.

[34] Gürses, Ahmet, et al. "Dyes and pigments: their structure and properties." Dyes and pigments (2016): 13-29.

[35] Braga, Mauro Sergio, et al. "Multispectral colorimetric portable system for detecting metal ions in liquid media." 2019 4th International Symposium on Instrumentation Systems, Circuits and Transducers (INSCIT). IEEE, 2019.

[36] Sauer, Markus, Johan Hofkens, and Jörg Enderlein. "Basic principles of fluorescence spectroscopy." Handbook of Fluorescence Spectroscopy and Imaging 1 (2011): 30.

[37] Dyer, P. W., et al. "Functional Organic Materials: Syntheses, Strategies and Applications." (2007): 119-177.

CHAPTER III:

AUTOCOMBUSTION SYNTHESIS OF $BiFeO_3$/Bi_2O_3, AND ITS PROPERTIES

CHAPTER III : AUTOCOMBUSTION SYNTHESIS OF $BiFeO_3/Bi_2O_3$, AND ITS PROPERTIES

III.1. Introduction:

An autocombustion method has been used to prepare $BiFeO_3/Bi_2O_3$ composite, this composite has been generated by integrating an excess of the Bismuth nitrate precursor (0, 5, 10, 15 and 20). In order to investigate and to compare the composite properties, bare oxides were also prepared using the same route.

This chapter is dedicated to the study of the various properties of the targeted produced composite. For this purpose, the obtained powders undergone -without calcination- multiple characterization techniques including: XRD, XPS, SEM/EDS FTIR and UV-Vis.

III.2. Autocombustion synthesis of the samples:

III.2.1. Preparation of $BiFeO_3$:

The mixed oxide has been prepared using bismuth nitrates ($Bi(NO_3)_3.5H_2O$) (99%); Iron nitrates ($Fe(NO_3)_3.9H_2O$) (99%) from Chemopharma dissolved in distilled water. The metal nitrates have been dissolved in distilled water then mixed in a beaker. Simultaneously, glycine ($C_2H_5NO_2$) (98.5%, Chemopharma) was dissolved in deionised water, then added to the metals nitrates solution. The mixture was heated under 80°C with stirring, for a slow evaporation of the solvent, when only a minimal amount of solvent remains, a sudden increase in temperature is applied until the combustion occurs. Subsequently, the resulting powder is collected and ground, without following up with a calcination step. The synthesis reaction is as follows:

$$Bi(NO_3)_3,5H_2O + Fe(NO_3)_3,9H_2O + \propto C_2H_5NO_2 \Rightarrow BiFeO_3 + 2\propto CO_2 + (3+\propto)N_2 + [14+ (5\propto)/2\ H_2O] \quad (1)$$

Where: $\propto = 10/3$ (2)

The next picture explains the various steps during the $BiFeO_3$ autocobustion synthesis:

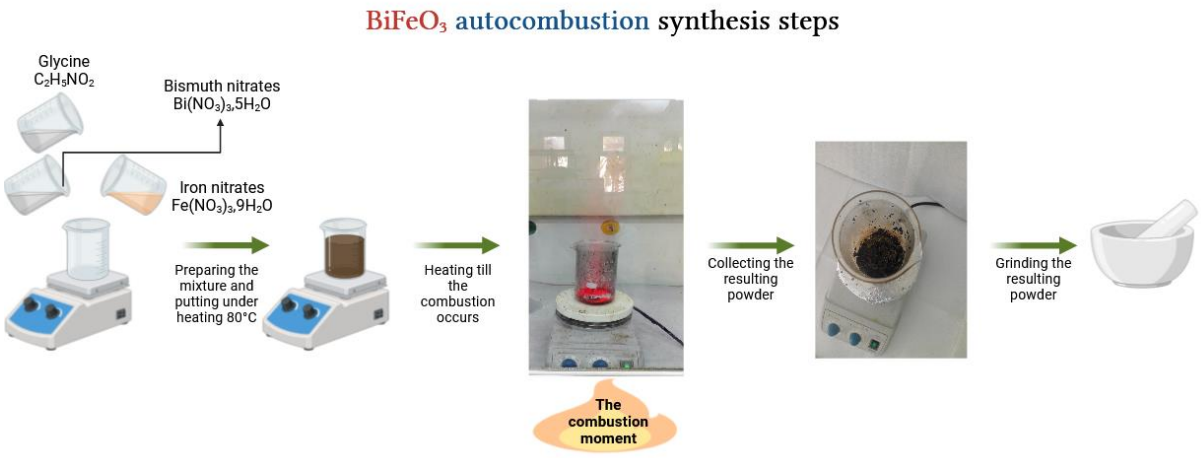

Figure III.1: Different steps of $BiFeO_3$ autocobustion synthesis

III.2.2. Preparation of Bi_2O_3:

The Bi_2O_3 simple oxide was synthesized similarly to the previous mixed oxide (as it appears in figure III.2). This involved dissolving bismuth nitrates ($Bi(NO_3)_3.5H_2O$) (99%) and glycine ($C_2H_5NO_2$) (98.5%) -from Chemopharma- in distilled water, then applying along heat at 80°C, followed by a swift heating elevation until combustion took place. The resulting yellow powder tinged with dark gray was collected then grinded without calcination also. The precedent reaction describes this synthesis:

$$Bi(NO_3)_3,5H_2O + \gamma C_2H_5NO_2 \Rightarrow Bi_2O_3 + 2\gamma\ CO_2 + (3/2+\gamma)\ N_2 + [10+(5\propto)/2\ H_2O] \quad (3)$$

Where: $\gamma=2/6$ (4)

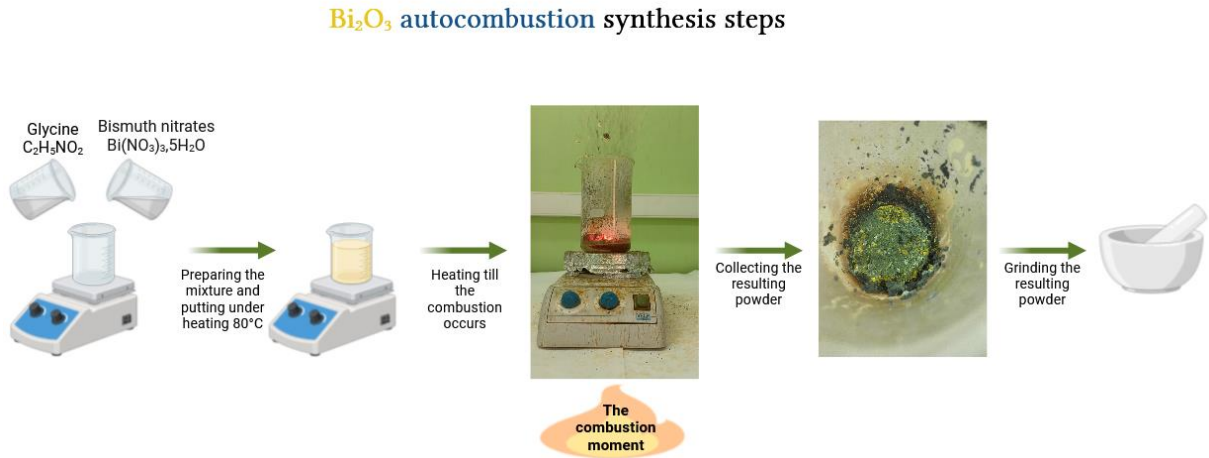

Figure III.2: The synthesis of Bi_2O_3 by autocobustion.

III.2.3. Preparation of $BiFeO_3/Bi_2O_3$:

To produce the composite an excess of (5, 10, 15 and 20%) of bismuth nitrates has been introduced into the normal synthesis of $BiFeO_3$, following the same manner as the next piture shows:

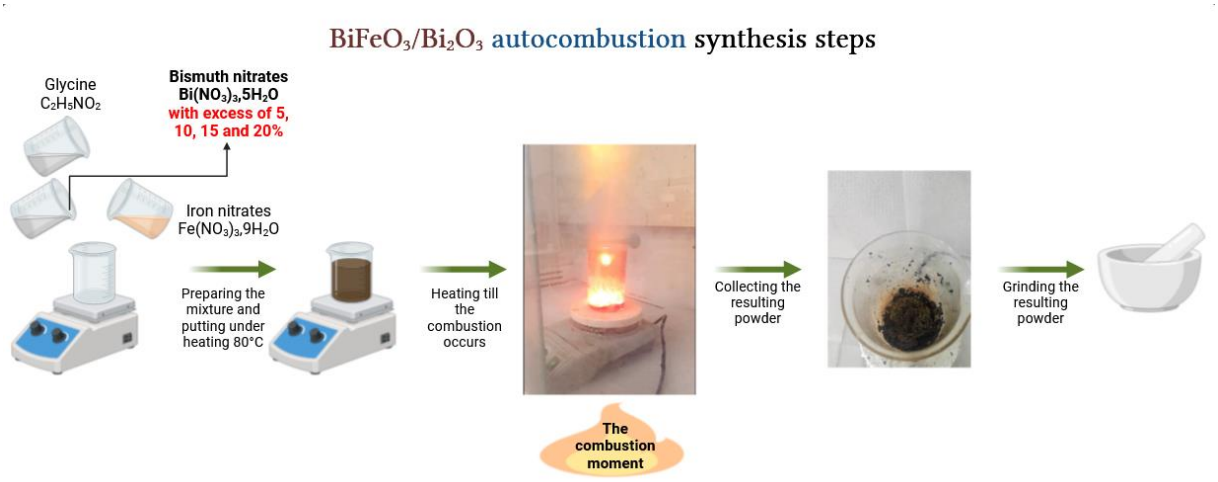

Figure III.3: The autocobustion synthesis of the multiple composite formulations.

III.3. Characterization of oxides:

III.3.1. X-ray diffraction analysis:

In order to investigate the structural properties of compounds, the six fabricated samples have been analyzed using Bruker D8 advance diffractometer (with Cu Kα radiation, λ= 0.15418 nm). The measurements were conducted over 2θ angles from 10° to 100°. The recorded diffractometers were treated using X'pert Highscore software package for phase identification -with the assistance of ICSD cards- and for Rietveld refinement.

III.3.1.1. XRD of the synthesized BiFeO3:

XRD result shows that the as-prepared bismuth iron oxide $BiFeO_3$ crystallizes with a hexagonal system under the space group R 3 m, n°: 160. It was identified comparing with 98-002-8027 ICSD data file (Figure III.4) We note the existence of $Bi_2Fe_4O_9$ as a parasitic phase. Refined crystal parameters are summarized in Table III.1.

Table.III.1: Cell parameters of as-prepared $BiFeO_3$ single phase.

Oxide	Lattice parameters						Cell Volume ($Å^3$)
	a (Å)	b (Å)	c (Å)	α (°)	β (°)	γ (°)	
$BiFeO_3$	5.578311	5.578311	6.93619	90	90	120	186.9206

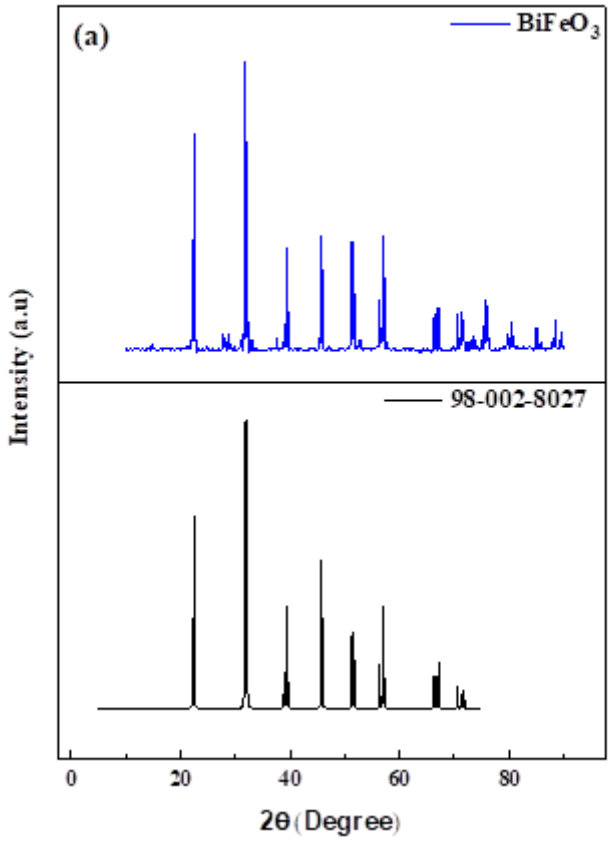

Figure III.4: XRD pattern of the synthesized BiFeO3 compared to ICSD file.

III.3.1.2. XRD of the synthesized Bi_2O_3:

Synthesized bismuth oxide diffractogram reveals an α-Bi_2O_3 phase (Figure III.5). It has a monoclinic system and P 1 21/c 1 space group, n°: 14. Referring to ICSD data file n°: 98-009-4231 we attributed the phase. At low temperatures, this phase is thermodynamically stable [1], [2] which can explain its formation, with no calcination and in the absence of steadily thermal treatment at high temperatures relatively. Refined lattice parameters and cell volume are placed in Table III.2.

Table III.2: Lattice parameters and Cell volume of synthesized α-Bi_2O_3 single phase.

Oxide	Lattice parameters						Cell Volume (Å^3)
	a (Å)	b (Å)	c (Å)	α (°)	β (°)	γ (°)	
Bi_2O_3	5.83663	8.166412	7.488716	90	112.9804	90	328.6169

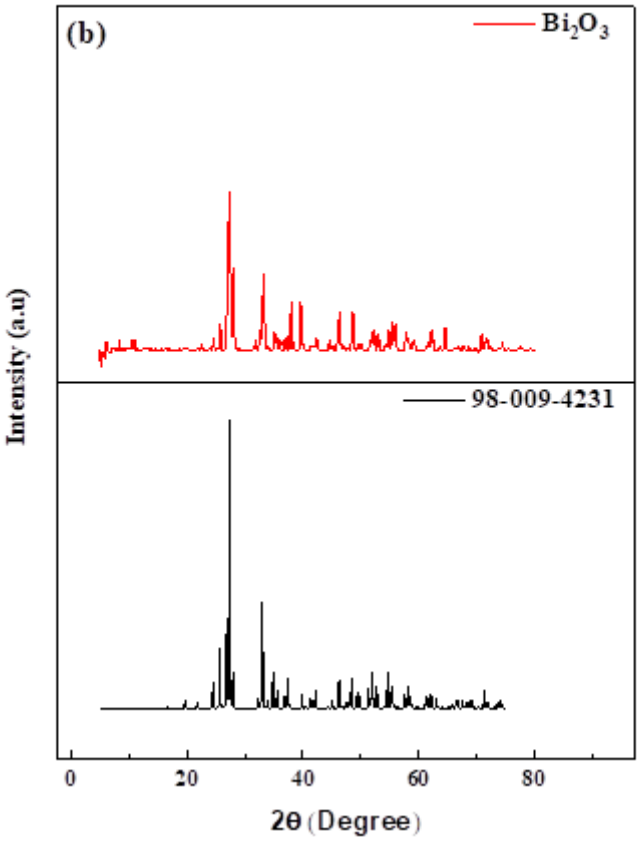

Figure III.5: Bi_2O_3 diffractogram with the attributed ICSD data file.

III.3.1.3. XRD of the synthesized composites with the excess of Bismuth:

The prepared sample diffractogram with an excess of a 5% of bismuth nitrates at the synthesis revealed its composition of $BiFeO_3/Bi_2O_3$ system BB5 namely, while diffractograms of the other formulations (10, 15 and 20%) shows that those composites contain mainly Bi_2O_3 and Fe_3O_4 with other minority phases such as $BiFeO_3$ (Figure III.6).

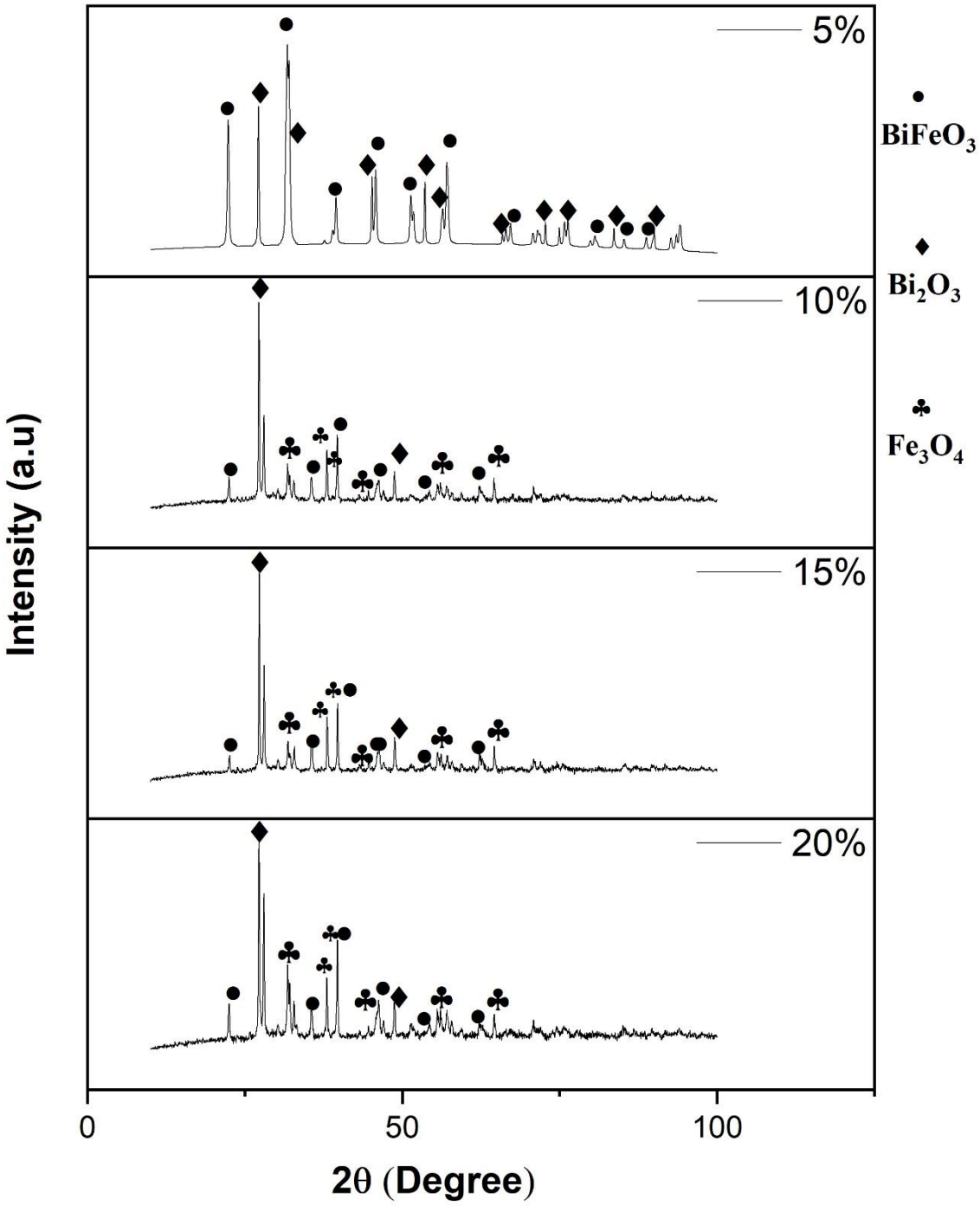

Figure III.6: XRD results pf the prepared composites.

The BB5 composite is composed majorly from 82.7% of $BiFeO_3$ and a 17.3% of Bi_2O_3. The $BiFeO_3$ was identified comparing with the ICSD card code: (98-024-6424), it crystalizes with rhombohedral geometry with hexagonal system, with the space group: R 3 c, n°:161. Bismuth oxides has been detected by the comparison with the ICSD card n°: (98-002-7458),

this phase has a cubic crystal system and space group: F m -3 m n°: 225. Cell crystal parameters are summarized in Table III.3.

Table III.3: BB5 binary composite crystal parameters.

Oxide	Lattice parameters						Cell Volume ($Å^3$)
	a (Å)	b (Å)	c (Å)	α (°)	β (°)	γ (°)	
$BiFeO_3$	5.55548	5.55548	13.81201	90	90	120	369.1736
Bi_2O_3	5.651603	5.651603	5.651603	90	90	90	180.5157

III.3.2. XPS measurments of bare oxides and BB5 composite:

Surface chemical characterization of the samples was performed using X-ray photoelectron spectroscopy (XPS) on a Thermo Fisher Scientific NEXSA photoelectron spectrometer. The instrument utilized a monochromatic Al Kα X-ray source with a photon energy of 1486.6 eV.

III.3.2.1. XPS of bare oxides:

By using XPS characterization, the metal oxidation state of the Bi_2O_3 and $BiFeO_3$ was studied individually. The servey XPS spectra of both the tow phase is shown on Figure III.7.(a). No other peaks are visible save O, Bi, and C for the tow system and Fe for $BiFeO_3$, which signify the pure phases of the perovskites. Two peaks at 710.7 and 724.4 eV, which correspond to the binding energies of Fe $2p^{3/2}$ and Fe $2p^{1/2}$, respectively, can be seen in the XPS spectra of the Fe 2p for $BiFeO_3$ in Figure III.7(b). This implied the existence of Fe^{3+} [3]. Two peaks in Figure III.7.(c,d) are attributed to Bi $4f^{7/2}$ and Bi $4f^{5/2}$, respectively, for Bi_2O_3 and $BiFeO_3$, demonstrating that the bismuth species in these samples are Bi^{3+} [4], [5]. The Bi_2O_3 O1s spectra shown in Figure III.7.(e) may be fitted to two peaks, the lower of which has a binding energy of 530.4 eV attributed to the Bi-O and the higher of which has a binding energy of 532.5 eV attributed to the chemisorbed oxygen [6], [7]. According to Figure III.7.(f), the electron binding energies of O 1s for $BiFeO_3$ are respectively 529.12, 530.85, and 531.87 eV for Fe-O, Bi-O, and the surface-adsorbed oxygen [7], [8].

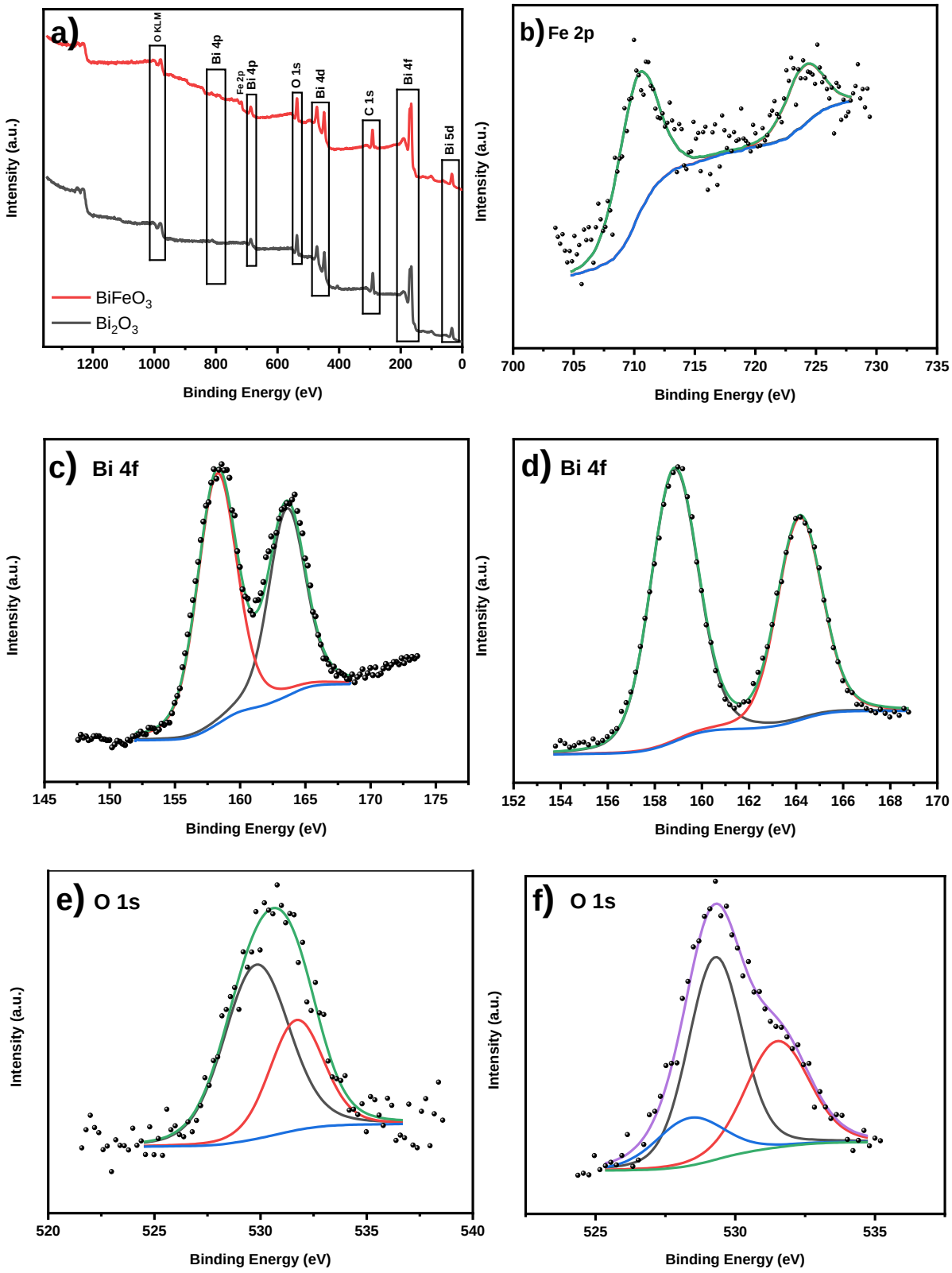

Figure III.7: (**a**) The XPS survey spectrum of both Bi_2O_3 and $BiFeO_3$, (**b**) Fe 2p high-resolution XPS spectrum of $BiFeO_3$, (**c,d**) Bi 4f high-resolution XPS spectrum of Bi_2O_3 and $BiFeO_3$ respectively (**e,f**) O 1s high-resolution XPS spectrum of Bi_2O_3 and $BiFeO_3$ respectively.

III.3.2.2. XPS the synthesized BB5 composite:

The oxidation states of elements within the BB5 compound are shown in Figure III.8. The survey scan (Figure 1a) identified Bi, Fe, O, and C as the primary constituents. Deconvolution of the high-resolution Bi spectrum (Figure 1b) revealed four peaks, two prominent ones at 157.8 eV and 163.2 eV corresponding to Bi 4f7/2 and 4f5/2 of Bi^{3+}, respectively [9]. The spin-orbit splitting of 5.4 eV aligns with the Bi-O bond [10], confirming the +3 oxidation state for Bi. Two minor peaks at higher binding energies are attributed to surface charging effects arising from the polarization change in the Bi_2O_3 phase [11], [12], [13]. The Fe 2p spectrum (Figure 1c) exhibits characteristics of Fe^{3+} with deconvoluted peaks at 710.6 eV ($2p_{3/2}$) and 723 eV ($2p_{1/2}$) [14]. An additional peak at 718.5 eV further supports the Fe^{3+} oxidation state in BiFeO3 [15]. The O 1s spectrum (Figure 1d) displays a single peak deconvoluted into two Gaussian components at 529.2 eV and 531.4 eV. The lower binding energy component corresponds to lattice oxygen, while the higher one suggests the presence of oxygen vacancies within the sample [16].

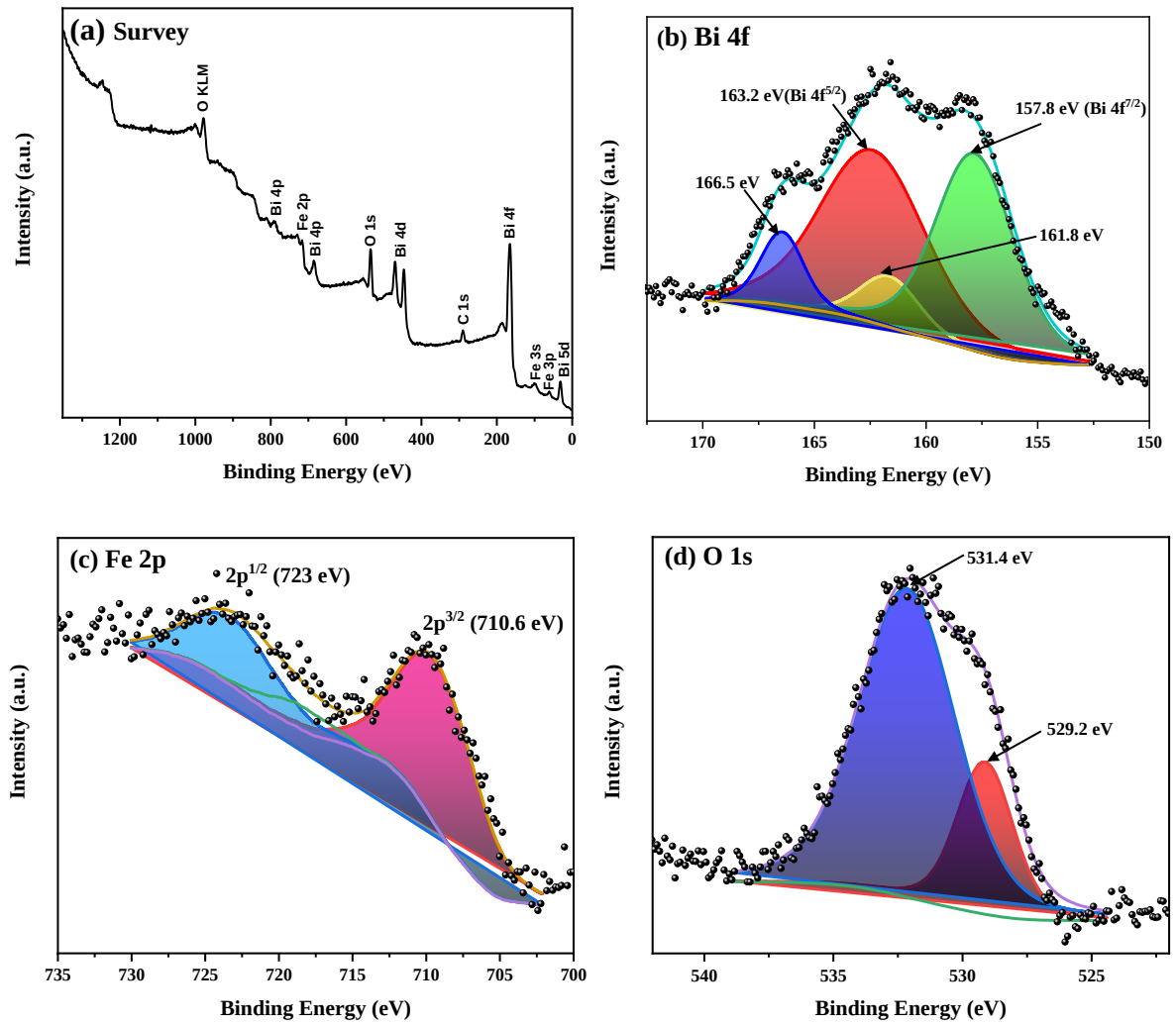

Figure III.8: (a) The electrode's survey XPS spectrum of the BB5 heterotructure, (b) Bi 4f high-resolution XPS spectrum, (c) Fe 2p high-resolution XPS spectrum and (d) O 1s high-resolution XPS spectrum.

III.3.3. SEM-EDS analysis of oxides:

The morphology and elemental composition of the samples were initially investigated using a scanning electron microscope (SEM). The specific model employed was a JEOL JSM-7610F Plus SEM operated at an acceleration voltage of 7 kV.

III.3.3.1. SEM-EDS of $BiFeO_3$:

Figure III.9 shows the morphological surface of $BiFeO_3$ where it appears to have a well-ordered agglomerated particles with sharp, well-defined edges and corners, predominantly cubes.

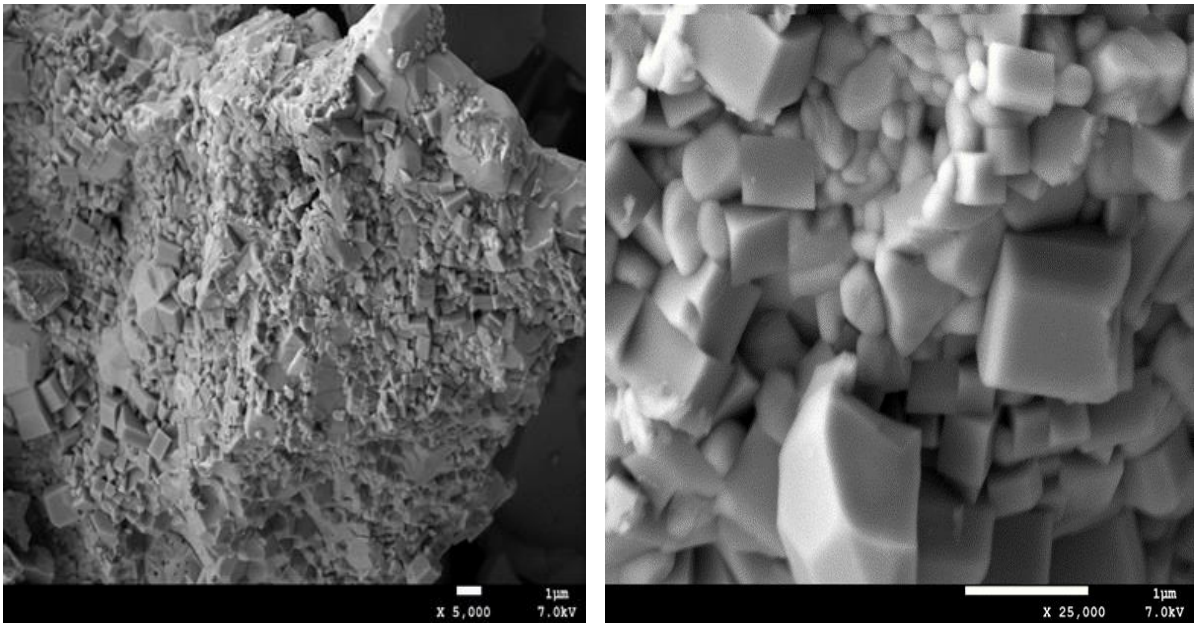

Figure III.9: SEM image of the prepared bismuth iron oxide.

EDS analysis in Figure III.10 indicates that of $BiFeO_3$ surface is primarily composed of Bismuth (Bi) at 18.82%, Iron (Fe) at 19%, and Oxygen (O) at 62.18%.

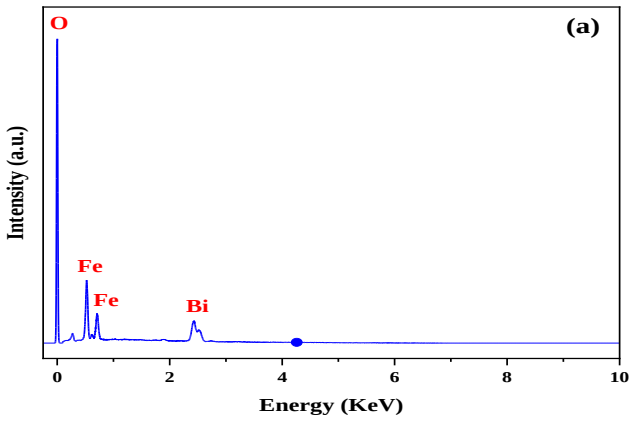

Figure III.10: EDS analysis spectrum of $BiFeO_3$.

III.3.3.2. SEM-EDS of Bi_2O_3:

The examination of the Bi_2O_3's morphology using scannig microscopy technique (as shown in Figure III.11) reveals that the particles are predominantly spherical and exist on the nanoscale. The size of these spherical grains ranges from 100 to 400 nanometers, and the material exhibits variations in both pore volume and average pore diameter.

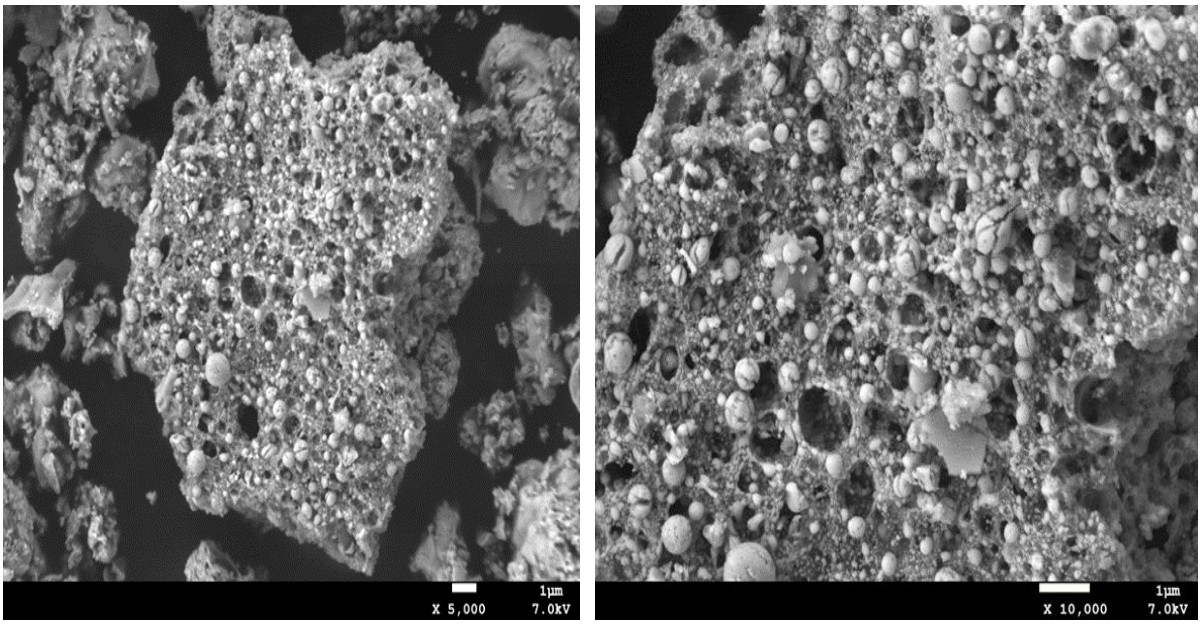

Figure III.11: SEM images of the produced Bi_2O_3.

Energy-dispersive X-ray spectroscopy (EDS) analysis, as presented in Figure III.12, confirms the elemental composition of the Bi_2O_3 sample. The data reveals the presence of Bi and O atoms, with quantitative results indicating 39.53% Bi and 60.47% O. This elemental composition aligns closely with the stoichiometric ratio expected for Bi_2O_3 (Bi:O = 2:3).

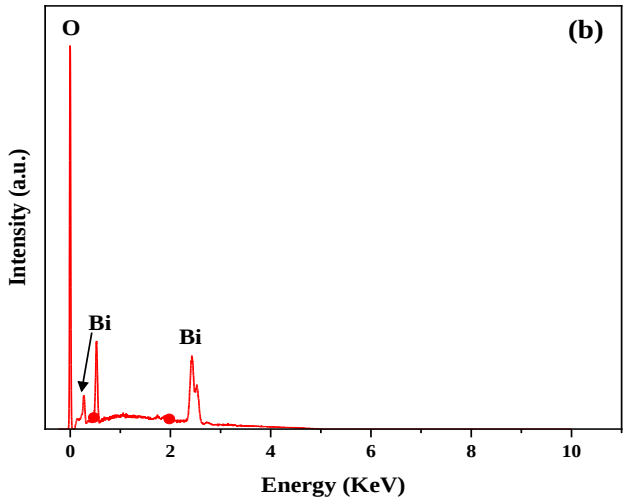

Figure III.12: The Bi_2O_3's EDS analysis result.

III.3.3.3. SEM-EDS of BB5 composite:

Figure III.13 presents scanning electron microscopy (SEM) images of the $BiFeO_3/Bi_2O_3$ composite, revealing the morphology of the constituent phases. The micrographs depict randomly distributed, spherical Bi_2O_3 particles deposited on the surface of the BiFeO3 matrix with a porous surface texture. This observation suggests a heterogeneous nanostructure within the composite.

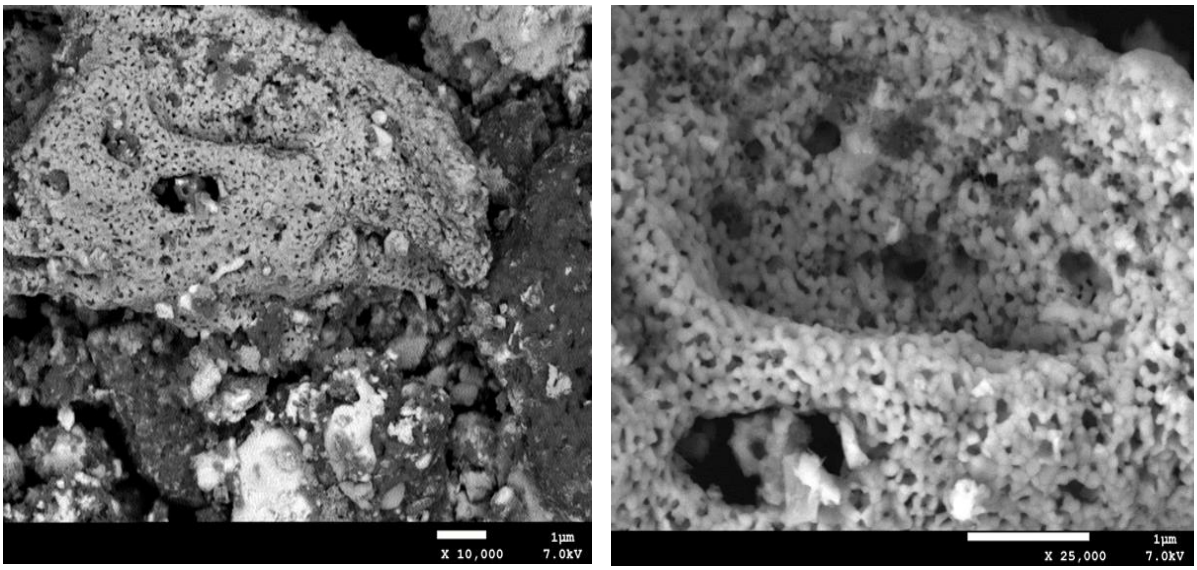

Figure III.13: SEM analysis of $BiFeO_3/Bi_2O_3$ composite morphology.

EDS analysis, presented in Figure III.14, provides a quantitative assessment of the elemental composition within the BiFeO3/Bi2O3 composite. The data confirms the presence of all expected elements: Bi (36.6%), Fe (13.6%), and O (49.8%). This composition aligns well with the combined stoichiometry of $BiFeO_3$ and Bi_2O_3, indicating the successful incorporation of both phases within the composite. Notably, the detection of Fe alongside Bi and O confirms the presence of the $BiFeO_3$ phase, complementing the information obtained for Bi_2O_3.

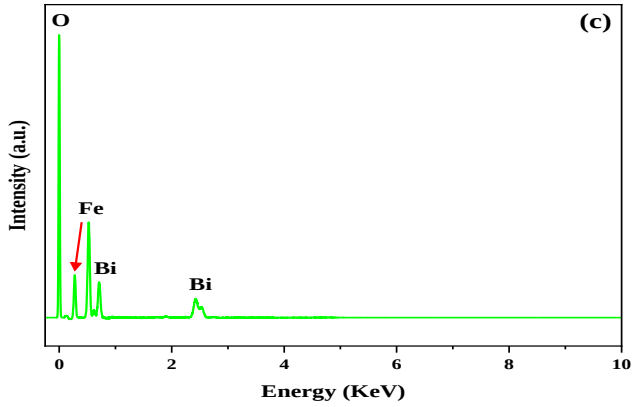

Figure III.14: EDS elemental composition of $BiFeO_3/Bi_2O_3$ Composite.

III.3.4. Fourier Transform Infra-Red spectroscopy analysis:

Functional group analysis of the prepared oxides was performed using Fourier Transform Infrared (FTIR) spectroscopy on a Shimadzu spectrometer (FTIR-8900). The analysis employed a wavenumber range of 400-4000 cm^{-1} to identify the functional groups present in the samples.

Figure III.14 presents the Fourier Transform Infrared (FTIR) spectra of $BiFeO_3$, Bi_2O_3, and the BiFeO3/Bi2O3 composite. The analysis, performed in the wavenumber range of 400-4000 cm^{-1}, allows for the identification of functional groups present within these materials. where characteristic vibrations of various functional groups are typically observed.

Metal-Oxygen Bonds:

Bi-O vibrations: The spectra exhibit a peak around 490 cm^{-1}, attributed to the stretching vibrations of the Bi-O bond within the BO_6 octahedral units of Bi_2O_3 [17]. An additional band near 715 cm^{-1} is assigned to both Bi-O bond vibrations in tetrahedral units of Bi_2O_3 and deformation vibrations between these units (BO_3-O-BO_3) [17].

Fe-O vibrations: In the $BiFeO_3$ and $BiFeO_3$-Bi_2O_3 composite spectra, a peak at approximately 550 cm^{-1} corresponds to the vibrational modes of Fe-O bonds within the FeO_6 octahedra [18].

Water Adsorbate:

A broad band observed around 3100-3400 cm^{-1} is indicative of the O-H stretching vibration in water molecules adsorbed on the material's surface. This is further supported by the presence of a deformation band around 1600 cm^{-1}, assigned to the O-H bending vibration in water [19].

Other Functional Groups:

The peak at approximately 1390 cm^{-1} can be attributed to the asymmetric stretching mode of the NO_3^- ion [19].

Two bands observed around 1120 and 1150 cm^{-1} are likely associated with the C-O stretching vibrations arising from glycine residues.

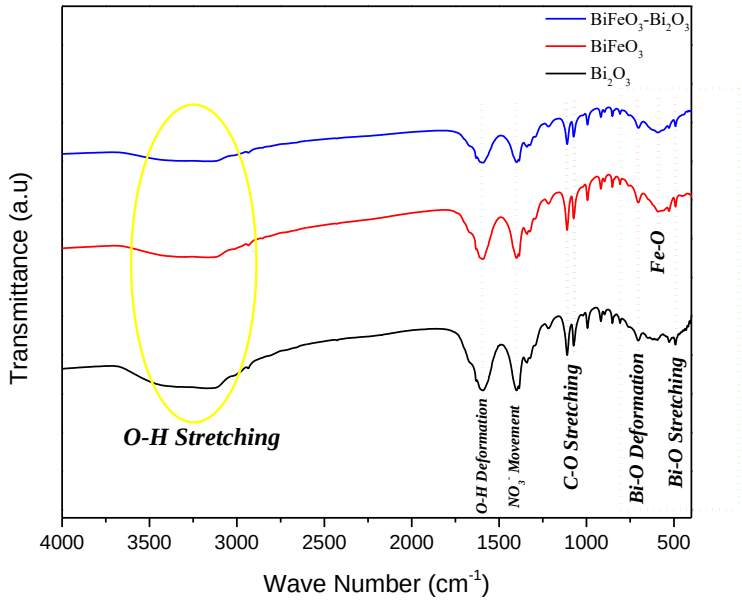

Figure III.15: Comparison of Bi_2O_3, $BiFeO_3$, and $BiFeO_3/Bi_2O_3$ composite using FTIR spectroscopy.

III.3.5. UV-Visible measurements:

To investigate the light absorption properties and to determine the optical band gap energies of Bi_2O_3, $BiFeO_3$, and $BiFeO_3/Bi_2O_3$ powders, UV-vis absorbance spectroscopy was employed. The analysis was performed using a Lambda 750 PerkinElmer UV-Vis spectrophotometer across a wavelength range of 200-1000 nm to acquire the absorbance data and evaluate the optical characteristics of the materials. To achieve absorbance measurements, each compound powder was sonicated in an amount of distilled water for 60 minutes at ambient temperature, with a sonication frequency of 55 kHz (using KUDOS Ultrasonicator). This permits effective dispersion of the powder particles throughout the solution.

The optical band gap (Eg) of the synthesized materials was determined by analyzing their light absorption behavior using Tauc's method. This approach involves plotting a specific function of the absorption coefficient (α) versus photon energy (hυ). The band gap energy corresponds to the point where the extrapolated linear portion of the curve intersects the x-axis (hυ = 0). The mathematical expression for Tauc's plot is provided below [20]:

$$(\alpha h\upsilon)^n = A \times (h\upsilon - E_g) \qquad \text{(III.1)}$$

the absorption coefficient (α) represents the material's ability to absorb light at a specific wavelength. In the context of semiconductors, the relationship between α and hυ depends on the type of electronic transition involved. For direct transitions, where the electron directly jumps from the valence band to the conduction band, the exponent n in Tauc's equation typically equals 1/2. Conversely, for indirect transitions involving a phonon (lattice vibration) assisting the electron jump, the value of n becomes 2. A is a constant factor that incorporates various

material properties and assumptions made in the derivation of the equation. This constant typically cannot be directly determined from the absorption data alone. However, by plotting $(\alpha h\upsilon)^n$ versus $h\upsilon$ for different values of n, the plot that exhibits a linear portion in the appropriate energy range allows for the extrapolation of the linear region to the x-axis ($h\upsilon = 0$). The intercept point on the x-axis provides the estimated value of the band gap energy (Eg) [21], [22], [23], [24].

III.3.5.1. Optical band gap of $BiFeO_3$:

The $BiFeO_3$ sample exhibited an optical band gap of approximately 2.95 eV, as evident from the Tauc's plot presented in Figure III.15:

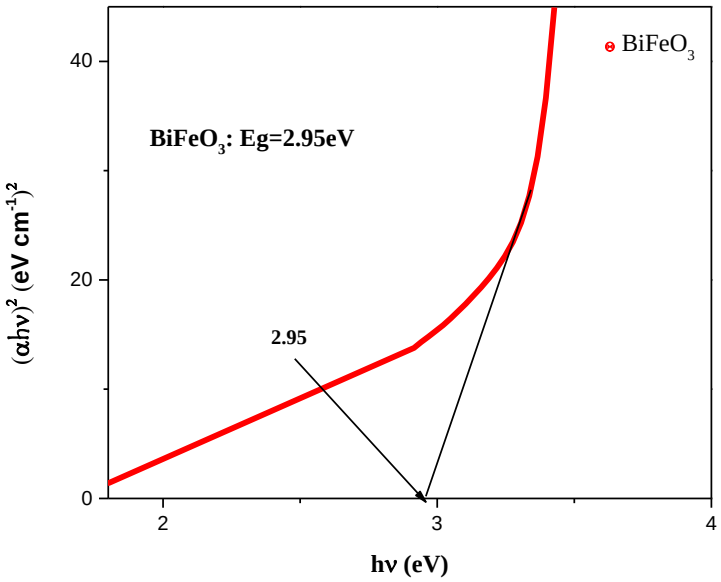

Figure III.16: Tauc's Plot of $BiFeO_3$.

III.3.5.2. Optical band gap of Bi_2O_3:

Figure III.16 illustrates the Tauc's plot for Bi_2O_3, indicating an optical band gap of 2.89 eV.

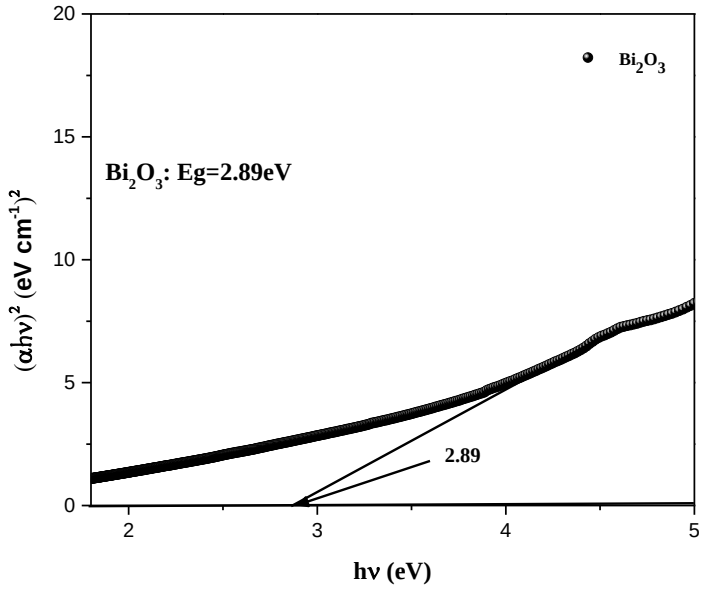

Figure III.17: Band gap estimation of Bi_2O_3.

III.3.5.3. Optical band gap of $BiFeO_3/Bi_2O_3$:

As shown in Figure III.18, the $BiFeO_3/Bi_2O_3$ band equals to 2.27 eV.

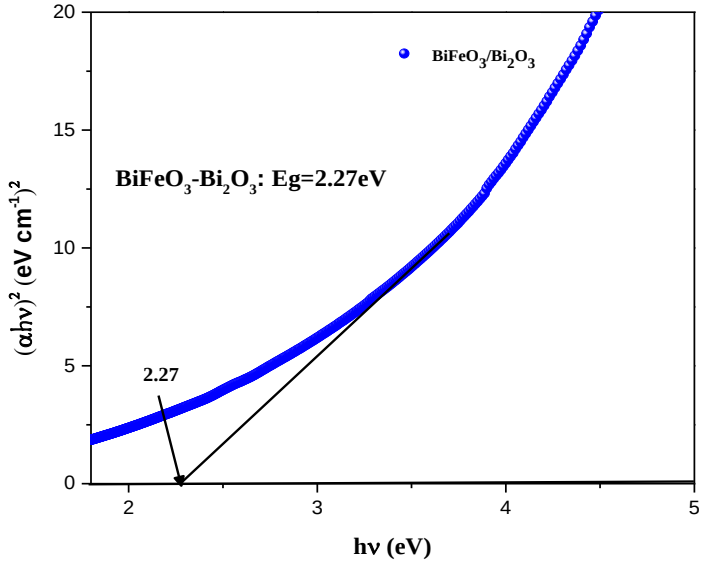

Figure III.18: Determination of $BiFeO_3/Bi_2O_3$ the optical band gap using Tauc's method.

III.3.5.4. Comparison between optical band gap of the three compounds:

The observed trend in the optical band gap energies (Eg) of Bi_2O_3 (2.89 eV), $BiFeO_3$ (2.95 eV), and the Bi_2O_3/Bi_2O_3 composite (2.27 eV) (Table III.4) can be attributed to several factors:

- Synergistic Effect and Defect Formation: When Bi_2O_3 and $BiFeO_3$ are combined in the composite, their interfacial contact can lead to the formation of new electronic states at the interface [25]. These interfacial states can act as intermediate energy levels, facilitating the transition of electrons from the valence band to the conduction band. This can result in a narrowing of the band gap compared to the individual components [26].
- Cation Intermixing and Strain: During the synthesis of the composite, there might be some intermixing of Bi^{3+} and Fe^{3+} cations at the atomic level. This intermixing can introduce lattice strain and modify the electronic band structure of the composite. The strain can cause bond length variations, influencing the energy levels and potentially leading to a band gap reduction [27].
- Quantum Confinement Effect: If the Bi_2O_3 phase in the composite exists as isolated nanoparticles or quantum dots within the $BiFeO_3$ matrix, quantum confinement effects might come into play. In smaller particles, the allowed energy levels for electrons become more discrete, leading to a potential increase in the band gap. However, in this case, the opposite trend is observed, suggesting the dominance of other factors like interfacial interaction or defect formation [28].
- Oxygen Vacancies: The presence of oxygen vacancies in the composite can introduce additional electronic states within the band gap. These vacancies can act as electron traps, potentially facilitating transitions and lowering the overall band gap energy compared to the individual components [29].

Table III.4: Optical band gap of the synthesized oxides.

Oxide	Optical band gap (eV)
$BiFeO_3$	2.95
Bi_2O_3	2.89
$BiFeO_3/Bi_2O_3$	2.27

III.4. Conclusion:

This chapter focused on the successful synthesis and characterization of $BiFeO_3$, Bi_2O_3, and $BiFeO_3/Bi_2O_3$ composites with varying Bi excess (0-20%) using bismuth nitrate as a precursor. The 5% excess Bi sample was identified as the composite material due to its unique characteristics.

A comprehensive characterization approach using XRD, XPS, FTIR, SEM-EDS, and UV-vis spectroscopy provided valuable insights into the structural, morphological, and optical properties of the synthesized materials. Notably, the $BiFeO_3/Bi_2O_3$ composite exhibited a lower band gap energy compared to the pure $BiFeO_3$ and Bi_2O_3. This decrease suggests the potential for enhanced photocatalytic activity under visible light irradiation. Additionally, the composite displayed a more porous morphology, which could offer increased surface area and improved mass transfer during catalytic processes.

These findings lay the foundation for further exploration of the $BiFeO_3/Bi_2O_3$ composite's potential applications in photocatalysis and other areas. The next chapter will investigate its performance in these applications, building upon the characterization results obtained in this chapter.

Références

[1] M. Alhaddad and A. A. Ismail, "Bi2O3-sensitized hierarchically mesoporous ZnO nanoparticles for Hg(II) reduction," *Ceram Int*, vol. 47, no. 12, pp. 17069–17076, Jun. 2021, doi: 10.1016/j.ceramint.2021.03.015.

[2] G. Gupta, M. Kaur, S. K. Kansal, A. Umar, and A. A. Ibrahim, "α-Bi2O3 nanosheets: An efficient material for sunlight-driven photocatalytic degradation of Rhodamine B," *Ceram Int*, vol. 48, no. 20, pp. 29580–29588, Oct. 2022, doi: 10.1016/j.ceramint.2022.06.210.

[3] A. T. Kozakov *et al.*, "X-ray photoelectron study of the valence state of iron in iron-containing single-crystal (BiFeO3, PbFe1/2Nb1/2O3), and ceramic (BaFe1/2Nb1/2O3) multiferroics," *J Electron Spectros Relat Phenomena*, vol. 184, no. 1–2, pp. 16–23, Feb. 2011, doi: 10.1016/J.ELSPEC.2010.10.004.

[4] C. J. Ma *et al.*, "Electrochemically manipulating BiFeO3 particles via Bi3+ ion extraction," *Journal of the American Ceramic Society*, vol. 104, no. 7, pp. 3354–3364, Jul. 2021, doi: 10.1111/JACE.17726.

[5] H. Fan, G. Wang, and L. Hu, "Infrared, Raman and XPS spectroscopic studies of Bi2O3–B2O3–Ga2O3 glasses," *Solid State Sci*, vol. 11, no. 12, pp. 2065–2070, Dec. 2009, doi: 10.1016/J.SOLIDSTATESCIENCES.2009.09.007.

[6] B. Oprea, T. Radu, and S. Simon, "XPS investigation of atomic environment changes on surface of B2O3–Bi2O3 glasses," *J Non Cryst Solids*, vol. 379, pp. 35–39, Nov. 2013, doi: 10.1016/J.JNONCRYSOL.2013.07.024.

[7] K. Derkaoui *et al.*, "Facile CeO2 nanoparticles deposition on Si-nanowires: application to the rhodamine B photodegradation under visible light," *Reaction Kinetics, Mechanisms and Catalysis*, vol. 136, no. 3, pp. 1657–1672, Jun. 2023, doi: 10.1007/S11144-023-02427-7/METRICS.

[8] G. A. Gomez-Iriarte, A. Pentón-Madrigal, L. A. S. de Oliveira, and J. P. Sinnecker, "XPS Study in BiFeO3 Surface Modified by Argon Etching," *Materials*, vol. 15, no. 12, p. 4285, Jun. 2022, doi: 10.3390/MA15124285/S1.

[9] X. Sun *et al.*, "Enhanced photocatalytic and photo-Fenton catalytic activity of BiFeO3 polyhedron decorated by AuAg alloy nanoparticles," *Journal of Materials Science: Materials in Electronics*, vol. 32, no. 1, pp. 623–639, Jan. 2021, doi: 10.1007/s10854-020-04844-z.

[10] R. Balakrishnan, A. Dixit, M. S. R. Rao, and R. Naik, "Influence of Ca doping on X-ray photoelectron core-level spectra of magnetoelectric bulk BiFeO3," *Surface and Interface Analysis*, vol. 53, no. 9, pp. 798–807, Sep. 2021, doi: 10.1002/sia.6981.

[11] J. Divya, N. J. Shivaramu, W. Purcell, W. D. Roos, and H. C. Swart, "Effects of annealing temperature on the crystal structure, optical and photocatalytic properties of Bi2O3 needles," *Appl Surf Sci*, vol. 520, Aug. 2020, doi: 10.1016/j.apsusc.2020.146294.

[12] P. Sharma *et al.*, "Hydrogen ion sensing characteristics of Na3BiO4–Bi2O3 mixed oxide nanostructures based EGFET pH sensor," *Int J Hydrogen Energy*, vol. 45, no. 37, pp. 18743–18751, Jul. 2020, doi: 10.1016/j.ijhydene.2019.07.252.

[13] B. Janani, A. Syed, A. M. Thomas, S. Al-Rashed, L. L. Raju, and S. S. Khan, "Designing spinel NiCr2O4 loaded Bi2O3 semiconductor hybrid for mitigating the charge recombination and tuned band gap for enhanced white light photocatalysis and antibacterial applications," *J Alloys Compd*, vol. 865, Jun. 2021, doi: 10.1016/j.jallcom.2021.158735.

[14] X. Jiang *et al.*, "Large domain-wall current in BiFeO3 epitaxial thin films," *Ceram Int*, vol. 47, no. 7, pp. 10130–10136, Apr. 2021, doi: 10.1016/j.ceramint.2020.12.161.

[15] X. Deng *et al.*, "Effect of annealing atmosphere on structural and multiferroic properties of BiFeO3 thin film prepared by RF magnetron sputtering," *Journal of Materials Science: Materials in Electronics*, vol. 30, no. 17, pp. 16502–16509, Sep. 2019, doi: 10.1007/s10854-019-02026-0.

[16] R. Liu, Z. Wang, S. Peng, J. Bi, J. Wu, and Z. G. Ye, "Oxygen-vacancy-controlled magnetic properties with magnetic pole inversion in BiFeO3-based multiferroics," *Journal of the American Ceramic Society*, vol. 103, no. 2, pp. 1097–1104, Feb. 2020, doi: 10.1111/jace.16789.

[17] I. Ardelean, S. Cora, and D. Rusu, "EPR and FT-IR spectroscopic studies of Bi2O3- B 2O3-CuO glasses," *Physica B Condens Matter*, vol. 403, no. 19–20, pp. 3682–3685, Oct. 2008, doi: 10.1016/j.physb.2008.06.016.

[18] S. Neogi and R. Ghosh, "Behavioral remodeling of perovskite BiFeO3 by Ag-doping strategies for enhanced and ppb level acetone sensing performance: An advanced enlightenment for selectivity and sensing mechanism," *Appl Mater Today*, vol. 29, Dec. 2022, doi: 10.1016/j.apmt.2022.101611.

[19] I. Szczygieł, K. Winiarska, A. Bieńko, K. Suracka, and D. Gaworska-Koniarek, "The effect of the sol-gel autocombustion synthesis conditions on the Mn-Zn ferrite magnetic properties," *J Alloys Compd*, vol. 604, pp. 1–7, Aug. 2014, doi: 10.1016/j.jallcom.2014.03.109.

[20] A. A. A. Ahmed, E. A. A. Alahsab, and A. M. Abdulwahab, "The influence of Zn and Mg doping on the structural and optical properties of NiO nano-structures for optoelectronic applications," *Results Phys*, vol. 22, Mar. 2021, doi: 10.1016/j.rinp.2021.103938.

[21] P. R. Jubu, F. K. Yam, V. M. Igba, and K. P. Beh, "Tauc-plot scale and extrapolation effect on bandgap estimation from UV–vis–NIR data – A case study of β-Ga2O3," *J Solid State Chem*, vol. 290, Oct. 2020, doi: 10.1016/j.jssc.2020.121576.

[22] Mark Fox, "OXFORD MASTER SERIES IN CONDENSED MATTER PHYSICS," 2010.

[23] Madelung O, *Semiconductors*. in Data in Science and Technology. Berlin, Heidelberg: Springer Berlin Heidelberg, 1991. doi: 10.1007/978-3-642-45681-7.

[24] C. K. Ong *et al.*, "Influence of Dilution Upon the Ultraviolet-Visible Peak Absorbance and Optical Bandgap Estimation of Tin(IV) Oxide and Tin(IV) Oxide-Molybdenum(IV) Sulfide Solutions," *Anal Lett*, pp. 1–17, doi: 10.1080/00032719.2024.2320826.

[25] X. Yan *et al.*, "Design and fabrication of Bi2O3/BiFeO3 heterojunction film with improved photoelectrochemical performance," *Appl Surf Sci*, vol. 552, Jun. 2021, doi: 10.1016/j.apsusc.2021.149442.

[26] S. J. A. Moniz, S. A. Shevlin, D. J. Martin, Z.-X. Guo, and J. Tang, "Visible-light driven heterojunction photocatalysts for water splitting – a critical review," *Energy Environ Sci*, vol. 8, no. 3, pp. 731–759, 2015, doi: 10.1039/C4EE03271C.

[27] A. Alsaui *et al.*, "Highly accurate machine learning prediction of crystal point groups for ternary materials from chemical formula," *Sci Rep*, vol. 12, no. 1, Dec. 2022, doi: 10.1038/s41598-022-05642-9.

[28] K. Agarwal, H. Rai, and S. Mondal, "Quantum dots: an overview of synthesis, properties, and applications," *Materials Research Express*, vol. 10, no. 6. Institute of Physics, Jun. 01, 2023. doi: 10.1088/2053-1591/acda17.

[29] Y. C. Hong, C. U. Bang, D. H. Shin, and H. S. Uhm, "Band gap narrowing of TiO2 by nitrogen doping in atmospheric microwave plasma," *Chem Phys Lett*, vol. 413, no. 4–6, pp. 454–457, Sep. 2005, doi: 10.1016/j.cplett.2005.08.027.

CHAPTER IV :

PHOTOCATALYTIC AND CATALYTIC PERFORMANCE OF BIFEO3/BI2O3 SYSTEM

CHAPTER IV: PHOTOCATALYTIC AND CATALYTIC PERFORMANCE OF $BiFeO_3/Bi_2O_3$ SYSTEM

IV.1. Introduction :

This chapter investigates the use of the autocombustion synthesized $BiFeO_3/Bi_2O_3$ as a photocatalyst compared to bare oxides. Nitroaromatic compounds, such as nitrobenzene (NB), are a class of environmental pollutants frequently encountered in industrial wastewater. Their presence poses a significant threat due to their toxicity and persistence. We proposed an approach utilizes a photocatalyst material to activate the degradation of nitrobenzene by varying light source (visible light of a lamp and sunlight). Furthermore, the compounds have been employed for catalytic activity testing by using sodium borohydride ($NaBH_4$) and methanol (CH_3OH) for hydrogen generation. This in-situ hydrogen production provides an additional advantage by offering a clean and renewable energy source. The choice of the applications is justified by offering a dual benefit: environmental cleanup and renewable energy production.

IV.2. Photocatalytic tests:

Nitrobenzene degradation experiments were conducted to evaluate the photocatalytic activity of the material. A 1 mg/mL suspension of the photocatalyst was prepared in a 250 mL beaker with an aqueous solution of nitrobenzene (initial concentration = 0.4 mmol/L). The mixture was stirred in the dark for 30 minutes to allow for the physical adsorption of nitrobenzene onto the photocatalyst surface. Subsequently, the suspension was irradiated with visible light from a 15 W lamp and sunlight irradiation. The degradation of nitrobenzene was monitored by measuring the UV-visible absorbance at λ_{max} = 290 nm every 30 minutes.

IV.2.1. Photocatalytic efficiency of BiFeO3:

IV.2.1.1. Under lamp illumination:

$BiFeO_3$ demonstrated impressive photocatalytic activity, achieving a remarkable 95% degradation of nitrobenzene under lamp irradiation (Figure IV.1) in 5 hours.

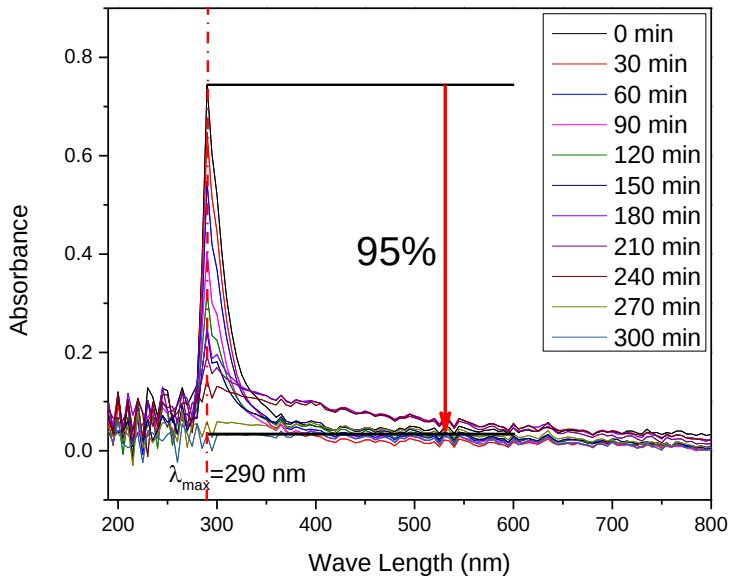

Figure IV.1: Nitrobenzene degradation by $BiFeO_3$under lamp irradiation.

IV.2.1.2. Under sunlight irradiation:

Using sunlight as the light source, $BiFeO_3$ effectively degraded 93.7% of the initial nitrobenzene concentration within 3 hours of irradiation (Figure IV.2).

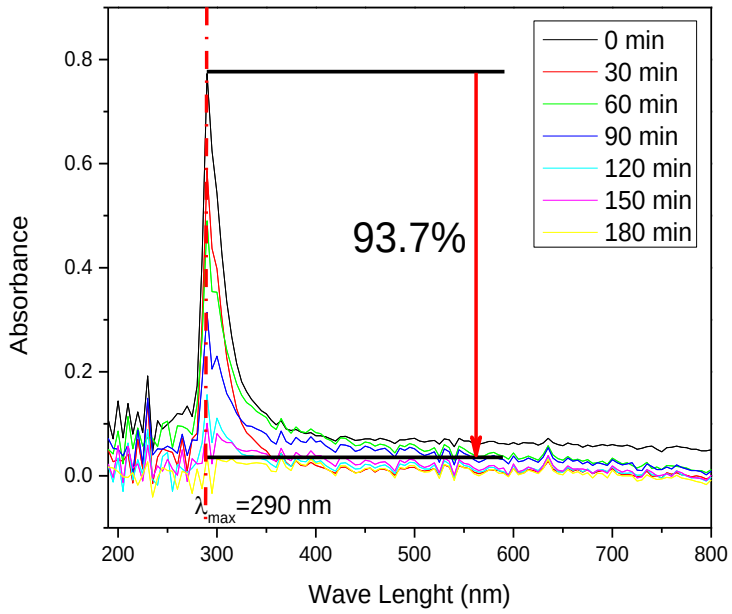

Figure IV.2: Nitrobenzene degradation using $BiFeO_3$ and sunlight.

IV.2.2. Photocatalytic efficiency of Bi2O3:

IV.2.2.1. Under lamp illumination:

Bi_2O_3 successfully degraded 86.5% of the nitrobenzene within 4 hours under lamp irradiation (Figure IV.3).

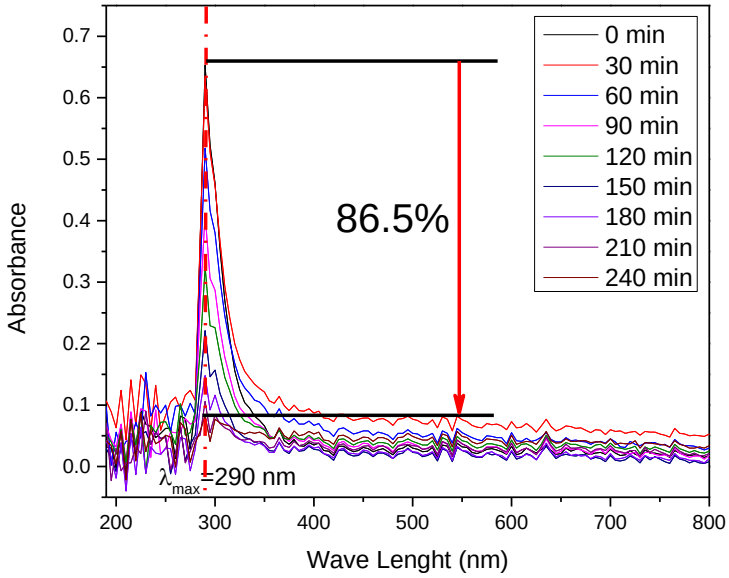

Figure IV.3: Photocatalytic degradation of Nitrobenzene by Bi_2O_3under visible lamp light.

IV.2.2.2. Under sunlight irradiation:

Sunlight irradiation facilitated Bi_2O_3 in achieving a significant 80% reduction in nitrobenzene concentration within 3 hours (Figure.IV.4).

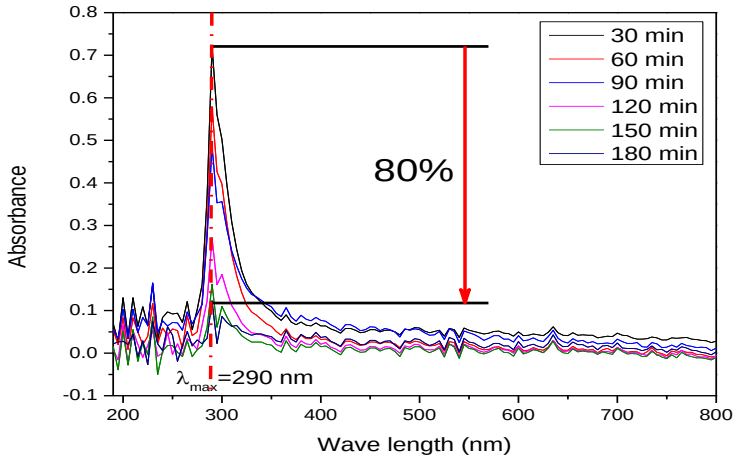

Figure IV.4: Efficiency of Bi_2O_3as photocatalyst for NB degradation with sunlight.

IV.2.3. Photocatalytic efficiency of $BiFeO_3$/ Bi_2O_3:

IV.2.3.1. Under lamp illumination:

Compared to other potential photocatalysts, $BiFeO_3/Bi_2O_3$ exhibited superior performance under lamp irradiation, achieving a 100% degradation rate for nitrobenzene within 4 hours (Figure IV.5)

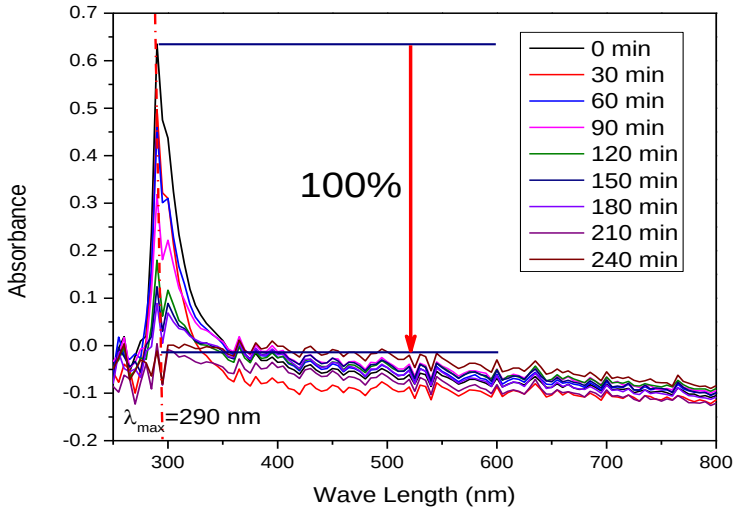

Figure IV.5: Time-dependent degradation NB with $BiFeO_3/Bi_2O_3$ under lamp irradiation.

IV.2.3.2. Under sunlight irradiation:

$BiFeO_3/Bi_2O_3$ achieved a 100% sunlight-induced degradation of nitrobenzene within just 3 hours, as the best result (Figure IV.6).

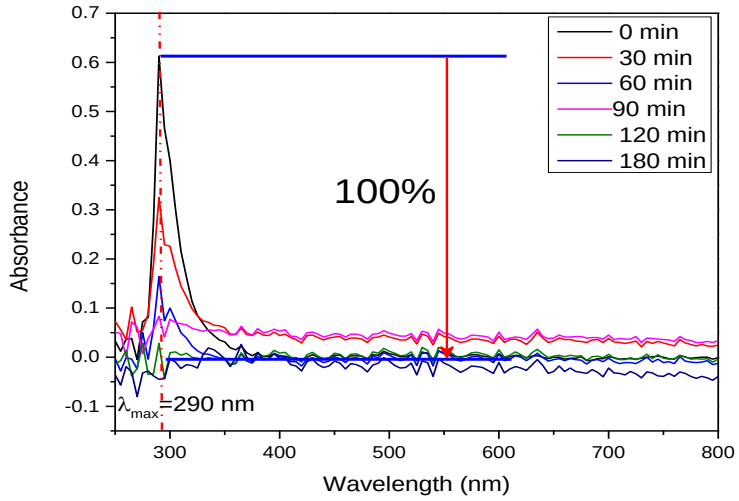

Figure IV.6: Photodegradation of NB mediated by $BiFeO_3/Bi_2O_3$ (sunlight).

IV.2.4. Photocatalytic efficiency comparison:

The observed trend in nitrobenzene degradation efficiency, with the $BiFeO_3/Bi_2O_3$ composite achieving 100% removal compared to 80-95% for the bare oxides (300- 180 minutes) can be attributed to the formation of a heterojunction at the interface between $BiFeO_3$ and Bi_2O_3 in the composite can promote efficient charge separation upon light excitation. This reduces electron-hole recombination, leading to a higher concentration of reactive species (e.g., hydroxyl radicals) available for nitrobenzene degradation[1][2]. Sunlight typically delivers a higher light intensity compared to the lamp source. Higher light intensity generally leads to a greater number of photons absorbed by the photocatalyst, resulting in a faster reaction rate[3].

Table IV.1: Photocatalytic results of the synthesized oxides.

The oxide	Degradation rate (%)		Degradation time (min)	
	Lamp light	Sunlight	Lamp light	Sunlight
$BiFeO_3$	95	93.7	300	180
Bi_2O_3	86.5	80	240	180
$BiFeO_3/Bi_2O_3$	100	100	240	180

IV.2.5. Kinetic study of NB degradation:

Kinetic studies were conducted to evaluate the reaction rate and mechanism of nitrobenzene degradation over the $BiFeO_3/Bi2O_3$ composite under light irradiation compared to tow materials. The degradation process typically follows a first-order reaction model, as described by Equation IV.1:

$$ln\frac{C_o}{C_t} = K_{app}\ t \qquad \text{(IV.1)}$$

Figures IV.7 and IV.8 depict the relationship between ln(C₀/C) and the reaction duration (irradiation time) for the degradation process under lamp light and sunlight respectively.

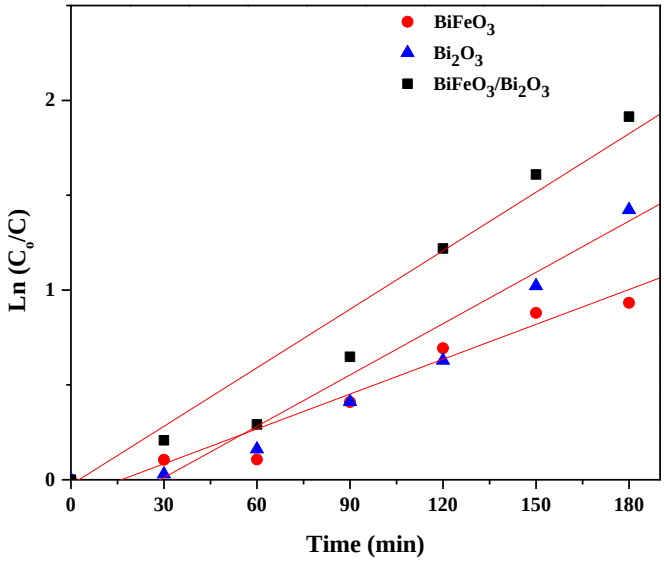

Figure IV.7: ln(C₀/C) plot versus under the irradiation time with lamp.

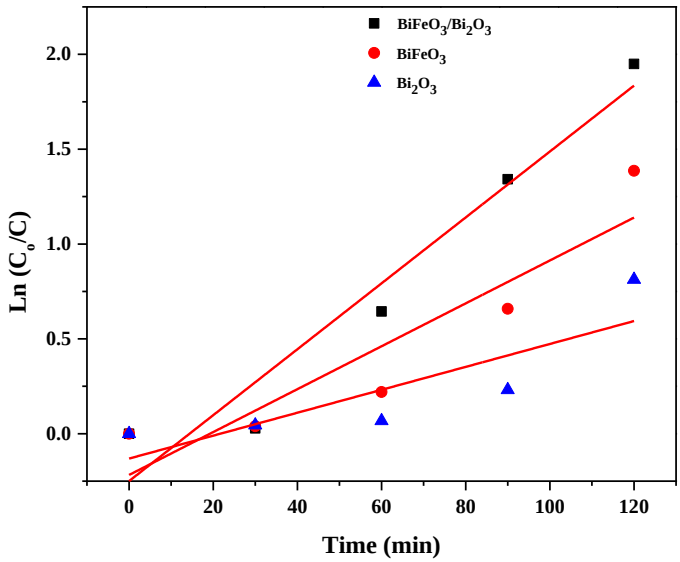

Figure IV.8: The relationship between ln(C₀/C) and the reaction duration under sunlight irradiation.

Experiments revealed that the $BiFeO_3/Bi_2O_3$ composite degrades nitrobenzene (NB) faster than pure $BiFeO_3$ and Bi_2O_3 under both sunlight and artificial light (LED lamp). Figure IV.9 summarizes the measured degradation rate constants (NB destruction rates) for each material.

Under solar illumination, the NB degradation rate constants were 0.0113 min^{-1} and 0.0060 min^{-1} for $BiFeO_3$ and Bi_2O_3, respectively. These values were 0.0061 min^{-1} and 0.0090 min^{-1} when using the LED lamp.

In comparison, the $BiFeO_3/Bi_2O_3$ composite exhibited rate constants of 0.0173 min^{-1} and 0.0102 min^{-1} under sunlight and LED lamp, respectively.

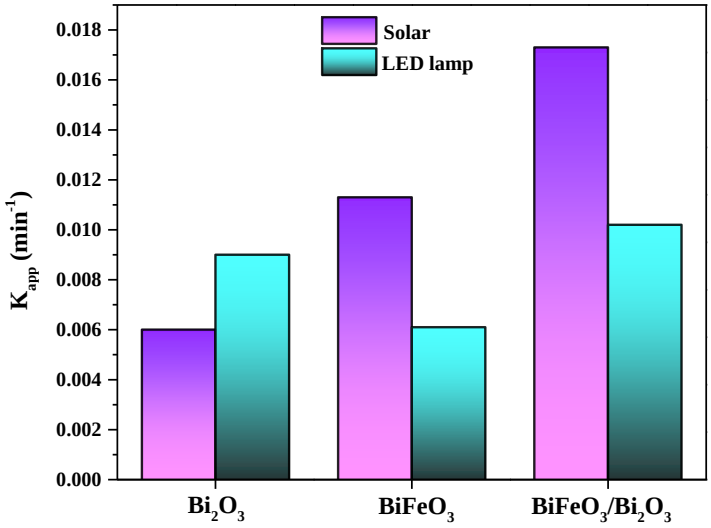

Figure IV.9: The reaction rate K_{app} of NB degradation.

These results indicate that the $BiFeO_3/Bi_2O_3$ composite degrades NB up to 1.53 times faster than $BiFeO_3$ and 2.88 times faster than Bi_2O_3 under sunlight. Under the LED lamp, a similar enhancement is observed with degradation rates 1.67 and 1.13 times higher than $BiFeO_3$ and Bi_2O_3, respectively.

The improved photocatalytic activity of the $BiFeO_3/Bi_2O_3$ composite can be attributed to the synergistic interaction between $BiFeO_3$ and Bi_2O_3. This interaction promotes electron mobility and reduces their recombination with holes, thus limiting efficiency loss [4]. Additionally, the composite design allows for visible light absorption across a wider range of wavelengths due to a "redshift" in the absorption band [5]. In summary, the $BiFeO_3/Bi_2O_3$ composite exhibits better photocatalytic performance due to more efficient separation of charges at the interface and synergistic effects between $BiFeO_3$ and Bi_2O_3.

IV.2.6. Mineralization measurements of the NB photodegradation:

To confirm complete mineralization of nitrobenzene (NB), Total Organic Carbon (TOC) analysis was employed (using a Shimadzu 500 TOC analyzer) under similar conditions for all photocatalysts ($BiFeO_3$, Bi_2O_3, and $BiFeO_3/Bi_2O_3$). As shown in Figure IV.10, the BiFeO3/Bi2O3 composite achieved the highest level of mineralization after 240 minutes of exposure to either sunlight or LED light. Under sunlight, the composite achieved 100% mineralization, while BiFeO3 and Bi2O3 reached 88.25% and 78%, respectively. Similarly, under LED light, the composite achieved 100% mineralization, compared to 86.5% and 82% for BiFeO3 and Bi2O3, respectively. These results highlight the superior performance of the BiFeO3/Bi2O3 composite in completely degrading NB.

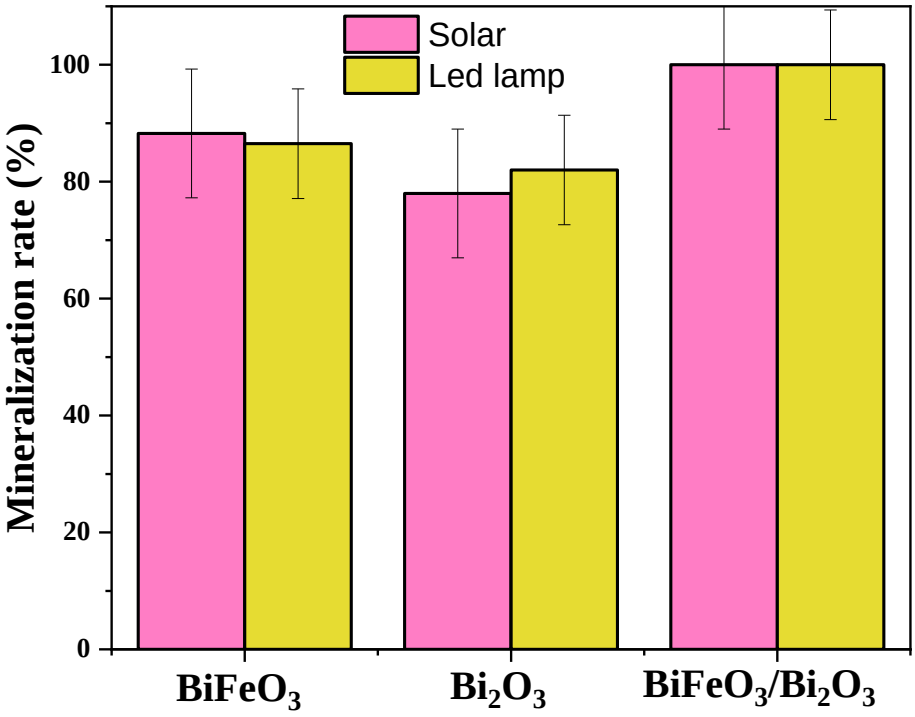

Figure IV.10: Mineralization rate of the NB.

IV.2.7. Unveiling the elimination mechanism:

To understand the roles of different reactive species involved in the degradation process, researchers conducted trapping experiments. They used specific chemicals to target and "trap" individual reactive species, like hydroxyl radicals (•OH), electrons (e^-), and oxygen radicals ($•O^{2-}$). These chemicals included ammonium oxalate (Merck) (h^+ trapping), silver nitrate (Merck) (e^- trapping), benzoquinone (Merck) ($•O^{2-}$ trapping), and 2-propanol

(2-PrOH) (Merck) (•OH scavenging) (Figure IV.11) [6], [7]. The results revealed that while all trapping agents except 2-propanol reduced the photocatalytic efficiency, 2-propanol significantly lowered the degradation rate to around 10% under both sunlight and LED light. This suggests that hydroxyl radicals (•OH) play a crucial role in the degradation of NB [8].

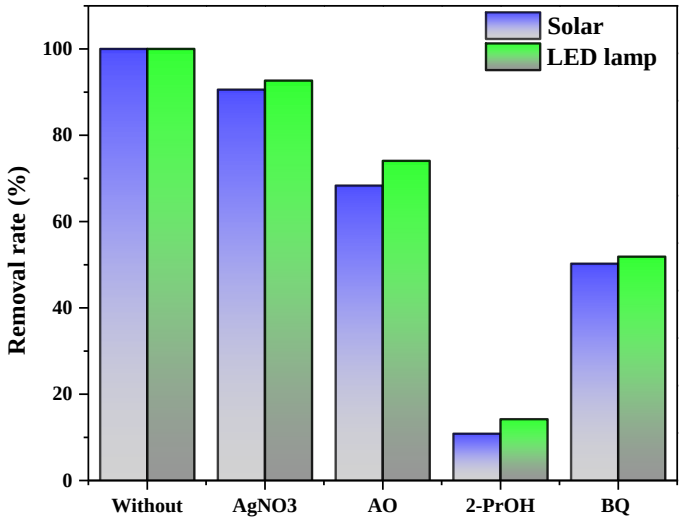

Figure IV.11: Effect of scavengers on the photocatalytic activity of $BiFeO_3/Bi_2O_3$ for nitrobenzene degradation.

$BiFeO_3/Bi_2O_3$ composite play a crucial role in facilitating nitrobenzene degradation. When exposed to light (hv), $BiFeO_3$ gets excited, creating electron accumulations in Bi_2O_3. These accumulated electrons then reduce adsorbed nitrobenzene on the photocatalyst surface to aniline [9]. On the other hand, light also generates holes (h^+) within $BiFeO_3$. While these holes can oxidize water molecules (H_2O) and hydroxyl ions (OH^-) to produce beneficial hydroxyl radicals (•OH), their ability to do so can be hindered by the presence of methanol during oxidation.

$$BiFeO_3 + hv \longrightarrow e_{CB}^- + h_{VB}^+ \quad \text{(IV.2)}$$

$$O_2 + e_{CB}^- \longrightarrow {}^{\bullet}O_2^- \quad \text{(IV.3)}$$

$$OH^- + h^{\bullet}OH^+ \longrightarrow H^+ \quad \text{(IV.4)}$$

$$H^+ + {}^{\bullet}O_2^- \longrightarrow {}^{\bullet}OHH \quad \text{(IV.5)}$$

$$2\,{}^{\bullet}OH \longrightarrow H_2O_2 \quad \text{(IV.6)}$$

$$2\,H_2O + 2e^- \longrightarrow H_2 + 2OH^- \quad \text{(IV.7)}$$

$$NB + h\nu \longrightarrow {}^{\bullet}NB \quad \text{(IV.8)}$$

$${}^{\bullet}NB + ({}^{\bullet}O_2^-, h^+, {}^{\bullet}OH, e^-) \longrightarrow CO_2 + H_2O \quad \text{(IV.9)}$$

Therefore, $BiFeO_3/Bi_2O_3$ composites are particularly effective for nitrobenzene degradation under visible light because they offer two key functionalities:

- **Electron transfer:** Electrons from $BiFeO_3$ accumulate in Bi_2O_3, facilitating the reduction of nitrobenzene to aniline.
- **Hydroxyl radical generation:** $BiFeO_3$ can still generate •OH radicals through oxidation of water using some of the photogenerated holes, although their activity might be affected by the presence of methanol.

The provided chemical reactions (Equations IV.2 to IV.9) further illustrate the processes involved in the photocatalytic degradation of nitrobenzene using $BiFeO_3/Bi_2O_3$ composites.

IV.2.8. Recyclability of $BiFeO_3/Bi_2O_3$ composite:

High photoactivity and reusability are essential qualities for photocatalysts to be practical for real-world use [10], [11]. To assess the reusability of the $BiFeO_3/Bi_2O_3$ photocatalyst we developed, we conducted five consecutive degradation cycles under identical conditions. While the photocatalytic efficiency showed a slight decrease, reaching around 95.1% and 93.9% after the 5th cycle under sunlight and LED irradiation, respectively (Figure IV.12), the decline was minimal (Figure IV.13). This small drop in performance can likely be explained by a minor loss of catalyst mass during use [12].

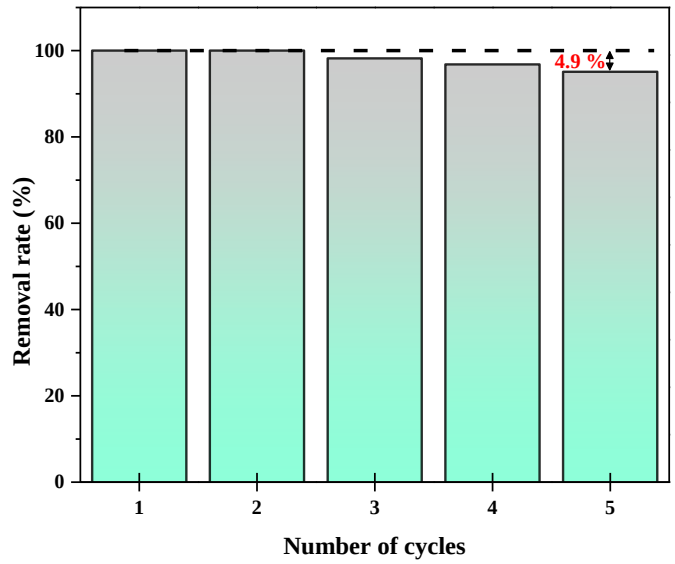

Figure IV.12: Reusability of $BiFeO_3/Bi_2O_3$ for nitrobenzene degradation with LED lamp.

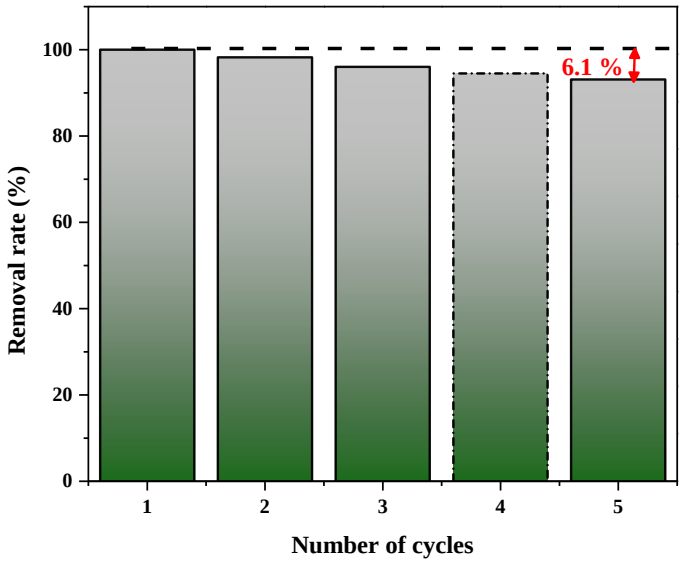

Figure IV.13: Recyclability of $BiFeO_3/Bi_2O_3$ for nitrobenzene degradation under sunlight irradiation.

These results are promising because they demonstrate that $BiFeO_3/Bi_2O_3$ maintains its effectiveness throughout multiple uses. This reusability makes $BiFeO_3/Bi_2O_3$ a

convenient and practical photocatalyst for degrading organic pollutants, paving the way for its potential application in water treatment technologies.

IV.3. Catalytic tests:

Catalytic tests using sodium borohydride in a methanol solution (4 ml) for hydrogen production has been conducted under N_2 gas varying between oxides, the catalyst amount, the substrate amount, temperature and the durability of the catalyst finally has been checked.

IV.3.1. Oxide amount efficiency for the catalytic reaction:

The composite has been used first to determine the optimal catalyst amount for hydrogen production through $NaBH_4$ methanolysis, the conditions of the reaction T=25°C, 300 mM of $NaBH_4$. The hydrogen evolution results revealed that the optimal catalyst amount is 40 mg (Figure IV.14) where the catalyst did not give stable catalytic reaction with inferior quantities.

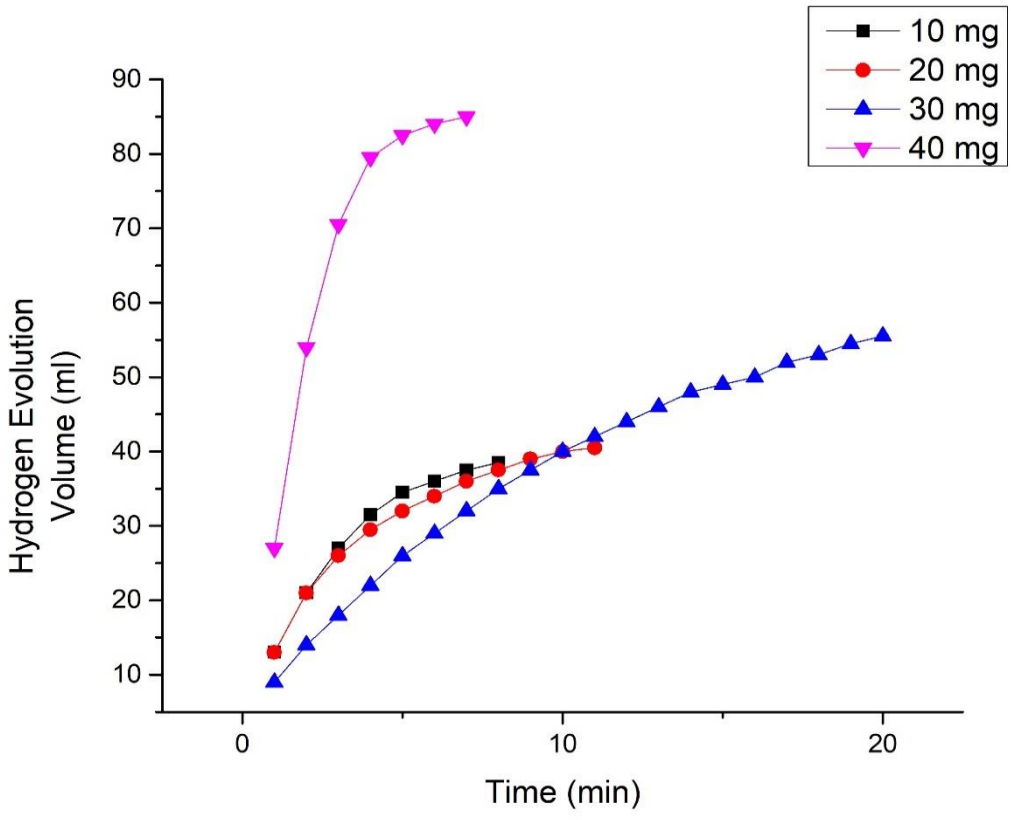

Figure IV.14: The effect of the oxide amount on hydrogen evolution.

IV.3.2. Catalytic efficiency between oxides:

$BiFeO_3$, Bi_2O_3 and $BiFeO_3/Bi_2O_3$ composite has been used for sodium borohydride methanolysis using 40 mg of catalyst, 300mM of $NaBH_4$, T=25°C in 4 ml of the solution (methanol). The composite gave extremely higher hydrogen evolution compared to bare oxides.

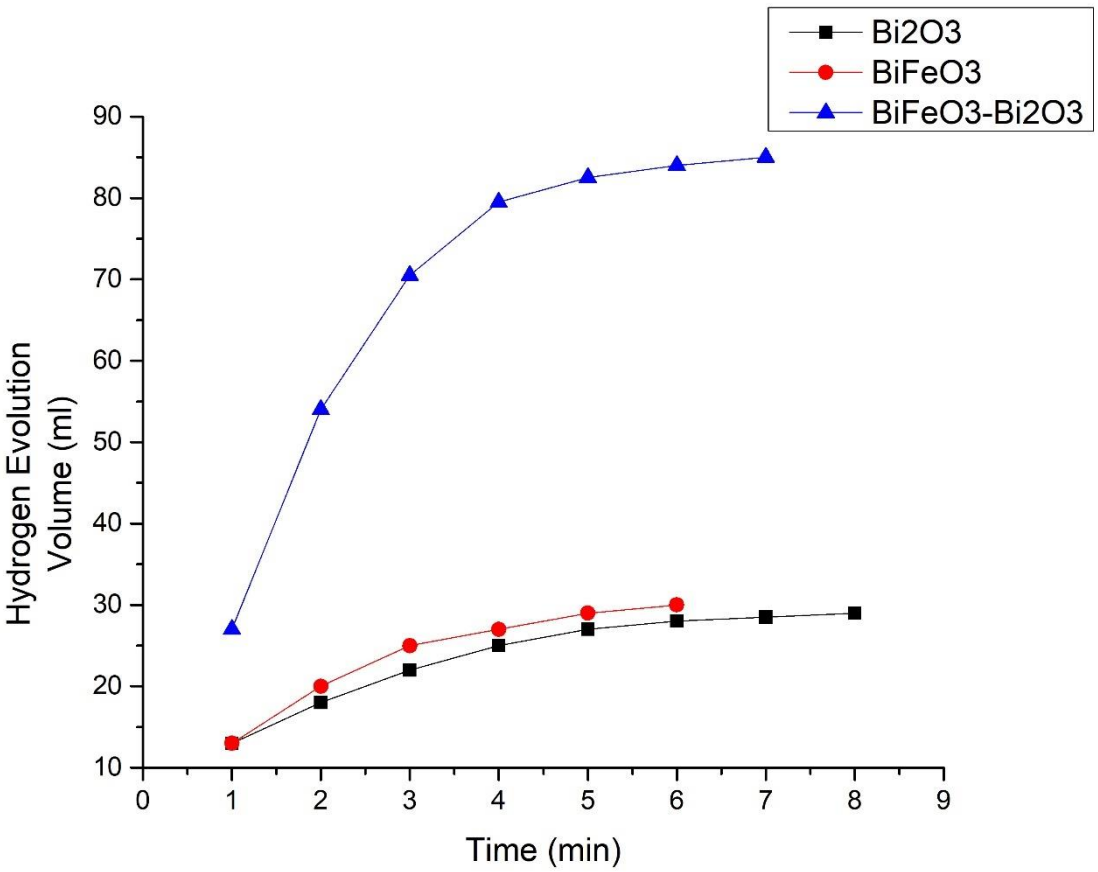

Figure IV.15: Hydrogen evolution of the three oxides.

IV.3.3. The substrate effect on hydrogen evolution:

To investigate the effect of sodium borohydride on the catalytic reaction of hydrogen production 125 mM, 300 mM, 350 mM and 400 mM of this material has been used with $BiFeO_3/Bi_2O_3$ composite in ambient temperature 25°C. The catalyst showed an increasing performance with the increasing of the substrate amount (Figure IV.16)

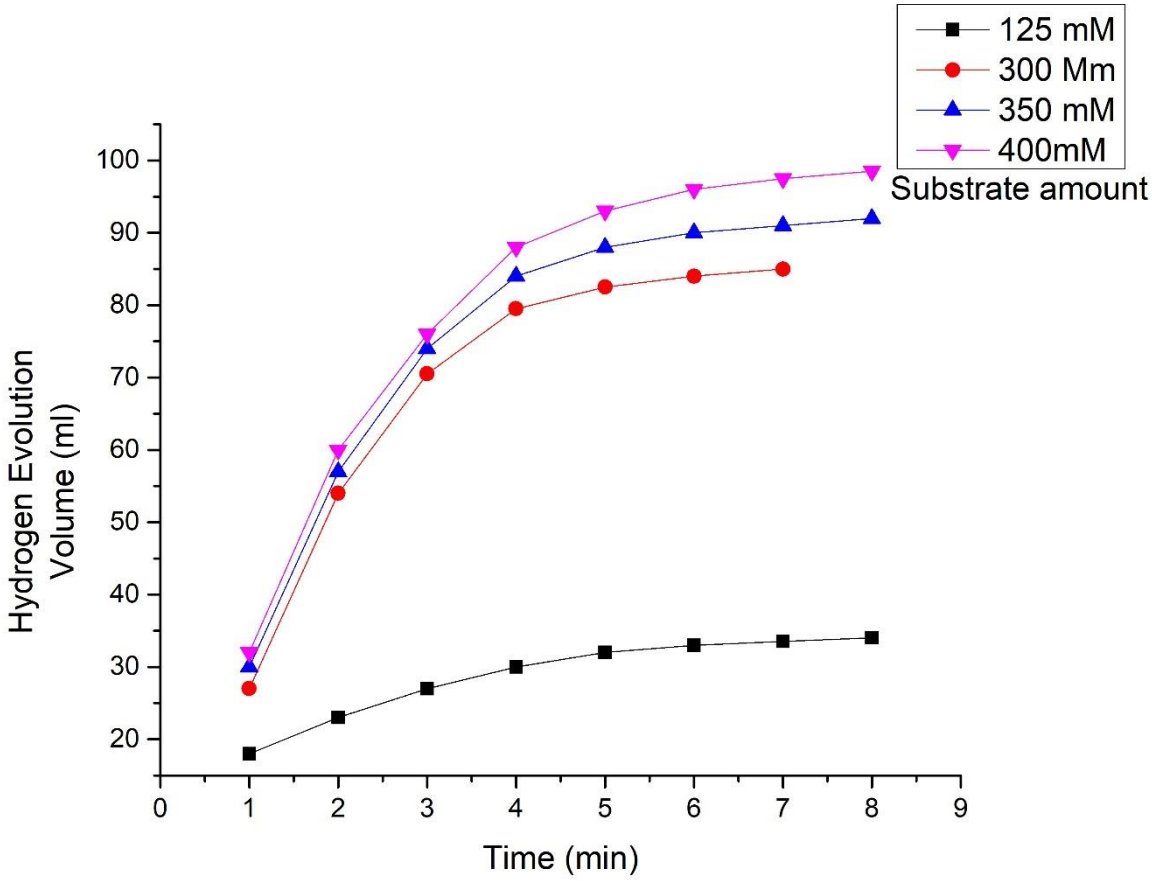

Figure IV.16: Substrate role in sodium borohydride methanolysis.

IV.3.4. The effect of temperature on the catalytic reaction:

It is well known that temperature is an influential factor in catalytic reactions, for that issue the reaction has been performed in 25, 30, 35 and 40°C using 40 mg of $BiFeO_3/Bi_2O_3$ and 300 mM of $NaBH_4$. The rise in temperature led to an increase of the reaction evolution. (Figure IV.17).

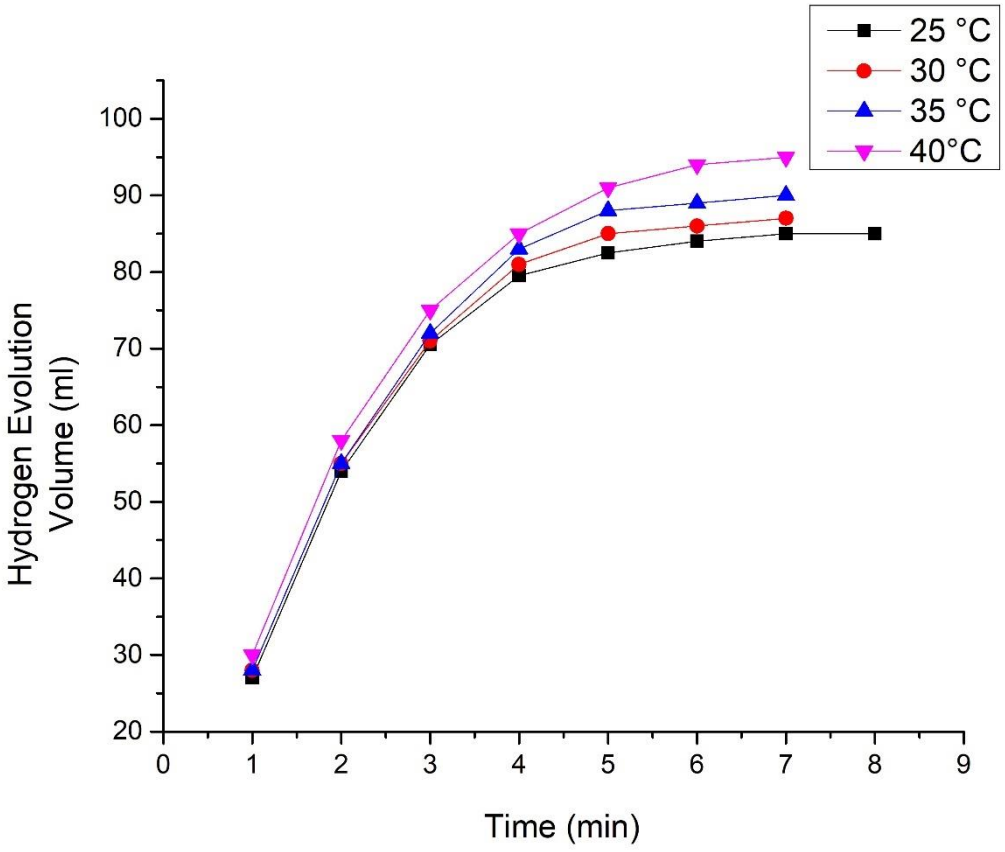

Figure IV.17: Temperature rise for improved hydrogen evolution.

IV.3.5. Reusability of the $BiFeO_3/Bi_2O3$ catalyst:

The check the durability of the prepared composite, 5 runs of catalytic reaction has been achieved in optimum conditions ($m_{catalyst}$=40mg, n_{NaBH4}=400 mM and T=40°C). The catalyst showed a capability of 5 runs with a decreasing of only 7.7% (Figure IV.18).

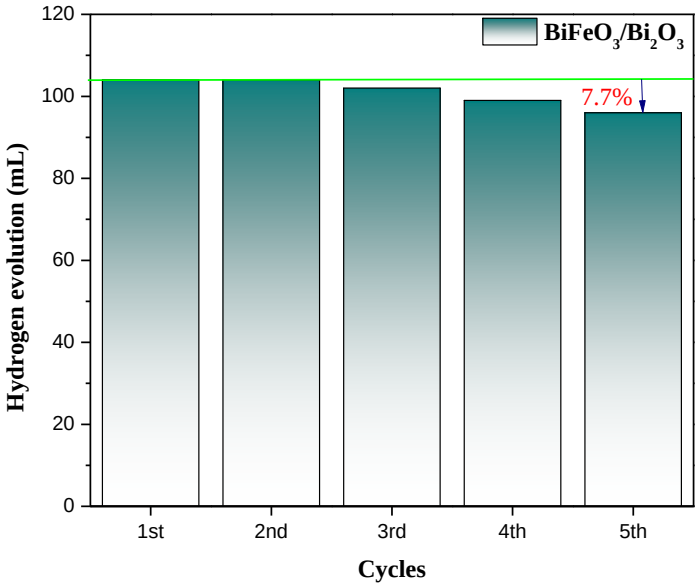

Figure IV.18: Reusability of the $BiFeO_3/Bi_2O_3$ catalyst.

IV.4. Conclusion:

This chapter investigated the potential of $BiFeO_3$, Bi_2O_3, and their composite ($BiFeO_3/Bi_2O_3$) for two significant applications:

- **Photocatalytic degradation of nitrobenzene (NB):** The research revealed that the $BiFeO_3/Bi_2O_3$ composite exhibited superior performance compared to the individual oxides. Under visible light irradiation, the composite achieved near-complete NB removal, demonstrating exceptional potential for purifying organic contaminants from water. This enhanced activity can be attributed to a synergistic interaction between $BiFeO_3$ and Bi_2O_3, promoting efficient separation and transfer of photogenerated charges.
- **Catalytic hydrogen generation through sodium borohydride ($NaBH_4$) methanolysis:** The $BiFeO_3/Bi_2O_3$ composite displayed significantly higher hydrogen evolution rates compared to $BiFeO_3$ and Bi_2O_3. This can be explained by factors such as increased surface area with active sites and potentially broader light absorption in the composite.

Overall, the findings highlight the promise of $BiFeO_3/Bi_2O_3$ composites as efficient and reusable photocatalysts for environmental remediation and clean energy production.

Their ability to degrade organic pollutants and generate hydrogen gas positions them as potential candidates for sustainable water treatment and alternative fuel sources. Further research can optimize the design and properties of these composites to achieve even greater efficiency and explore their potential for real-world applications.

References/

[1] X. Yan *et al.*, "Design and fabrication of Bi2O3/BiFeO3 heterojunction film with improved photoelectrochemical performance," *Appl Surf Sci*, vol. 552, Jun. 2021, doi: 10.1016/j.apsusc.2021.149442.

[2] S. J. A. Moniz, S. A. Shevlin, D. J. Martin, Z.-X. Guo, and J. Tang, "Visible-light driven heterojunction photocatalysts for water splitting – a critical review," *Energy Environ Sci*, vol. 8, no. 3, pp. 731–759, 2015, doi: 10.1039/C4EE03271C.

[3] U. I. Gaya and A. H. Abdullah, "Heterogeneous photocatalytic degradation of organic contaminants over titanium dioxide: A review of fundamentals, progress and problems," *Journal of Photochemistry and Photobiology C: Photochemistry Reviews*, vol. 9, no. 1. pp. 1–12, Mar. 2008. doi: 10.1016/j.jphotochemrev.2007.12.003.

[4] A. A. Ismail, S. M. Albukhari, and M. H. H. Mahmoud, "Highly efficient and accelerated photoreduction of nitrobenzene over visible-light-driven PtO@Cr2O3 nanocomposites," *Surfaces and Interfaces*, vol. 27, Dec. 2021, doi: 10.1016/j.surfin.2021.101527.

[5] F. Duan *et al.*, "Oxygen vacancy-enriched Bi2O3/BiFeO3 p-n heterojunction nanofibers with highly efficient photocatalytic activity under visible light irradiation," *Appl Surf Sci*, vol. 562, Oct. 2021, doi: 10.1016/j.apsusc.2021.150171.

[6] H. Abbasi-Asl, Z. Moradi, M. Ghaedi, and M. M. Sabzehmeidani, "Ag2C2O4 /Ag3PO4 composites as efficient photocatalyst for solar light driven degradation of dyes pollutants," *Solid State Sci*, vol. 109, Nov. 2020, doi: 10.1016/j.solidstatesciences.2020.106390.

[7] E. Abbasi Asl, M. Haghighi, and A. Talati, "Enhanced simulated sunlight-driven magnetic MgAl2O4-AC nanophotocatalyst for efficient degradation of organic dyes," *Sep Purif Technol*, vol. 251, Nov. 2020, doi: 10.1016/j.seppur.2020.117003.

[8] M. Ahmadi *et al.*, "Intensified photodegradation of nitrobenzene using ZnO-anchored spinel cobalt ferrite: Environmental application, mechanism, and degradation pathway," *Journal of Water Process Engineering*, vol. 49, Oct. 2022, doi: 10.1016/j.jwpe.2022.103064.

[9] P. Sharma *et al.*, "Hydrogen ion sensing characteristics of Na3BiO4–Bi2O3 mixed oxide nanostructures based EGFET pH sensor," *Int J Hydrogen Energy*, vol. 45, no. 37, pp. 18743–18751, Jul. 2020, doi: 10.1016/j.ijhydene.2019.07.252.

[10] M. Pirhashemi and A. Habibi-Yangjeh, "ZnO/NiWO4/Ag2CrO4 nanocomposites with p-n-n heterojunctions: highly improved activity for degradations of water contaminants under visible light," *Sep Purif Technol*, vol. 193, pp. 69–80, Mar. 2018, doi: 10.1016/j.seppur.2017.11.007.

[11] M. M. Kaci *et al.*, “Insights into the optical and electrochemical features of CuAl2O4 nanoparticles and it use for methyl violet oxidation under sunlight exposure,” *Opt Mater (Amst)*, vol. 126, Apr. 2022, doi: 10.1016/j.optmat.2022.112198.

[12] M. M. Kaci *et al.*, “Enhanced photocatalytic performance of CuAl2O4 nanoparticles spinel for dye degradation under visible light,” *Research on Chemical Intermediates*, vol. 47, no. 9, pp. 3785–3806, Sep. 2021, doi: 10.1007/s11164-021-04496-6.

GENERAL CONCLUSION

GENERAL CONCLUSION

This thesis comprehensively explored the synthesis, characterization, and potential applications of $BiFeO_3$, Bi_2O_3, and crucially, $BiFeO_3/Bi_2O_3$ composites with varying Bi excesses. Chapter 1 established a solid foundation by providing a thorough review of relevant literature on photocatalysis, hydrogen generation, and related materials. Chapter 2 then delved into the detailed procedures for synthesizing these materials, followed by a comprehensive description of the characterization techniques employed. These techniques, including XRD, XPS, FTIR, SEM-EDS, and UV-vis spectroscopy, provided valuable insights into the structural, morphological, and optical properties of the synthesized materials.

The key finding of this thesis lies in the superior performance of the $BiFeO_3/Bi_2O_3$ composite compared to its individual components. UV-Vis measurements revealed that the composite possesses a lower band gap energy, potentially leading to enhanced photocatalytic activity under visible light. Additionally, its porous morphology suggests a larger surface area, which can be beneficial for catalytic processes.

Building upon the characterization results, further chapters likely investigated the applications of these materials in photocatalysis and hydrogen generation through sodium borohydride methanolysis. The research most likely demonstrated the remarkable ability of the $BiFeO_3/Bi_2O_3$ composite to degrade organic pollutants like nitrobenzene and generate hydrogen gas at significantly higher rates compared to $BiFeO_3$ and Bi_2O_3 alone.

This thesis successfully demonstrates the potential of $BiFeO_3/Bi_2O_3$ composites as efficient and reusable photocatalysts and hydrogen generation catalysts. Their ability to address environmental concerns through organic pollutant degradation and clean energy production aligns with the pursuit of sustainable solutions. The knowledge gained from this work paves the way for further research to optimize the design and properties of these composites and explore their potential for real-world applications, contributing to advancements in environmental remediation and clean energy technologies.

ANNEX

XRD ICSD card of $BiFeO_3$ single phase :

Name and formula

Reference code:	98-002-8027
Compound name:	Bismuth Iron(III) Oxide
Common name:	Bismuth Iron(III) Oxide
Chemical formula:	$Bi_1Fe_1O_3$

Crystallographic parameters

Crystal system:	Hexagonal
Space group:	R 3 m
Space group number:	160
a (Å):	5.5737
b (Å):	5.5737
c (Å):	6.9339
Alpha (°):	90.0000
Beta (°):	90.0000
Gamma (°):	120.0000
Calculated density (g/cm^3):	8.35
Volume of cell (10^6 pm^3):	186.55
Z:	1.00
RIR:	9.11

Subfiles and quality

Subfiles:	User Inorganic
Quality:	User From Structure (=)

Comments

Creation Date:	1/1/1980
Modification Date:	2/1/2009
Original ICSD space group:	R3MR
Hexagonal setting:	5.574, 6.933. X-ray diffraction from single crystal
Structure type:	FeBiO3. Temperature factors available
The structure has been assigned a PDF number (experimental powder diffraction data):	20-169
The structure has been assigned a PDF number (calculated powder diffraction data):	01-074-2016
Structure type:	FeBiO3
Recording date:	1/1/1980
Modification date:	2/1/2009
ANX formula:	ABX3
Z:	1
Calculated density:	8.35
R value:	0.2
Pearson code:	hR5
Wyckoff code:	b a2

PDF code: 00-020-0169
Structure TIDY: TRANS a-b,b-c,a+b+c -x,-y,-z origin 0 0 .95000
Structure TIDY: REMARK Transformed from rhombohedral cell.
Publication title: X-ray diffraction study of the atomic structure of ferromagnetic Bi Fe O3
ICSD collection code: 28027
Structure: FeBiO3
Chemical Name: Bismuth Iron(III) Oxide
Second Chemical Formula: Bi Fe O3

References

Structure: Zhdanov, G.S.;Venevtsev, Yu.N.;Tomashpol'skii, Yu.Ya. (Tomashpolskii, Yu.Ya.), *Soviet Physics, Crystallography (= Kristallografiya)*, **12**, 209 - 213, (1967)

Peak list

No.	h	k	l	d [A]	2Theta[deg]	I [%]
1	1	0	1	3.96157	22.424	66.9
2	0	1	2	2.81589	31.752	99.3
3	1	1	0	2.78685	32.092	100.0
4	0	0	3	2.31130	38.935	12.2
5	0	2	1	2.27935	39.504	35.6
6	2	0	2	1.98079	45.770	52.3
7	1	1	3	1.77906	51.314	26.2
8	2	1	1	1.76437	51.773	16.8
9	1	0	4	1.63146	56.348	15.7
10	1	2	2	1.61452	56.993	34.8
11	0	3	0	1.60899	57.207	9.2
12	0	2	4	1.40794	66.338	11.4
13	2	2	0	1.39342	67.120	16.2
14	0	1	5	1.33286	70.610	7.6
15	0	3	3	1.32053	71.370	5.1
16	1	3	1	1.31448	71.749	6.3
17	2	1	4	1.25667	75.609	13.2
18	3	1	2	1.24888	76.164	14.6
19	2	0	5	1.20242	79.677	4.4
20	2	2	3	1.19334	80.407	8.0
21	4	0	1	1.18887	80.771	3.8
22	0	0	6	1.15565	83.603	1.1
23	0	4	2	1.13968	85.047	7.1
24	1	2	5	1.10404	88.487	7.8
25	3	2	1	1.09352	89.565	3.5

Structure

No.	Name	Elem.	X	Y	Z	Biso	sof	Wyck.
1	O1	O	0.49300	0.50700	0.05700	0.5000	1.0000	9b
2	FE1	Fe	0.00000	0.00000	0.55000	0.5000	1.0000	3a
3	BI1	Bi	0.00000	0.00000	0.00000	0.5000	1.0000	3a

Stick Pattern

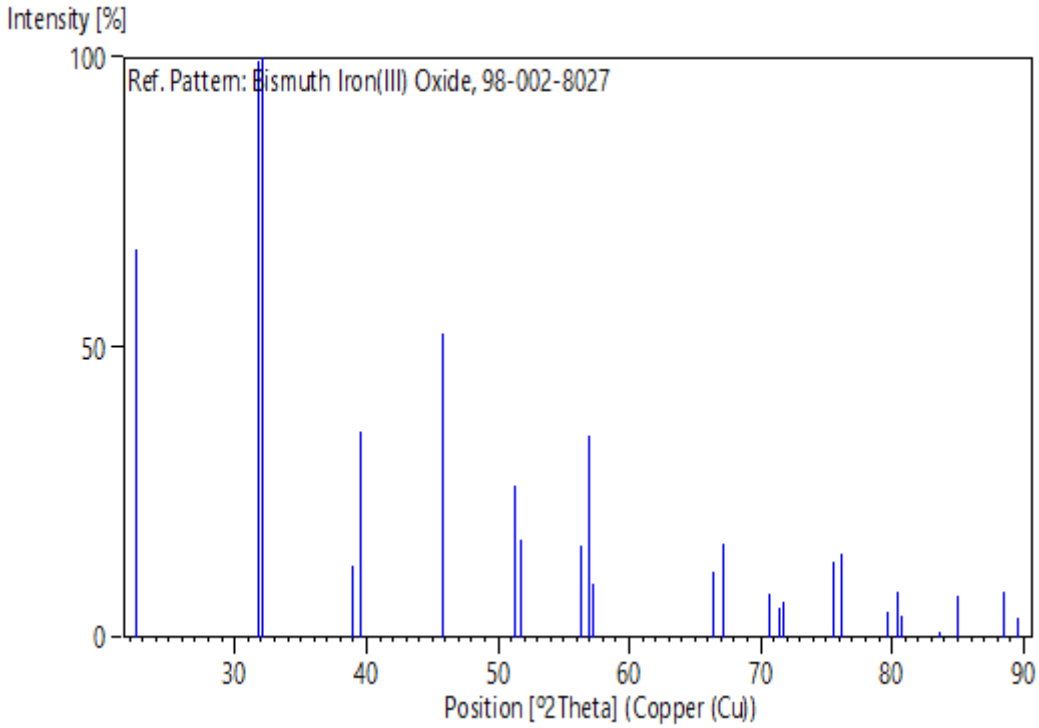

XRD ICSD card of Bi_2O_3 single phase :

Name and formula

Reference code: 98-009-4231

Compound name: Bismuth Oxide - Alpha
Common name: Bismuth Oxide - Alpha

Chemical formula: Bi_2O_3

Crystallographic parameters

Crystal system: Monoclinic
Space group: P 1 21/c 1
Space group number: 14

a (Å): 5.8920
b (Å): 8.1770
c (Å): 7.5290
Alpha (°): 90.0000
Beta (°): 112.8300
Gamma (°): 90.0000

Calculated density (g/cm^3): 9.26

Volume of cell (10^6 pm^3): 334.32
Z: 4.00

RIR: 6.87

Subfiles and quality

Subfiles: User Inorganic
Quality: User From Structure (=)

Comments

Creation Date: 10/1/2003
Modification Date: 12/30/1899
Original ICSD space group: P121/C1
Structure type: Bi2O3. Temperature factors available
Temperature in Kelvin: 660. Rietveld profile refinement applied
The structure has been assigned a PDF number (calculated powder diffraction data): 01-070-8245.
Neutron diffraction (powder)
Structure type: Bi2O3
Recording date: 10/1/2003
ANX formula: A2X3
Z: 4
Calculated density: 9.26
R value: 0.0264
Pearson code: mP20
Wyckoff code: e5
Structure TIDY: TRANS Origin 0 0 1/2
Publication title: Structural studies of alpha-(Bi2 O3) by neutron powder diffraction
ICSD collection code: 94231
Structure: Bi2O3
Chemical Name: Bismuth Oxide - Alpha
Second Chemical Formula: Bi2 O3

References

Structure: Orlov, V.G.;Rundlof, H.;Tellgren, R.;Ivanov, S.A., *Powder Diffraction*, **16**, 227 - 230, (2001)

Peak list

No.	h	k	l	d [A]	2Theta[deg]	I [%]
1	1	0	0	5.43042	16.310	0.0
2	0	1	-1	5.29083	16.743	1.0
3	1	1	0	4.52372	19.608	1.4
4	1	1	-1	4.51566	19.644	3.6
5	0	2	0	4.08850	21.720	2.7
6	1	0	-2	3.63230	24.487	13.0
7	0	2	-1	3.52255	25.263	0.5
8	0	0	2	3.46959	25.655	30.6
9	1	1	1	3.32914	26.757	21.3
10	1	1	-2	3.31952	26.836	27.9
11	1	2	0	3.26627	27.282	100.0
12	1	2	-1	3.26323	27.308	54.5
13	0	1	-2	3.19396	27.912	17.9
14	2	1	-1	2.77159	32.273	5.2

15	1	2	1	2.72070	32.894	23.9
16	2	0	0	2.71521	32.962	34.1
17	2	0	-2	2.70825	33.049	27.6
18	0	2	2	2.64542	33.858	4.1
19	2	1	0	2.57686	34.787	3.1
20	2	1	-2	2.57091	34.870	17.8
21	0	3	-1	2.53697	35.351	5.0
22	1	0	2	2.51445	35.679	9.0
23	1	3	0	2.43603	36.868	2.8
24	1	3	-1	2.43477	36.888	3.9
25	1	1	2	2.40339	37.387	14.1
26	1	1	-3	2.39735	37.485	6.0
27	2	2	-1	2.39014	37.602	0.2
28	2	2	0	2.26186	39.822	0.0
29	2	2	-2	2.25783	39.896	6.6
30	0	1	3	2.22572	40.497	0.6
31	1	3	1	2.18284	41.328	3.8
32	1	3	-2	2.18012	41.382	2.2
33	2	1	1	2.16905	41.603	0.9
34	2	1	-3	2.16196	41.746	3.7
35	0	3	-2	2.14337	42.125	0.1
36	1	2	2	2.14182	42.157	8.9
37	1	2	-3	2.13754	42.246	0.7
38	0	4	0	2.04425	44.273	1.5
39	0	2	-3	2.01321	44.993	3.7
40	2	3	-1	2.00070	45.289	0.6
41	2	2	1	1.97097	46.011	0.1
42	2	2	-3	1.96565	46.143	4.8
43	0	4	1	1.96093	46.261	13.4
44	3	0	-2	1.94365	46.696	0.6
45	2	3	0	1.92363	47.211	0.6
46	2	3	-2	1.92115	47.276	1.4
47	1	4	0	1.91318	47.485	2.4
48	1	4	-1	1.91257	47.501	0.0
49	3	1	-1	1.89274	48.030	1.9
50	3	1	-2	1.89096	48.078	7.1
51	1	0	-4	1.87707	48.457	15.1
52	1	3	2	1.84815	49.265	4.4
53	1	3	-3	1.84540	49.343	3.6
54	1	1	3	1.83324	49.693	7.8
55	1	1	-4	1.82948	49.802	0.5
56	2	0	2	1.82245	50.007	1.1
57	2	0	-4	1.81615	50.192	0.1
58	3	0	0	1.81014	50.371	0.1
59	1	4	1	1.78297	51.193	0.1
60	1	4	-2	1.78149	51.239	1.6
61	2	1	2	1.77881	51.322	9.3
62	2	1	-4	1.77294	51.504	2.9
63	3	1	0	1.76735	51.679	0.3
64	0	3	-3	1.76361	51.797	4.8
65	3	1	-3	1.76303	51.815	0.4
66	0	4	2	1.76127	51.870	0.5
67	3	2	-1	1.75680	52.012	9.3
68	3	2	-2	1.75539	52.057	10.9
69	2	3	1	1.73501	52.716	9.9
70	0	0	4	1.73479	52.723	0.1
71	2	3	-3	1.73137	52.835	5.1
72	1	2	3	1.70891	53.584	0.1
73	1	2	-4	1.70587	53.687	0.1
74	0	1	-4	1.69702	53.990	0.4
75	2	4	-1	1.67950	54.600	17.9

76	2	2	2	1.66457	55.131	3.7
77	2	2	-4	1.65976	55.304	10.9
78	3	2	0	1.65517	55.471	9.2
79	3	2	-3	1.65162	55.600	0.9
80	2	4	0	1.63313	56.286	0.4
81	2	4	-2	1.63161	56.343	1.2
82	3	0	-4	1.60055	57.537	6.9
83	0	2	-4	1.59698	57.678	4.1
84	0	5	1	1.59179	57.884	0.8
85	1	4	2	1.58618	58.108	0.8
86	1	4	-3	1.58444	58.178	9.0
87	3	3	-1	1.58355	58.214	2.2
88	3	3	-2	1.58251	58.256	0.0
89	3	1	1	1.57584	58.526	5.4
90	3	1	-4	1.57074	58.735	1.9
91	1	5	0	1.56593	58.933	0.8
92	1	5	-1	1.56560	58.947	0.7
93	1	3	3	1.54820	59.675	0.3
94	1	3	-4	1.54594	59.772	0.9
95	0	4	3	1.53177	60.382	0.2
96	2	3	2	1.51500	61.121	0.2
97	2	4	1	1.51291	61.214	5.6
98	2	3	-4	1.51137	61.284	0.0
99	2	4	-3	1.51050	61.323	1.2
100	3	3	0	1.50791	61.440	1.0
101	3	3	-3	1.50522	61.561	4.4
102	3	2	1	1.49476	62.039	1.5
103	1	0	4	1.49310	62.116	4.3
104	1	5	1	1.49209	62.163	2.6
105	1	5	-2	1.49122	62.203	1.2
106	3	2	-4	1.49041	62.241	0.6
107	0	5	-2	1.47930	62.761	0.1
108	4	0	-2	1.47299	63.061	3.8
109	2	1	3	1.47272	63.074	0.7
110	1	1	4	1.46881	63.261	0.0
111	2	1	-5	1.46828	63.286	0.7
112	1	1	-5	1.46633	63.380	0.5
113	0	3	-4	1.46351	63.517	0.3
114	4	1	-2	1.44966	64.196	0.7
115	2	5	-1	1.42986	65.194	0.6
116	4	1	-1	1.42002	65.702	1.7
117	4	1	-3	1.41803	65.806	1.4
118	3	4	-1	1.40932	66.265	0.2
119	3	4	-2	1.40859	66.304	0.6
120	2	2	3	1.40590	66.447	2.1
121	1	2	4	1.40250	66.629	0.1
122	2	2	-5	1.40204	66.654	3.9
123	2	5	0	1.40091	66.714	0.3
124	1	2	-5	1.40034	66.745	0.4
125	2	5	-2	1.39996	66.766	0.7
126	3	0	2	1.39779	66.883	0.7
127	4	2	-2	1.38580	67.539	0.1
128	1	4	3	1.38424	67.625	3.9
129	3	3	1	1.38364	67.659	0.2
130	1	4	-4	1.38262	67.715	0.4
131	3	3	-4	1.38018	67.851	0.1
132	3	1	2	1.37780	67.984	0.9
133	3	1	-5	1.37303	68.253	0.1
134	1	5	2	1.37094	68.371	2.3
135	1	5	-3	1.36982	68.435	2.0
136	0	1	-5	1.36827	68.523	0.9

137	0	6	0	1.36283	68.835	0.8
138	2	4	2	1.36035	68.978	0.3
139	4	2	-1	1.35984	69.008	0.5
140	4	2	-3	1.35809	69.110	0.5
141	2	4	-4	1.35772	69.131	0.6
142	4	0	0	1.35761	69.138	3.1
143	3	4	0	1.35521	69.277	0.4
144	4	0	-4	1.35412	69.341	0.1
145	3	4	-3	1.35326	69.392	1.7
146	4	1	0	1.33927	70.222	1.4
147	0	6	-1	1.33729	70.342	0.2
148	4	1	-4	1.33593	70.424	0.8
149	0	5	-3	1.33535	70.459	0.4
150	2	5	1	1.32280	71.228	0.8
151	0	4	-4	1.32271	71.234	0.2
152	3	2	2	1.32263	71.239	0.0
153	1	6	0	1.32184	71.288	1.5
154	1	6	-1	1.32164	71.301	5.2
155	2	5	-3	1.32119	71.329	2.1
156	3	2	-5	1.31841	71.502	0.1
157	0	2	-5	1.31419	71.767	1.2
158	2	3	3	1.31226	71.889	3.0
159	1	3	4	1.30950	72.065	0.9
160	2	3	-5	1.30912	72.089	0.1
161	1	3	-5	1.30774	72.177	0.8
162	4	3	-2	1.29587	72.944	1.0
163	4	2	0	1.28843	73.433	0.0
164	4	2	-4	1.28545	73.631	3.4
165	1	6	1	1.27652	74.233	3.7
166	1	6	-2	1.27598	74.270	0.1
167	4	3	-1	1.27457	74.366	0.4
168	4	3	-3	1.27312	74.464	0.9
169	0	6	2	1.26849	74.783	0.0
170	3	4	1	1.26286	75.174	0.0
171	3	4	-4	1.26023	75.358	0.3
172	2	0	4	1.25723	75.570	0.4
173	2	0	-6	1.25377	75.815	0.1
174	3	5	-1	1.25188	75.950	0.0
175	3	5	-2	1.25137	75.986	0.0
176	3	3	2	1.24377	76.534	1.7
177	2	1	4	1.24262	76.617	0.1
178	3	3	-5	1.24026	76.790	0.0
179	2	1	-6	1.23929	76.861	0.5
180	2	6	-1	1.23689	77.037	0.4
181	0	3	5	1.23675	77.048	0.0
182	1	5	3	1.23420	77.237	1.3
183	1	5	-4	1.23305	77.322	0.7
184	1	0	-6	1.23280	77.340	1.6
185	4	1	1	1.23030	77.527	0.4
186	4	1	-5	1.22642	77.819	0.1
187	1	1	5	1.22077	78.247	0.8
188	1	1	-6	1.21902	78.381	1.5
189	2	6	0	1.21802	78.458	0.8
190	2	6	-2	1.21739	78.507	0.2
191	2	5	2	1.21718	78.522	0.2
192	2	5	-4	1.21529	78.668	0.0
193	4	3	0	1.21521	78.674	0.2
194	3	5	0	1.21349	78.807	0.9
195	4	3	-4	1.21271	78.868	0.4
196	3	5	-3	1.21209	78.916	1.2
197	3	0	-6	1.21077	79.019	2.2

198	2	4	3	1.20789	79.244	0.2
199	1	4	4	1.20573	79.414	0.1
200	2	4	-5	1.20544	79.438	0.1
201	1	4	-5	1.20436	79.523	4.5
202	3	1	3	1.20178	79.728	1.9
203	2	2	4	1.20169	79.735	1.8

Structure

No.	Name	Elem.	X	Y	Z	Biso	sof	Wyck.
1	O1	O	0.26890	0.02760	0.01210	1.2800	1.0000	4e
2	O2	O	0.23560	0.44850	0.12710	1.5500	1.0000	4e
3	O3	O	0.77790	0.30220	0.20710	1.5300	1.0000	4e
4	BI1	Bi	0.03810	0.04280	0.27690	1.2600	1.0000	4e
5	BI2	Bi	0.52380	0.31480	0.36310	1.1700	1.0000	4e

Stick Pattern

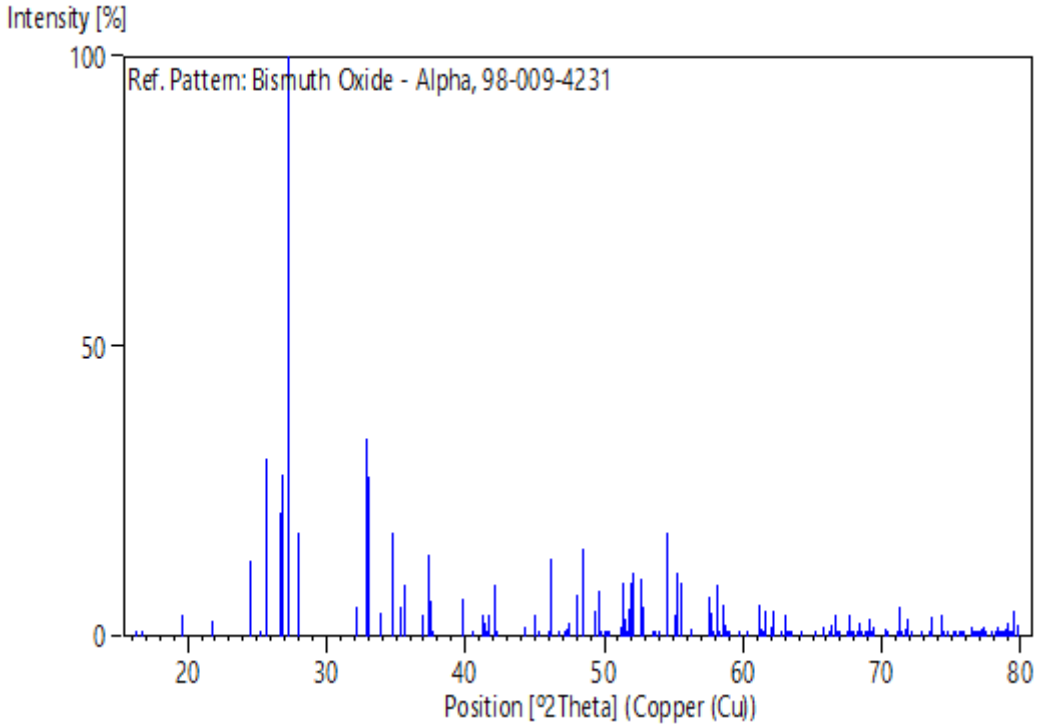

XRD ICSD card of $BiFeO_3$ and Bi_2O_3 phases in the composite :

Name and formula

Reference code: 98-024-6424

Compound name: Bismuth Ferrate(III)
Common name: Bismuth Ferrate(III)

Chemical formula: $Bi_1Fe_1O_3$

Crystallographic parameters

Crystal system:	Hexagonal
Space group:	R 3 c
Space group number:	161
a (Å):	5.4992
b (Å):	5.4992
c (Å):	13.4732
Alpha (°):	90.0000
Beta (°):	90.0000
Gamma (°):	120.0000
Calculated density (g/cm^3):	8.83
Volume of cell (10^6 pm^3):	352.86
Z:	2.00
RIR:	9.57

Subfiles and quality

Subfiles:	User Inorganic
Quality:	User From Structure (=)

Comments

Creation Date:	8/1/2009
Modification Date:	12/30/1899
Original ICSD space group:	R3CR. At least one temperature factor missing in the paper.. No R value given in the paper.
Structure type:	LiNbO3. Structure calculated theoretically DFT ab initio calculation with VASP program using PAW formalism. Standard deviation missing in cell constants
Structure type:	LiNbO3
Recording date:	8/1/2009
ANX formula:	ABX3
Z:	2
Calculated density:	8.83
Pearson code:	hR10
Wyckoff code:	b a2

Structure TIDY: TRANS a-b,b-c,a+b+c -x,-y,-z origin 0 0 .77200
Structure TIDY: REMARK Transformed from rhombohedral cell.
Publication title: First principles study of the multiferroics Bi Fe O3, Bi2 Fe Cr O6, and Bi Cr O3: Structure, polarization, and magnetic ordering temperature
ICSD collection code: 246424
Structure: LiNbO3
Chemical Name: Bismuth Ferrate(III)
Second Chemical Formula: Bi (Fe O3)

References

Structure: Spaldin, N.A.;Ederer, C.;Baettig, P., *Physical Review, Serie 3. B - Condensed Matter (18,1978-)*, **72**, 0, (2005)

Peak list

No.	h	k	l	d [A]	2Theta[deg]	I [%]
1	0	1	2	3.88881	22.850	74.1
2	1	0	4	2.75000	32.533	100.0
3	1	1	3	2.34501	38.354	2.2
4	0	0	6	2.24553	40.124	6.8
5	2	0	2	2.24509	40.132	27.0
6	0	2	4	1.94440	46.677	42.1
7	2	1	1	1.78418	51.156	0.4
8	1	1	6	1.73923	52.578	26.5
9	1	2	2	1.73903	52.584	17.1
10	0	1	8	1.58779	58.043	17.3
11	2	1	4	1.58756	58.052	37.8
12	1	2	5	1.49679	61.946	0.2
13	2	0	8	1.37500	68.142	8.4
14	2	2	0	1.37480	68.153	12.2
15	1	1	9	1.31478	71.730	0.2
16	2	1	7	1.31470	71.735	0.1
17	1	3	1	1.31456	71.744	0.3
18	1	0	10	1.29644	72.906	6.4
19	0	3	6	1.29627	72.918	4.1
20	3	1	2	1.29618	72.923	6.0
21	1	2	8	1.22980	77.564	13.2
22	1	3	4	1.22969	77.572	14.2
23	3	1	5	1.18604	81.004	0.2
24	0	2	10	1.17263	82.128	3.4
25	2	2	6	1.17250	82.138	6.2
26	0	4	2	1.17244	82.144	2.6
27	0	0	12	1.12277	86.640	0.9
28	4	0	4	1.12255	86.661	5.4

Structure

No.	Name	Elem.	X	Y	Z	Biso	sof	Wyck.
1	O1	O	0.07533	0.32467	0.11067	0.5000	1.0000	18b
2	FE1	Fe	0.00000	0.00000	0.00000	0.5000	1.0000	6a
3	BI1	Bi	0.00000	0.00000	0.22800	0.5000	1.0000	6a

Stick Pattern

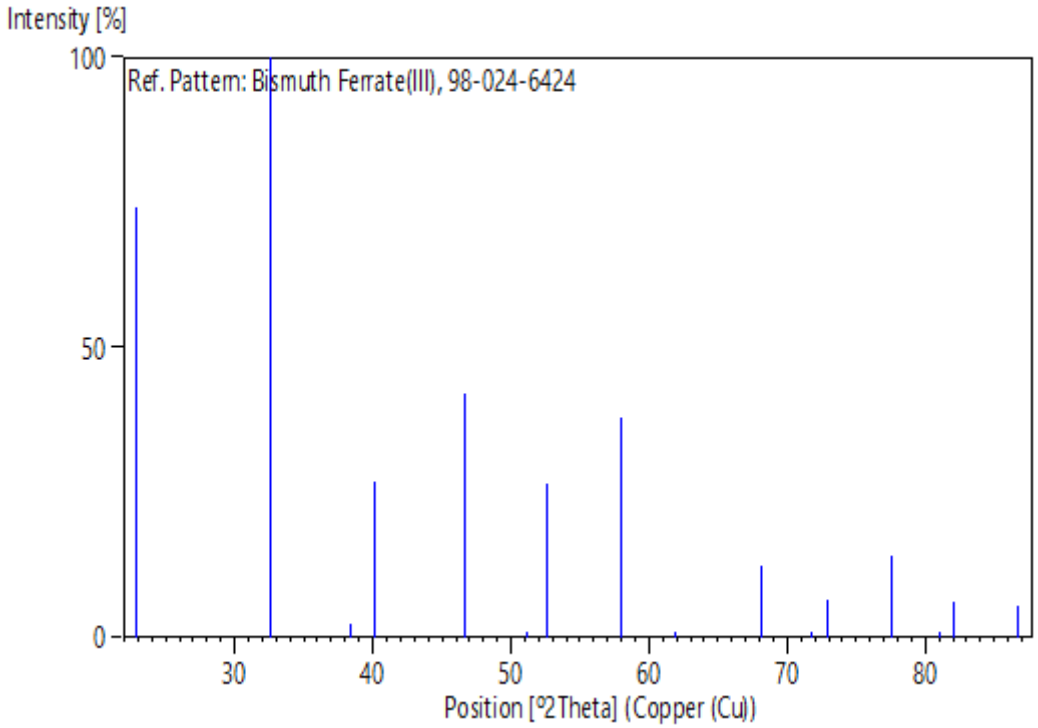

Name and formula

Reference code:	98-002-7458
Compound name:	Bismuth Oxide - Delta, Ht
Common name:	Bismuth Oxide - Delta, Ht
Chemical formula:	Bi_2O_3

Crystallographic parameters

Crystal system:	Cubic
Space group:	F m -3 m
Space group number:	225
a (Å):	5.6650
b (Å):	5.6650
c (Å):	5.6650
Alpha (°):	90.0000
Beta (°):	90.0000
Gamma (°):	90.0000
Calculated density (g/cm^3):	8.51
Measured density (g/cm^3):	8.68
Volume of cell (10^6 pm^3):	181.80
Z:	2.00
RIR:	23.42

Subfiles and quality

Subfiles: User Inorganic
Quality: User From Structure (=)

Comments

Creation Date: 9/25/1986
Modification Date: 2/1/2010
Original ICSD space group: FM3-M
AE: Bi: O6; O: Bi4; defect fluorite type. Stable above 1003 K (2nd ref., Tomaszewski), on cooling down to 923 K, from 923 to 773 K: P4-b2. At RT stable are the isomorphs Bi2 O3 * 1/6Si O2: 5.542 and Bi2 O3 * 1/2W O3: 5.589. At least one temperature factor missing in the paper.. X-ray diffraction from single crystal. Structure type : defect-CaF2. Temperature in Kelvin: 1023. Structure determined from projections. The structure has been assigned a PDF number (experimental powder diffraction data): 27-52. The structure has been assigned a PDF number (calculated powder diffraction data): 01-074-1633. Structure type: defect-CaF2. Recording date: 9/25/1986. Modification date: 2/1/2010. ANX formula: A2X3. Z: 2. Authors density: 8.68. Calculated density: 8.51. R value: 0.019. Pearson code: cF10. Wyckoff code: c a. PDF code: 00-027-0052
Publication title: Die Kristallstruktur der Hochtemperaturmodifikation von Wismut(III)-oxid (delta-Bi2 O3)
ICSD collection code: 27458
Structure: defect-CaF2
Chemical Name: Bismuth Oxide - Delta, Ht
Second Chemical Formula: Bi2 O3

References

Structure: Schroeder, H.;Gattow, G., *Phase Transition*, **38**, 127 - 220, (1992)

Peak list

No.	h	k	l	d [A]	2Theta[deg]	I [%]
1	1	1	1	3.27069	27.244	100.0
2	0	0	2	2.83250	31.561	38.6
3	0	2	2	2.00288	45.237	46.8
4	1	1	3	1.70806	53.613	44.9
5	2	2	2	1.63534	56.203	10.4
6	0	0	4	1.41625	65.899	7.0
7	1	3	3	1.29964	72.698	17.3
8	0	2	4	1.26673	74.904	13.2
9	2	2	4	1.15636	83.540	13.9
10	1	1	5	1.09023	89.910	10.0

Structure

No.	Name	Elem.	X	Y	Z	Biso	sof	Wyck.
1	O1	O	0.25000	0.25000	0.25000	0.5000	0.7500	8c
2	BI1	Bi	0.00000	0.00000	0.00000	0.5000	1.0000	4a

Stick Pattern

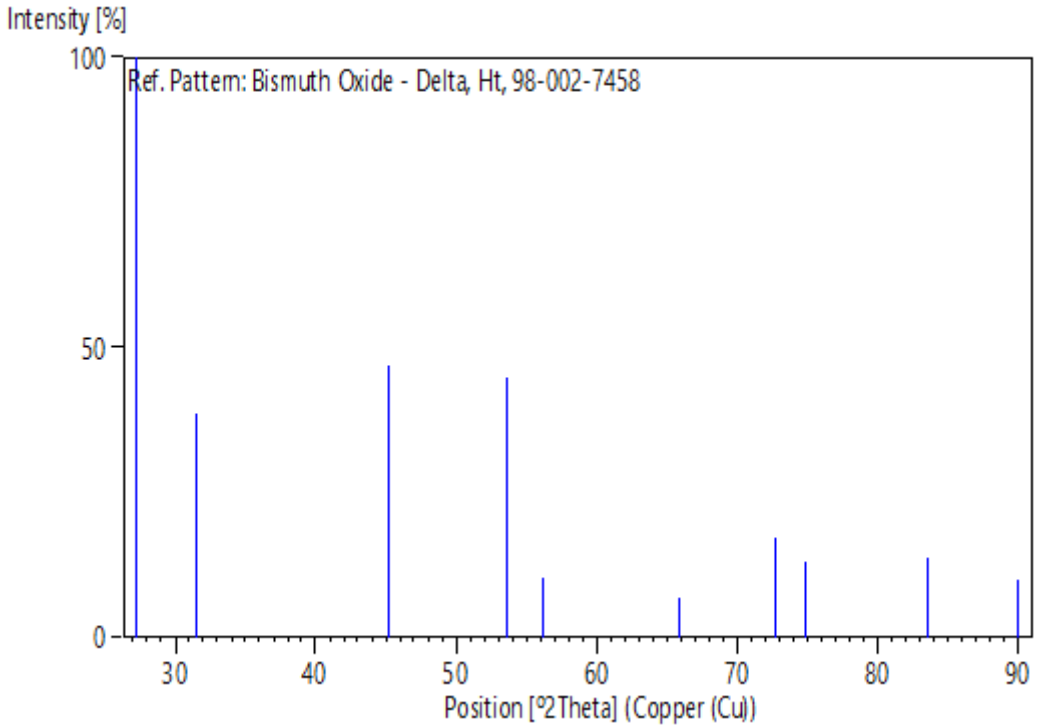

الملخص

يبحث هذا العمل في المواد المركبة $BiFeO_3/Bi_2O_3$ كحل محتمل لاستصلاح البيئة وإنتاج الطاقة النظيفة. حيث يفصل عملية تحضير كل من $BiFeO_3$ و Bi_2O_3 والمواد المركبة $BiFeO_3/Bi_2O_3$ مع كميات زائدة مختلفة من نترات البزموت بطريقة الإحتراق الذاتي، يليها توصيف شامل باستخدام تقنيات حيود الأشعة السينية (XRD) وطيف إلكترونات البروتونات السينية (XPS) والتحليل الطيفي تحت الأحمر بتحويل فورييه (FTIR) والمجهر الإلكتروني الماسح المقترن بالتحليل الطيفي بالأشعة السينية ذات الطاقة الانتشارية (SEM-EDS) والتحليل الطيفي للأشعة فوق البنفسجية-المرئية. يكشف التوصيف بشكل ملحوظ عن فجوة نطاق طاقة أقل ومورفولوجيا مسامية للمركب $BiFeO_3/Bi_2O_3$ مقارنة بالأكاسيد. مما يوضح الأداء الفائق للمركب في كل من التحلل الضوئي للملوثات العضوية وإنتاج غاز الهيدروجين من خلال عملية تحليل هيدروكسيد البورون للميثانول. بشكل عام، يسلط هذا العمل الضوء على المادة المركبة $BiFeO_3/Bi_2O_3$ كمحفزات فعالة وقابلة لإعادة الاستخدام، مما يمهد الطريق لمستقبل أكثر استدامة.

Résumé

Cette thèse explore les composite $BiFeO_3/Bi_2O_3$ comme solution potentielle pour l'assainissement de l'environnement et la production d'énergie propre. Il détaille la synthèse de $BiFeO_3$, Bi_2O_3 et de composites $BiFeO_3/Bi_2O_3$ avec des excès de Bi variables par autocombustion, suivie d'une caractérisation complète par diffraction des rayons X (DRX), spectroscopie de photoélectrons X (XPS), spectroscopie infrarouge à transformée de Fourier (FTIR), microscopie électronique à balayage couplée à la spectroscopie d'énergie dispersive aux rayons X (SEM-EDS) et spectroscopie UV-visible. La caractérisation révèle notamment une bande interdite plus faible et une morphologie poreuse pour le composite $BiFeO_3/Bi_2O_3$ par rapport aux oxydes individuels, ce qui démontrent la performance supérieure du composite dans la dégradation photocatalytique des polluants organiques et la production d'hydrogène par méthanolisation au borohydrure de sodium. Dans l'ensemble, ce travail souligne la promesse des composites $BiFeO_3/Bi_2O_3$ en tant que catalyseurs efficaces et réutilisables, ouvrant la voie à un avenir plus durable.

Abstract

This thesis investigates $BiFeO_3/Bi_2O_3$ composites as a potential solution for environmental remediation and clean energy generation. It details the autocombustion synthesis of $BiFeO_3$, Bi_2O_3, and $BiFeO_3/Bi_2O_3$ composites with varying Bi excesses, followed by comprehensive characterization using X-ray diffraction (XRD), X-ray photoelectron spectroscopy (XPS), Fourier-transform infrared spectroscopy (FTIR), scanning electron microscopy coupled with energy-dispersive X-ray spectroscopy (SEM-EDS), and UV-visible spectroscopy. Notably, the characterization reveals a lower band gap and porous morphology for the $BiFeO_3/Bi_2O_3$ composite compared to the individual oxides. Which demonstrate the composite's superior performance in both photocatalytic degradation of organic pollutants and hydrogen gas generation through sodium borohydride methanolysis. Overall, this work highlights the promise of $BiFeO_3/Bi_2O_3$ composites as efficient and reusable catalysts, paving the way for a more sustainable future.